

Exploratory modelling of the formation of tidal bars under a propagating tidal wave using a linear stability analysis

MSc Thesis

By

R. D. White¹

September 2021



"The Great Wave of Kanagawa" by Katsushika Hokusai

Graduation committee:

Dr. ir. P. C. Roos

Ir. W. M. van der Sande

Prof. dr. S. J. M. H. Hulscher

University of Twente

University of Twente

University of Twente

Department of Water Engineering & Management

Faculty of Engineering Technology

University of Twente

Enschede, The Netherlands

¹ Contact: rubenwhitenl@hotmail.com

I. Preface

In front of you lies my master thesis for the research carried out for the Marine and Fluvial Systems group at the University of Twente. This thesis also marks the end of my master's in Water Engineering & Management and my time as a student at the University of Twente. I could not have completed my studies and this thesis without the support of everyone involved.

First, I would like to thank Wessel and Pieter for supervising my master thesis. I could not have wished for better supervisors. Both of you were always willing to think along, provide feedback and give your opinions. I am also grateful for the support and positivity you two provided during my thesis, especially during more difficult times. I really enjoyed working with both of you and hope to be able to do this again in the future. I would like to give an additional thank you to Pieter for the sessions throughout my bachelor and master in which we would talk about the progression of my studies. I would also like to thank Suzanne for her contribution to this thesis. Although you might have been less directly involved, I am still very grateful for the time you set aside to join several meetings and the feedback you provided during the evaluation sessions.

Thank you to everyone at the department of Civil Engineering and Management, especially within the Water Engineering and Management department, for creating a pleasant environment for studying and working. A special thanks to Judith, another member of the Roos family, with whom I would regularly talk about my study progression, mainly during the first two years of my bachelor. I am also grateful to Gerrit and Maarten for providing opportunities to work as a student assistant at the University of Twente.

Throughout the entire duration of my studies, I have lived at the "Piratio". Suhaib, Max, Martijn, Rogier, Arthur, Victor and Emre, thank you all for the countless laughs and unforgettable memories you provided during my time on the ship. I will be sure to keep in touch and hope we will be able to hoist the anchor, lower the sails and raise the flag for the occasional voyage in the future.

I would like to thank all my friends that have supported me throughout my studies. Tom and Henri, thank you for the numerous hours we have spent together working on several projects and the few moments during which we would unwind. I would also like to explicitly thank the members of Huize Burgerlijkheid. Simon, Bjorn, Kelt and Tim, your house truly felt like a second student home. Also thank you to Lucas, Dyon, Jasper, Kees, Frederik and many others for the moments we spent together online and when I returned to Bussum.

Beyza, I am very happy I got to know you during my studies. Thank you for your support during my master and this thesis. I can always tell you what is on my mind, and you are able to take my mind of my work like no other.

Finally, I would like to thank my family. Mom, Dad, Emily and Julia, you supported me through every step of the way, and have had an incredibly important role in shaping me into the person I am today.

Thank you all,

Ruben White

II. Summary

Tidal bars are rhythmic bed features that occur in tidal channels. These bars typically have heights of several metres and wavelengths of 1 to 15 km. The formation of rhythmic bed features is often studied using the linear stability concept, in which the formation of bedforms is explained as a free instability of a morphodynamic system. In linear stability models several assumptions are usually applied to simplify and schematise the modelled system. One of these is the so-called rigid lid assumption, through which the free surface effects are neglected. These are effects caused by changes in the position of the water surface due to tidal waves. This assumption is currently applied in most linear stability studies.

In this study we develop a (numerical) linear stability model in which the rigid lid assumption is not applied, i.e., the NRL (non-rigid lid) model. This (numerical) NRL model aims to include (instead of neglect) the free surface effects caused by a propagating tidal wave. The NRL model can therefore be used to obtain physics-based insights into the influence of a propagating tidal wave on the formation of tidal bars. These insights are obtained by comparing the NRL model to a traditional (semi-analytical) linear stability model in which the rigid lid assumption is applied, i.e., the RL (rigid lid) model. This is done for two cases in the Western Scheldt: the standard friction case and the reduced friction case.

First, a model is formulated for a propagating tidal wave in a tidal channel. This model consists of the depth-averaged hydrodynamic equations, a simple sediment transport formula and a sediment conservation equation for the bed evolution. Boundary conditions are defined that allow a tidal wave to propagate in the positive along-channel direction.

Next, an expansion in the Froude number is used to obtain a solution to the basic state for the NRL model. The solutions for the basic flow show that the free water surface and depth-averaged velocity in the along-channel direction are described by sinusoidal waves that travel in the along-channel direction. Moreover, because the solution for the basic flow is spatially variant, the sensitivity of the bed evolution under the basic flow is analysed. This is done by comparing the bed evolution in the basic state to the approximated evolution of the bed in the perturbed state. If the former is small compared to the latter, it is valid to conclude that the bed in the basic state remains relatively flat. The results show that the solution to the basic state for the NRL model presented in this study is only valid for the reduced friction case.

Thereafter, a numerical solution procedure for the perturbed state is developed. This is done because the traditional (semi-analytical) procedure breaks down when the solution to the basic state is spatially variant, as is the case for the NRL model. As part of this numerical procedure, a generalised eigenvalue problem for the evolution of this state is defined. The eigenvectors and eigenvalues that follow from this problem describe the structure of the bedforms and can be used to determine the other bedform characteristics (i.e., growth rate, cross-channel mode and wavelength). These characteristics are used to construct growth curves and to define the fastest growing mode (FGM). The FGM is considered the dominant bedform and therefore provides insight into the behaviour of the modelled system.

The numerical solution procedure for the perturbed state is first applied to the RL model. This is done to validate the numerical procedure by comparing the numerical solutions to those obtained using the semi-analytical procedure. The results for both cases in the Western Scheldt show that the numerical and semi-analytical solutions are approximately equal when the number of discretisation points is sufficiently large.

Finally, the numerical solution procedure is applied to the NRL model in which a propagating tidal wave is considered. The solutions for the NRL model are compared to those obtained using the RL model. The results for the reduced friction case show that the peaks of the growth curves (for higher cross channel modes) for the NRL model are higher and occur at larger wavenumbers compared to those for the RL model.

We define two preconditions: the abovementioned difference is caused by a propagating tidal wave; and the influence of a propagating tidal wave is the same for both friction cases. Assuming these preconditions are true, we expect that a propagating tidal wave might have the following influence on the formation of tidal bars: (1) formation of shorter tidal bars (i.e., the wavelength of the FGM decreases); and (2) faster formation of tidal bars (i.e., the growth rate of the FGM increases). However, to ensure the validity of these statements, further research must be conducted in which the NRL model is improved and validated.

Contents

I. Preface	3
II. Summary	5
1. Introduction to tidal bars and linear stability analysis	9
1.1 Background.....	9
1.2 State-of-the-art knowledge.....	10
1.3 Knowledge gap	12
1.4 Objective and research questions.....	12
1.5 Methods	12
1.6 Report structure.....	14
2. Model formulation for a propagating tidal wave in a tidal channel	15
2.1 Model outline	15
2.2 Geometry.....	15
2.3 Hydrodynamics.....	16
2.4 Sediment transport	17
2.5 Bed evolution	17
3. Basic state when including a propagating tidal wave	18
3.1 Scaling procedure without rigid lid assumption.....	18
3.2 Spatially variant basic state	19
3.3 Sensitivity of the bed evolution in the spatially variant basic state.....	22
4. Numerical solution procedure for the perturbed state	25
4.1 Scaling procedure with rigid lid assumption	25
4.2 Spatially uniform basic state	26
4.3 Numerical solution procedure for the perturbed state	27
4.4 Comparison of the numerical and semi-analytical solutions to the perturbed state	30
5. Perturbed state when including a propagating tidal wave	33
5.1 Numerical solution procedure for the perturbed state	33
5.2 Numerical solutions to the perturbed state when including a propagating tidal wave	35
6. Discussion	38
6.1 Interpretation of the results for the NRL model	38
6.2 Evaluation of the NRL model.....	44
7. Conclusion and Outlook	46
7.1 How can a propagating tidal wave be considered in a linear stability model for tidal bars?.....	46
7.2 How can we define a meaningful basic state for this NRL model?	46
7.3 How can we obtain the solution to the perturbed state for this NRL model?.....	46
7.4 What are the growth characteristics for this NRL model?	46
7.5 What is the influence of a propagating tidal wave on the formation of tidal bars?	47
7.6 Outlook for further research regarding the influence of a propagating tidal wave on the formation of rhythmic bed features.....	47
References	49
Appendices	51
Appendix A: Rewritten model equations for the perturbed state	51
Appendix B: Expanded matrices for the generalised eigenvalue problem	54
Appendix C: Vectors and matrices	59
Appendix D: Method to construct growth curves for multichromatic bedforms	61
Appendix E: NRL model with non-periodic boundary conditions	62

1. Introduction to tidal bars and linear stability analysis

This chapter contains the background, state-of-the-art-knowledge and knowledge gap regarding the subject of this study. This is followed by the objective of this study, with the corresponding research questions, and the methods used to answer these research questions. Finally, an overview of the report structure is given.

1.1 Background

Tidal bars are rhythmic bed features that occur in tidal channels (or estuaries) and offshore areas. This study focusses on the formation of tidal bars in the former environment. Examples of tidal channels with tidal bars include the Western Scheldt in the Netherlands, the Ord River Estuary in Australia, the Exe Estuary in England and the Netarts bay in the United States (see Figure 1). Note that tidal bars do not necessarily have to protrude from the water but can also be fully submerged. Tidal bars typically have heights of several metres, wavelengths of 1 to 15 km (Hepkema et al., 2019) and usually an alternating cross-channel structure. Their characteristics are determined by channel properties, such as channel depth, channel width and tidal amplitude (Dalrymple & Rhodes, 1995; Leuven et al., 2016; Tambroni et al., 2005). These properties may change due to human interventions and climate change (e.g., dredging, land reclamation and sea level rise). Tidal bars function as rich feeding grounds for many organisms but may also impede marine traffic (Hepkema et al., 2019). It is therefore important to understand the dynamics of these bed features for proper management of tidal channels.

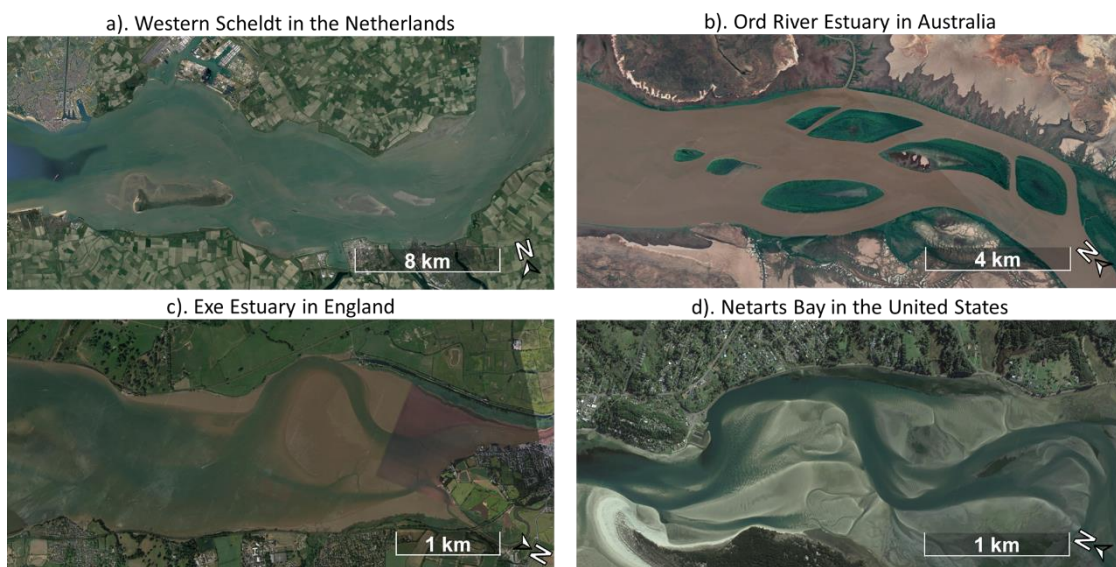


Figure 1: Tidal bars in four different tidal channels: (a) Western Scheldt in The Netherlands; (b) Ord River Estuary in Australia; (c) Exe Estuary in England; and (d) Netarts bay in the United States (images from Google Earth; and composition based on Hepkema et al., 2019).

The formation of tide-induced rhythmic bed features (e.g., sand banks, sand waves and tidal bars) is often explained as a morphodynamic instability of the coupled water-sediment system subject to tidal motion. Huthnance (1982a, 1982b) was the first to show this for sand banks using a so-called linear stability analysis. This is an idealised process-based approach, meaning that mathematical formulations are used to capture the fundamental physical processes of a system. The model by Huthnance consists of the depth-averaged shallow water equations, a simple sediment transport formula and a sediment conservation equation for the bed evolution. The linear stability concept was later also used to analyse the formation of other rhythmic bed features, such as sand waves (e.g., Campmans et al., 2017; Hulscher, 1996) and tidal bars (e.g., Hepkema et al., 2019, 2020; Schramkowski et al., 2002; Seminara & Tubino, 2001).

Seminara and Tubino (2001) used a 3D idealised model to demonstrate that tidal bars can form as free instabilities of a morphodynamic system. They found modelled tidal bars with wavelengths comparable to those of tidal bars observed in the field. Later, Schramkowski et al. (2002) showed that a depth-averaged model is sufficient to model the characteristics of tidal bars. This model demonstrated that the current velocity and water depth are important when determining the wavelength of tidal bars. The model by Schramkowski et al. (2002) was later extended to include the effects of channel width and the Coriolis effect on the formation of tidal bars (Hepkema et al., 2019, 2020).

Since linear stability models are idealised, they only consider the physical processes of a system that are believed to be essential for the phenomenon under study. The modelled system is therefore usually simplified and schematised by applying several assumptions. One of these is the so-called rigid lid assumption, through which the free surface effects are neglected. These are effects caused by changes in the position of the water surface due to tidal waves. They become relevant when the change in the water surface elevation is significantly large compared to the water depth (for river dunes, see Naqshband et al., 2014).

The rigid lid assumption is currently applied in most studies in which the linear stability concept is used to analyse rhythmic bed features. Marine and riverine environments are generally characterised by relatively small changes in the water surface compared to the overall water depth. However, tides in estuarine environments can lead to significant water depth changes (Lange et al., 2008). Because of this, free surface effects are probably more significant in tidal channels than in other environments. Therefore, it might not be valid to apply the rigid lid assumption when using a linear stability analysis to study tidal bars in tidal channels.

The following section provides further information regarding the linear stability concept, free surface effects and the rigid lid assumption.

1.2 State-of-the-art knowledge

1.2.1 Linear stability analysis

The formation of rhythmic bed features can be explained as a free instability of a morphodynamic system. In a linear stability analysis this is investigated by analysing the stability of the so-called basic state. This state is generally characterised as a (usually spatially uniform) tidal current over a flat bed. Next, bed perturbations with arbitrary wavelengths (referred to as ‘modes’) are introduced to the system. According to Dodd et al. (2003), a linear stability analysis will reveal one of the following possibilities: no positive growth rates for all modes or positive growth rates for a finite range of modes. In the first case, the basic state is termed stable since the system evolves back to the basic state. In the latter case, the basic state is termed unstable since the system does not evolve back to the basic state. For an unstable basic state, the mode with the maximum growth rate can be determined. This mode, assuming that it is unique, is defined as the fastest growing mode (FGM) (Dodd et al., 2003). The FGM does not necessarily have to be the mode that persists once the system has reached a dynamic equilibrium. However, several studies show that the linearly predicted characteristics (i.e., growth rate, migration rate, cross-channel mode and wavelength) roughly agree with those of bedforms found in the field (e.g., Campmans et al., 2017; Hepkema et al., 2019; Hulscher, 1996; Hulscher & van den Brink, 2001). The FGM thus provides insight into the behaviour of the modelled system.

The above can be formulated from a mathematical point of view. The state of the system is symbolically written as:

$$\boldsymbol{\phi} = [\zeta, u, v, q_x, q_y, h]^T, \quad (1)$$

where, $\boldsymbol{\phi}$ is a vector containing all system variables; ζ is the free surface elevation; u and v are the horizontal flow velocity components; q_x and q_y are the horizontal bed load sediment fluxes; and h is the bed topography. The stability of a certain state $\boldsymbol{\phi}_0$ of the system (termed the ‘basic state’) is analysed by introducing small wave-like bed perturbations to that state. The amplitude of these perturbations (\hat{h}^*) is relatively small compared to the mean water depth (H^*). This is denoted by $\varepsilon = \hat{h}^*/H^*$. Here, dimensional quantities are denoted by an asterisk (*). The approximated solution can thus be written as:

$$\boldsymbol{\phi} = \boldsymbol{\phi}_0 + \varepsilon \boldsymbol{\phi}_1 + \mathcal{O}(\varepsilon^2), \quad (2)$$

where, $\boldsymbol{\phi}_0$ is the basic state; $\boldsymbol{\phi}_1$ is the perturbed state; and higher order terms are neglected, because ε is relatively small.

1.2.2 Free surface effects

Free surface effects are effects caused by changes in the position of the water surface. These effects become more relevant for large values of the Froude number (Fox et al., 2015). The Froude number is defined as:

$$\text{Fr} = \frac{U^*}{\sqrt{g^* H^*}}, \quad (3)$$

where, Fr is the Froude number; U^* is the amplitude of the depth-averaged flow velocity, in this case of the tidal flow; g^* is the gravitational acceleration; and H^* is the mean water depth. In this case, the water depth is much smaller than the wavelength of the tidal waves. Therefore, the dispersion relation for shallow water waves (Phillips, 1977) can be used: $\omega^{*2} = g^* H^* k^{*2}$, where ω^* is the tidal frequency and k^* is the tidal wavenumber. The depth-averaged flow velocity can thus be determined by $U^* = \sqrt{g^*/H^*} Z^*$. Substituting this expression in the definition for Fr (i.e., Eq.(3)), results in:

$$\text{Fr} = \delta = \frac{Z^*}{H^*}. \quad (4)$$

Here, δ is the ratio between the amplitude of the free surface elevation and the mean water depth; and Z^* is the amplitude of the free surface elevation. Since δ is equal to Fr, free surface effects also become important when the change in the surface elevation is sufficiently large compared to the water depth, i.e., when δ is sufficiently large.

1.2.3 Rigid lid assumption

It is generally stated that when the rigid lid assumption is applied, the free surface effects are neglected. However, this statement should be read with care since using this assumption does not actually eliminate all effects that are related to the changes in the position of the water surface. Only the contribution of the free surface elevation to the water level is neglected (see Figure 2). The spatial derivative of the free surface (e.g., $\partial\zeta^*/\partial x^*$) which induces a pressure gradient is not eliminated (e.g., see application of rigid lid assumption in Hepkema et al., 2019, 2020; Schramkowski et al., 2002).

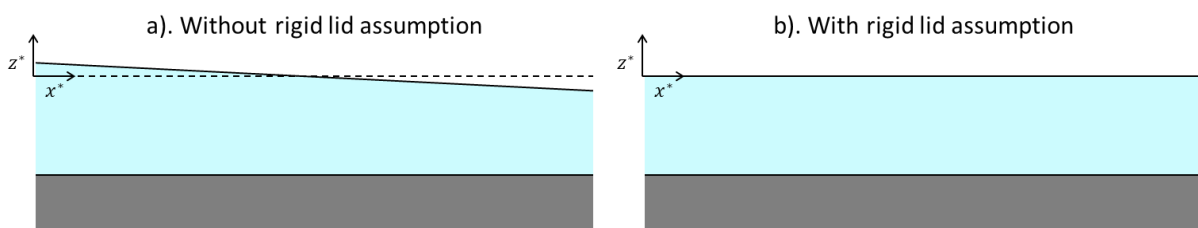


Figure 2: Schematic representation of the model domain (a) when the rigid lid assumption is not applied; and (b) when the rigid lid assumption is applied.

The rigid lid assumption simplifies a linear stability analysis, particularly the process of defining a basic state, which must be a solution to the model equations. Applying this assumption makes it possible to neglect several terms in the hydrodynamic equations. The basic state can therefore be characterised by a spatially uniform flow over a flat bed (e.g., see basic state in Hepkema et al., 2019, 2020; Schramkowski et al., 2002). This means that there is no divergence of tidally averaged bed transport and hence no bed evolution. This directly implies that the bed in the basic state remains flat. Moreover, this spatially uniform basic state facilitates the use of a semi-analytical procedure² to obtain the solution to the perturbed state. Part of this semi-analytical procedure is to predefine the monochromatic³ structure of the small bed perturbations.

Without the rigid lid assumption, it is not possible to define a spatially uniform flow in the basic state that is valid over large spatial scales. Moreover, due to the spatial variations in the basic state, the structure of the small bed perturbations cannot be predefined. Therefore, a numerical procedure must be used to obtain the solution to the perturbed state. This procedure allows the formation of multichromatic⁴ bedforms.

1.3 Knowledge gap

Several studies have been conducted in which the linear stability concept is used to physically explain the formation of rhythmic bed features, including tidal bars, sand banks and sand waves. However, the rigid lid assumption, through which free surface effects are neglected, is currently applied in most of these studies. Because of this, physics-based explanations regarding the influence of propagating tidal waves on the formation of rhythmic bed features are lacking. This is most relevant for tidal bars in tidal channels, since these estuarine environments are characterised by tides that can lead to significant changes in the water depth. Because of this, free surface effects are probably more significant in tidal channels than in other environments. Since the rigid lid assumption is routinely adopted, there is a knowledge gap regarding the concept of performing a linear stability analysis in which this assumption is not applied. Moreover, little is currently known about the influence of this assumption on the results obtained through a linear stability analysis.

1.4 Objective and research questions

The objective of this master thesis is to develop a (numerical) linear stability model in which the rigid lid assumption is not applied and use this model to obtain physics-based insights into the influence of a propagating tidal wave on the formation of tidal bars. This model is referred to as the NRL model. This objective is to be achieved by answering the following research questions (RQ):

1. *How can a propagating tidal wave be considered in a linear stability model for tidal bars?*
2. *How can we define a meaningful basic state for this NRL model?*
3. *How can we obtain a solution to the perturbed state for this NRL model?*
4. *What are the growth characteristics for this NRL model?*
5. *What is the influence of a propagating tidal wave on the formation of tidal bars?*

1.5 Methods

To answer the research questions, a (numerical) linear stability model is developed and used to analyse the formation of tidal bars. Hereafter, this model is referred to as the NRL (non-rigid lid) model (see Figure 3). The NRL model aims to include (instead of neglect) the free surface effects caused by a propagating tidal wave. The NRL model is compared to a traditional (semi-analytical) linear stability model in which the rigid lid assumption is applied. Hereafter, this traditional model is referred to as the (semi-analytical) RL (rigid lid) model (see Figure 3).

² The only non-analytical aspect of the semi-analytical procedure is the numerical solution of a matrix system accounting for the generation of overtides due to tide-topography interactions.

³ Monochromatic bedforms are described by a single sinusoidal component (with a single wavenumber).

⁴ Multichromatic bedforms are described by multiple sinusoidal components (with different wavenumbers).

First, a model is formulated for a propagating tidal wave in a tidal channel. This model consists of the depth-averaged hydrodynamic equations, a simple sediment transport formula and a sediment conservation equation for the bed evolution. Moreover, boundary conditions are defined that allow a tidal wave to propagate in the positive along-channel direction. This model formulation strictly applies to the NRL model.

Next, we seek a spatially variant basic state for the NRL model, retaining a relatively flat bed but allowing for a propagating tidal wave. A scaling procedure is performed to analyse the relative importance of each of the terms in the model equations on different spatial and temporal scales and to identify several dimensionless parameters. The rigid lid assumption is not applied in this scaling procedure. Because of this, the free surface effects due to a propagating tidal wave are considered in the NRL model. An expansion in the Froude number is used to obtain a spatially variant solution to the basic state for the NRL model. In traditional linear stability models (see RL models in Figure 3), the basic flow is spatially uniform, thereby directly implying that the bed remains flat. This is however not the case for the NRL model due to the spatially variant basic flow caused by a propagating tidal wave. The sensitivity of the bed evolution in the spatially variant basic state must therefore be analysed to determine if the bed remains relatively flat under a propagating tidal wave.

For traditional linear stability models, with a spatially uniform basic flow, the solution to the perturbed state can be obtained using a semi-analytical solution procedure (see semi-analytical RL model in Figure 3). This procedure breaks down when the solution to the basic state is spatially variant. Therefore, a numerical procedure is required to obtain the solution to the perturbed state for the NRL model. This numerical procedure is first applied to a linear stability model in which the rigid lid assumption is used (see numerical RL model in Figure 3). This is done to validate the numerical solution procedure. To construct the RL models, a separate scaling procedure is performed in which the rigid lid assumption is applied. Next, a spatially uniform basic state is defined. This is followed by the use of the numerical procedure to obtain the solution to the perturbed state. Note that the semi-analytical solution procedure is not explicitly described in this study. As part of this numerical procedure, a generalised eigenvalue problem for the evolution of the perturbed state is defined. The eigenvectors and eigenvalues that follow from this problem describe the structure of the bedforms and can be used to determine other bedform characteristics (i.e., growth rate, cross-channel mode and wavelength). The numerical procedure is validated by comparing the numerical solutions to those obtained using the semi-analytical solution procedure (see arrow A in Figure 3).

Next, the numerical solution procedure for the perturbed state is applied to the NRL model in which a propagating tidal wave is considered. The (numerical) solutions for the NRL model are compared to the (semi-analytical) solutions for the RL model (see arrow B in Figure 3). Several aspects of these solutions are noted, interpreted and discussed. From these aspects, statements are derived regarding the influence of a propagating tidal wave on the formation of tidal bars.

Figure 3 contains an overview of the models used throughout this study (shaded rounded rectangles), including the relations between these models (arrows), the chapters in which these models are used (areas separated by dashed lines) and the characteristics of these models (table). Note that Chapter 2 contains a model formulation that strictly applies to the NRL model. However, this model formulation is altered (as described in Section 4.1) to comply with the RL models.

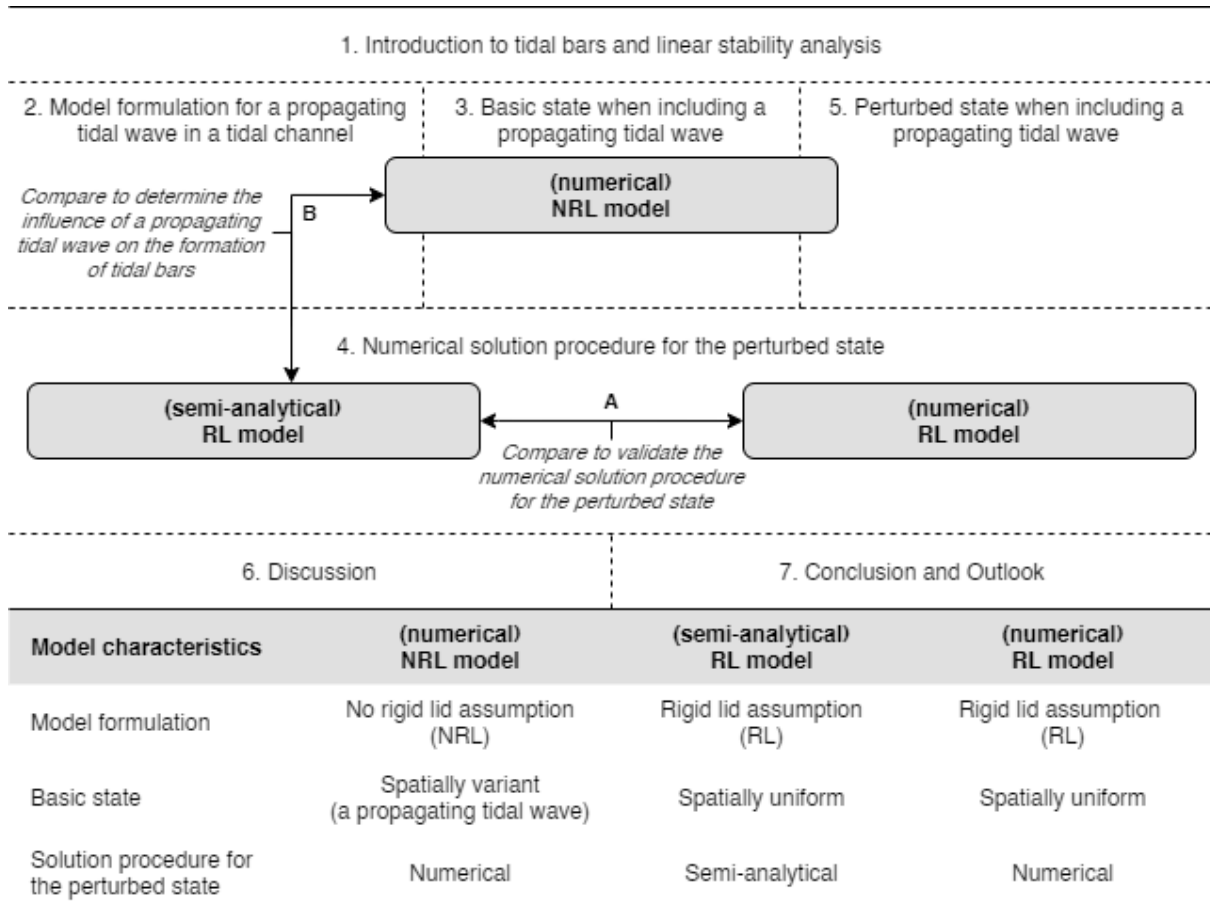


Figure 3: Overview of the linear stability models that are used throughout this study (shaded rounded rectangle), including, the relations between these models (arrows), the chapters in which these models are used (areas separated by dashed lines) and the characteristics of these models (table).

1.6 Report structure

The report is structured as follows. Chapter 2 contains the model formulation for the NRL model in which a propagating tidal wave is considered (RQ1). This chapter contains descriptions of the geometry, hydrodynamics, sediment transport and bed evolution. In Chapter 3, the spatially variant solution to the basic state is determined for the NRL model (RQ2). This chapter contains a scaling procedure in which the rigid lid assumption is not applied, a spatially variant solution to the basic state and an analysis of the sensitivity of the bed evolution under a propagating tidal wave. In Chapter 4, the numerical solution procedure for the perturbed state is described and applied to the RL model (RQ3). This chapter contains a separate scaling procedure in which the rigid lid assumption is applied, a spatially uniform solution to the basic state, the numerical solution procedure for the perturbed state and a comparison between the numerical and semi-analytical solutions. In Chapter 5, the numerical solution procedure is applied to the NRL model in which a propagating tidal wave is considered (RQ4). This chapter contains the numerical solution for the perturbed state, followed by a comparison between the solutions for the NRL and RL model. Chapter 6 contains the discussion in which the results for the NRL model are interpreted and discussed, statements are derived regarding the influence of a propagating tidal wave on the formation of tidal bars (RQ5) and the NRL model is evaluated. Finally, Chapter 7 contains the conclusion in which the research questions are answered, and an outlook is given on further research regarding the influence of a propagating tidal wave on the formation of rhythmic bed features.

2. Model formulation for a propagating tidal wave in a tidal channel

This chapter contains the model formulation for the NRL model in which a propagating tidal wave is considered (see Figure 3).

2.1 Model outline

A simple model is formulated for a propagating tidal wave in a straight tidal channel. To keep this model as simple as possible, only the physical processes of the system are captured that are essential for this study. A model domain is defined with a fixed channel width, with closed boundaries on either side, and a fixed channel length, with open boundaries on either side. Because we want to analyse the influence of a propagating tidal wave, the domain length is equal to the tidal wavelength, i.e., 475 km based on the tidal wave for the reduced friction case (see Figure 5). Similar to previous linear stability studies for tidal bars and sand banks (i.e., Hepkema et al., 2019, 2020; Hulscher et al., 1993; Huthnance, 1982a, 1982b; Schramkowski et al., 2002), the flow is modelled using a depth-averaged approach, thereby neglecting its vertical structure. The Coriolis effect is not considered, because the width of the tidal channel is small compared to the Rossby deformation radius, i.e., $R^* = \sqrt{g^* H^*} / |f^*| \approx 66$ km based on the Coriolis parameter $f^* = 1.15 \cdot 10^{-4} \text{ s}^{-1}$ (for 52° N) and the other parameters in Table 1. Boundary conditions are defined that allow a tidal wave to propagate in the positive along-channel direction. A simple sediment transport formula is used to model bed load transport. As mentioned by Hepkema et al. (2020), this transport formula corresponds to most bed load and total load sediment transport formulations depending on the different choices for the parameter values (Soulsby, 1997). Because of this, and to keep the model as simple as possible, suspended load is not modelled using a separate formula. Lastly, a sediment conservation equation is used to model the bed evolution.

2.2 Geometry

The model is used to analyse the formation of tidal bars in a straight tidal channel. The model geometry under consideration therefore consists of a two-dimensional rectangular channel with a length L_{dom}^* , constant width B^* and mean water depth H^* . A schematic representation of the model geometry is shown in Figure 4.

The model uses the coordinate system $\mathbf{x}^* = [x^*, y^*, z^*]$, in which x^* and y^* are the along-channel and cross-channel coordinates, respectively. The corresponding depth-averaged flow velocities are denoted by $\mathbf{u}^* = [u^*, v^*]^T$. The flow in the channel is induced by a M_2 tide (with free surface amplitude Z^* , typical velocity U^* and frequency ω^*). z^* is the vertical coordinate, with $z^* = \zeta^*$ is the free surface level, where ζ^* is the free surface elevation, and $z^* = -H^* + h^*$ is the bed level, where H^* is the mean water depth and h^* is the bed topography. Both ζ^* and h^* depend on the horizontal coordinates x^* and y^* as well as on time t^* . Note that vectors are denoted using bold symbols (e.g., \mathbf{x}^*) and dimensional quantities are denoted by an asterisk (*). An overview of the model parameters, and their values for the Western Scheldt in the Netherlands, is given in Table 1.

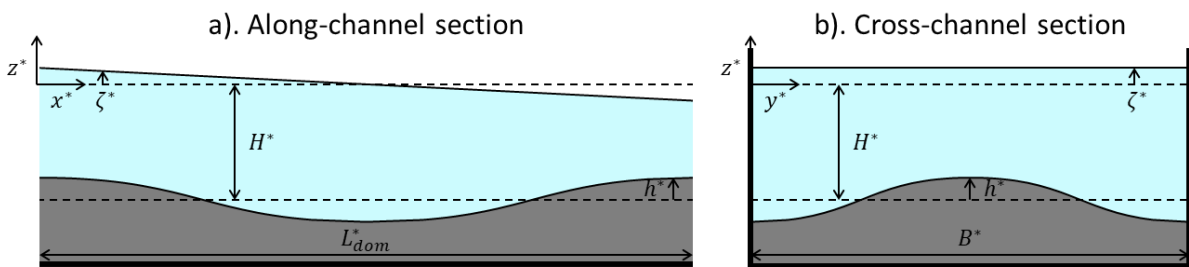


Figure 4: Schematic representation of the model geometry: (a) the along-channel section in the (x, z) -plane; and (b) the cross-channel section in the (y, z) -plane. x^* , y^* and z^* denote the axes of the three-dimensional coordinate system (x^* is along-channel direction and y^* is the cross-channel direction); L_{dom}^* is the domain length; B^* is the channel width; H^* is the mean water depth; ζ^* is the free surface elevation; and h^* is the bed topography.

Table 1: Overview of the model parameters and their values for two cases in the Western Scheldt: the standard friction case and the reduced friction case (altered values are given between parentheses).

Model parameter	Symbol	Value ³	Unit
Domain length	L_{dom}^*	475	km
Channel width ¹	B^*	5	km
Mean water depth ¹	H^*	10	m
Amplitude of free surface elevation	Z^*	1	m
Amplitude of the depth-averaged flow velocity ²	U^*	0.99	m s^{-1}
Tidal frequency (M_2 tide) ¹	ω^*	$1.4 \cdot 10^{-4}$	rad s^{-1}
Tidal wavenumber (M_2 tide) ²	k^*	$1.4 \cdot 10^{-5}$	rad m^{-1}
Gravitational acceleration	g^*	9.81	m s^{-2}
Linear friction coefficient ²	r^*	$2.1 \cdot 10^{-3}$ ($9.5 \cdot 10^{-5}$)	m s^{-1}
Bed load coefficient ¹	α^*	$3.0 \cdot 10^{-4}$ ($1.4 \cdot 10^{-5}$)	$\text{m}^{2-b_1} \text{s}^{b_1-1}$
Bed load exponent for the drag term ¹	b_1	3.0	–
Bed load exponent for the slope term ¹	b_2	2.0	–
Bed slope correction coefficient ¹	λ^*	5.0	$[\text{m s}^{-1}]^{b_1-b_2}$
Bed porosity ¹	p	0.4	–
Morphological time scale ²	T_m^*	46 (1077)	yr

¹Values from Hepkema et al. (2020). ²Values calculated using the equations in this report. ³A reduced friction case is analysed in which the linear friction coefficient (r^*) and bed load coefficient (α^*) are reduced such that the amplitude of the tidal wave remains approximately constant over the model domain (i.e., one tidal wavelength). The coefficients for the reduced friction case (given between parentheses) are obtained by multiplying the coefficients (r^* and α^*) for the standard friction case by 1/22. These altered coefficients (r^* and α^*) are used in the equations in this report to determine the other coefficients for the reduced friction case (e.g., T_m^*).

2.3 Hydrodynamics

The depth-averaged (2DH) shallow water equations, consisting of a continuity equation and two momentum equations, are used to model the conservation of mass and momentum:

$$\frac{\partial(\zeta^* - h^*)}{\partial t^*} + \frac{\partial[(H^* + \zeta^* - h^*)u^*]}{\partial x^*} + \frac{\partial[(H^* + \zeta^* - h^*)v^*]}{\partial y^*} = 0, \quad (5)$$

$$\frac{\partial u^*}{\partial t^*} + u^* \frac{\partial u^*}{\partial x^*} + v^* \frac{\partial u^*}{\partial y^*} + g^* \frac{\partial \zeta^*}{\partial x^*} + \frac{r^* u^*}{H^* + \zeta^* - h^*} = 0, \quad (6)$$

$$\frac{\partial v^*}{\partial t^*} + u^* \frac{\partial v^*}{\partial x^*} + v^* \frac{\partial v^*}{\partial y^*} + g^* \frac{\partial \zeta^*}{\partial y^*} + \frac{r^* v^*}{H^* + \zeta^* - h^*} = 0. \quad (7)$$

In these equations, g^* is the gravitational acceleration; and $r^* = 8c_d^*U^*/(3\pi)$ is the linear friction coefficient, where $c_d^* = 2.5 \cdot 10^{-3}$ is the drag coefficient of the sediment (Zimmerman, 1982).

A boundary condition is imposed at $x^* = 0$ which demands that both the free water surface (ζ^*) and along-channel flow velocity (u^*) must follow sinusoidal wave descriptions (in time):

$$\zeta^*(t^*) = Z^* \cos(\omega^* t^*), \quad u^*(t^*) = U^* \cos(\omega^* t^* - \varphi), \quad \text{at } x^* = 0, \quad (8)$$

in which φ is the phase lag between the sinusoidal wave for the free water surface and along-channel flow velocity. Moreover, the sinusoidal waves are only allowed to propagate in the positive along-channel direction (i.e., positive x -direction).

The boundary conditions that are imposed at the sides of the channel demand that there is no transport of water through these boundaries:

$$v^* = 0, \quad \text{at } y^* = 0, B^*. \quad (9)$$

Initial conditions are not defined since the hydrodynamic system is assumed to be in a dynamic equilibrium response to an external wave forcing.

2.4 Sediment transport

Sediment transport is assumed to be only due to bed load transport. Sediment transport is therefore modelled using an empirical bed load transport formula. This formula is analogue to the one used in most linear stability studies (e.g., Hulscher, 1996; Hulscher et al., 1993), but with separate bed load exponents for the drag and slope terms. The bed load exponent is separated to make the formula compatible with the numerical solution procedure for the perturbed state (see Chapter 4). In this transport formula, bed load is described as a power of the flow velocity with a bed slope correction:

$$\mathbf{q}^* = \alpha^* \left(|\mathbf{u}^*|^{b_1} \frac{\mathbf{u}^*}{|\mathbf{u}^*|} - |\mathbf{u}^*|^{b_2} \lambda^* \nabla^* h^* \right), \quad (10)$$

where, $\mathbf{q}^* = [q_x^*, q_y^*]^T$ is the volumetric bed load sediment flux; α^* is the bed load coefficient; b_1 and b_2 are the bed load exponents for the drag term and slope term, respectively; and λ^* is the bed slope correction coefficient. Moreover, in this vector notation, $\nabla^* = [\partial/\partial x^*, \partial/\partial y^*]^T$ is the nabla operator. This sediment transport formula does not consider a critical shear stress.

2.5 Bed evolution

The bed evolution, due to bed load transport, is modelled using the Exner equation stating conservation of sediment (Exner, 1920, 1925):

$$(1 - p) \frac{\partial h^*}{\partial t^*} = -\nabla^* \cdot \mathbf{q}^*, \quad (11)$$

where, p is the porosity of the bed (usually $p = 0.4$). Combining the Exner equation with the sediment transport formula in Eq.(10) results in:

$$(1 - p) \frac{\partial h^*}{\partial t^*} = -\alpha^* \nabla^* \cdot \left(|\mathbf{u}^*|^{b_1} \frac{\mathbf{u}^*}{|\mathbf{u}^*|} - |\mathbf{u}^*|^{b_2} \lambda^* \nabla^* h^* \right). \quad (12)$$

Hereafter, the bed evolution equation in Eq.(12) is considered instead of Eq.(10) and Eq.(11). The thus eliminated system variables for the bed load sediment fluxes (q_x and q_y) are therefore also omitted from the mathematical description for the state of the system (see Eq.(1)).

3. Basic state when including a propagating tidal wave

In this chapter the solution to the basic state is determined for the NRL model in which a propagating tidal wave is considered (see Figure 3).

3.1 Scaling procedure without rigid lid assumption

3.1.1 Scaled coordinates and variables

The coordinates and variables of the NRL model are scaled as follows:

$$\begin{aligned} \mathbf{x} &= \mathbf{x}^* k^*, & t &= t^* \omega^*, & \tau &= \frac{t^*}{T_m^*}, \\ \zeta &= \frac{\zeta^*}{Z^*}, & \mathbf{u} &= \frac{\mathbf{u}^*}{U^*}, & h &= \frac{h^*}{H^*}, \end{aligned} \quad (13)$$

in which:

$$U^* = \sqrt{\frac{g^*}{H^*}} Z^*, \quad T_m^* = \frac{(1-p)H^*}{\alpha^* k^*} U^{*-b_1}. \quad (14)$$

In the first expression, $\mathbf{x} = [x, y]$ are the dimensionless horizontal spatial coordinates; and k^* is the tidal wavenumber, which is used to define the horizontal length scale ($1/k^*$). The second and third expression show that the problem has two time scales: the tidal time scale ($1/\omega^*$) with coordinate t and the morphological time scale (T_m^*) with coordinate τ . In the other expressions, the scaled variables (ζ , \mathbf{u} and h) are the dimensionless versions of their dimensional counterparts (ζ^* , \mathbf{u}^* and h^*).

The model equations are scaled using these nondimensional coordinates and variables and the dispersion relation for shallow water waves (Phillips, 1977):

$$\omega^{*2} = g^* H^* k^{*2}. \quad (15)$$

3.1.2 Scaled model equations

The model equations are scaled using the abovementioned scales and dispersion relation. Note that the rigid lid assumption is not applied when scaling the model equations for the NRL model. The scaled model equations for the NRL model become:

$$\frac{\partial \zeta}{\partial t} + \frac{\partial[(1 + \delta\zeta - h)u]}{\partial x} + \frac{\partial[(1 + \delta\zeta - h)v]}{\partial y} = 0, \quad (16)$$

$$\frac{\partial u}{\partial t} + \delta u \frac{\partial u}{\partial x} + \delta v \frac{\partial u}{\partial y} + \frac{\partial \zeta}{\partial x} + \frac{ru}{1 + \delta\zeta - h} = 0, \quad (17)$$

$$\frac{\partial v}{\partial t} + \delta u \frac{\partial v}{\partial x} + \delta v \frac{\partial v}{\partial y} + \frac{\partial \zeta}{\partial y} + \frac{rv}{1 + \delta\zeta - h} = 0, \quad (18)$$

$$\frac{\partial h}{\partial \tau} = -\nabla \cdot \langle |\mathbf{u}|^{b_1} \frac{\mathbf{u}}{|\mathbf{u}|} - |\mathbf{u}|^{b_2} \lambda \nabla h \rangle. \quad (19)$$

Here, $\langle \cdot \rangle$ denotes averaging over a tidal period. The morphological time scale is relatively large (see Table 1). The bed topography will thus hardly vary on the tidal time scale. This implies that the bed topography (h) is effectively a function of the slow morphological time (τ). Therefore, the hydrodynamic variables (ζ , u and v) directly depend on the tidal time (t) and are only indirectly dependent on the morphological time through $h(\tau)$. Moreover, the relatively slow evolution of the bed topography is not directly determined by the sediment transport within a tidal cycle, but rather by the tidally averaged (or net) sediment fluxes. This explains the tidally averaged sediment fluxes in Eq.(19). To compute these fluxes, the hydrodynamic equations must be solved at the tidal time scale.

Scaling the boundary conditions given in Eq.(8) and Eq.(9) results in:

$$\zeta(t) = \cos(t), \quad u(t) = \cos(t - \varphi), \quad \text{at } x = 0, \quad (20)$$

$$v = 0, \quad \text{at } y = 0, B. \quad (21)$$

The flowing dimensionless parameters are used in the scaled equations and boundary conditions for the NRL model:

$$\begin{aligned} L_{dom} &= L_{dom}^* k^*, & B &= B^* k^*, & \delta &= \text{Fr} = \frac{Z^*}{H^*}, & r &= \frac{r^*}{H^* \omega^*}, \\ \lambda &= \lambda^* k^* H^* U^{*b_2-b_1}, & T_m &= T_m^* \omega^* = \frac{(1-p)H^* \omega^*}{\alpha^* k^* U^{*b_1}}, \end{aligned} \quad (22)$$

where, δ is the ratio between the amplitude of the free surface wave and the mean water depth. In this case δ is equal to the Froude number $\text{Fr} = U^*/\sqrt{g^*H^*}$, since $U^* = \sqrt{g^*/H^*}Z^*$ (see Subsection 1.2.2). The other parameters (L_{dom} , B , r , λ and T_m) are the dimensionless versions of their dimensional counterparts (L_{dom}^* , B^* , r^* , λ^* and T_m^*). An overview of the dimensionless parameters, and their values for the Western Scheldt, is given in Table 2.

Table 2: Overview of the dimensionless parameters and their values for the Western Scheldt.

Dimensionless model parameter	Symbol	Value ^{1,2}	Expression
Dimensionless channel length	L_{dom}	6.8	$L_{dom}^* k^*$
Dimensionless channel width	B	$7.1 \cdot 10^{-2}$	$B^* k^*$
Ratio between the amplitude of the free surface wave and the mean water depth (equal to Fr)	δ	0.1	Z^*/H^*
Dimensionless linear friction coefficient	r	1.5 ($6.8 \cdot 10^{-2}$)	$r^*/(H^* \omega^*)$
Dimensionless bed slope correction coefficient	λ	$7.2 \cdot 10^{-4}$	$\lambda^* k^* H^* U^{*b_2-b_1}$
Dimensionless morphological time scale	T_m	$2.0 \cdot 10^5$ ($4.5 \cdot 10^6$)	$T_m^* \omega^*$

¹Values are based on Table 1. ²Altered values for the reduced friction case are given between parentheses.

3.2 Spatially variant basic state

3.2.1 Formulation of the spatially variant basic state

The basic state (ϕ_0) for the NRL model is described as a unidirectional flow in the along-channel direction over a flat bed. This is symbolically written as:

$$\phi_0 = [\zeta_0, u_0, 0, 0]^T, \quad (23)$$

since, $v_0 = 0$, and $h_0 = 0$. The hydrodynamic model equations for the basic state become:

$$\frac{\partial \zeta_0}{\partial t} + \frac{\partial u_0}{\partial x} + \delta u_0 \frac{\partial \zeta_0}{\partial x} + \delta \zeta_0 \frac{\partial u_0}{\partial x} = 0, \quad (24)$$

$$\frac{\partial u_0}{\partial t} + \delta u_0 \frac{\partial u_0}{\partial x} + \frac{\partial \zeta_0}{\partial x} + \frac{r u_0}{1 + \delta \zeta_0} = 0. \quad (25)$$

Moreover, the bed is assumed to remain flat in the basic state. If this is indeed the case, the solution for the basic flow should satisfy:

$$\frac{\partial}{\partial x} \langle |u_0|^{b_1-1} u_0 \rangle = 0. \quad (26)$$

3.2.2 Solution to the spatially variant basic state

Assuming the ratio $\delta = Z/H$ is small, we expand the system variables (ϕ_0) in the Froude number:

$$\phi_0 = \phi_{00} + \delta\phi_{01} + \mathcal{O}(\delta^2). \quad (27)$$

This is similar to Hulscher (1993), in which an expansion in the Froude number is used to find a solution to the basic state with flow components in both horizontal directions. The solution obtained by Hulscher is of zeroth order in Froude number (δ^0). In this study, we also use an expansion in the Froude number, but aim to find a solution to the basic state that is of first order (δ^1). Here, including higher order terms is desired, since including these terms results in a more accurate description of the propagating tidal wave.

Applying the expansion (i.e., Eq.(27)) to the model equations in Eq.(24) and Eq.(25) and the boundary conditions in Eq.(20) yields the model equations at the leading order (or zeroth order) (δ^0):

$$\frac{\partial \zeta_{00}}{\partial t} + \frac{\partial u_{00}}{\partial x} = 0, \quad (28)$$

$$\frac{\partial u_{00}}{\partial t} + \frac{\partial \zeta_{00}}{\partial x} + ru_{00} = 0, \quad (29)$$

with boundary conditions⁵:

$$\zeta_{00}(t) = \cos(t), \quad u_{00}(t) = \cos(t - \varphi), \quad \text{at } x = 0. \quad (30)$$

Similarly, the model equations at the first order (δ^1) become:

$$\frac{\partial \zeta_{01}}{\partial t} + \frac{\partial u_{01}}{\partial x} + u_{00} \frac{\partial \zeta_{00}}{\partial x} + \zeta_{00} \frac{\partial u_{00}}{\partial x} = 0, \quad (31)$$

$$\frac{\partial u_{01}}{\partial t} + \frac{\partial \zeta_{01}}{\partial x} + u_{00} \frac{\partial u_{00}}{\partial x} + ru_{01} - r\zeta_{00}u_{00} = 0, \quad (32)$$

with boundary conditions:

$$\zeta_{01}(t) = 0, \quad u_{01}(t) = 0, \quad \text{at } x = 0. \quad (33)$$

A possible solution to the leading order (i.e., Eq.(28) to Eq.(30)), is:

$$\zeta_{00} = \text{Re}\{\exp(i[k_{\oplus}x - t])\}, \quad u_{00} = \text{Re}\left\{\frac{1}{k_{\oplus}}\exp(i[k_{\oplus}x - t])\right\}. \quad (34)$$

Subsequently, the solution to the first order can be found by substituting the solution to the leading order in Eq.(31) and Eq.(32). This results in:

$$\begin{aligned} \zeta_{01} &= \text{Re}\left\{-\frac{3i-2r}{4k_{\oplus}}x \exp(2i[k_{\oplus}x - t]) - \frac{1}{8k_i^2}\left(\frac{k_{\ominus}}{k_{\oplus}} - 1 - ir\left(1 + \frac{k_{\oplus}}{k_{\ominus}} - \frac{k_{\ominus}}{k_{\oplus}}\right)\right)\exp(-2k_ix)\right\}, \\ u_{01} &= \text{Re}\left\{-\left(\frac{3i-2r}{4k_{\oplus}^2}x + \frac{4k_{\oplus}^2-3-2ir}{8k_{\oplus}^3}\right)\exp(2i[k_{\oplus}x - t]) + \frac{ik_{\oplus}}{4k_ik_{\ominus}}\exp(-2k_ix)\right\}. \end{aligned} \quad (35)$$

In these solutions, $k_{\oplus} = \sqrt{1+ir}$ is a complex wavenumber; and $k_{\ominus} = \sqrt{1-ir}$ is the complex conjugate of k_{\oplus} . Moreover, k_r and k_i are the real and imaginary parts of k_{\oplus} , respectively. These complex wavenumbers are thus defined as follows:

⁵ Here the phase lag (φ) cannot be chosen freely but follows from the solution to the leading order (i.e., $\exp(-i\varphi) = 1/k_{\oplus}$). This solution must be a tidal wave that can only propagate in the positive along-channel direction, due to the boundary conditions imposed at $x^* = 0$.

$$k_{\oplus} = k_r + ik_i = \sqrt{1 + ir}, \quad k_{\ominus} = k_r - ik_i = \sqrt{1 - ir}. \quad (36)$$

The solution for the bed evolution in the basic state can be obtained by substituting the expression for the basic flow in Eq.(26). This can be done to analyse if the divergence of the tidally averaged bed transport, and hence the evolution of the bed, is indeed equal to zero, thereby satisfying Eq.(26).

The solutions to the basic state are visualised in Figure 5. This figure shows the free water surface (ζ^*), along-channel depth-averaged velocity (u^*) and bed evolution (dh^*/dt^*) as a function of the along-channel distance. The solutions are shown for the NRL model (see Figure 3) applied to three cases in the Western Scheldt (see Table 1): the case without friction (i.e., the standard friction case with $r^* = 0$ m/s), the reduced friction case and the standard friction case. Here, the case without friction is included to explicitly show why friction must be included in the model.

Figure 5 shows that the solutions for the free water surface and depth-averaged velocity are both described by sinusoidal waves that become increasingly distorted as they travel in the along-channel direction. The distortion of the sinusoidal waves is caused by the phase lag between the solutions for the leading order and first order. Without friction, the amplitude of the tidal wave increases as it propagates in the along-channel direction. Conversely, for the standard friction case, the amplitude of the wave decreases rapidly. For the reduced friction case, the linear friction coefficient is chosen such that the amplitude of the wave remains approximately constant over the model domain (i.e., between $x^* = 0$ and 475 km). Thereafter (i.e., $x^* > 475$ km), the amplitude of the wave decreases slowly.

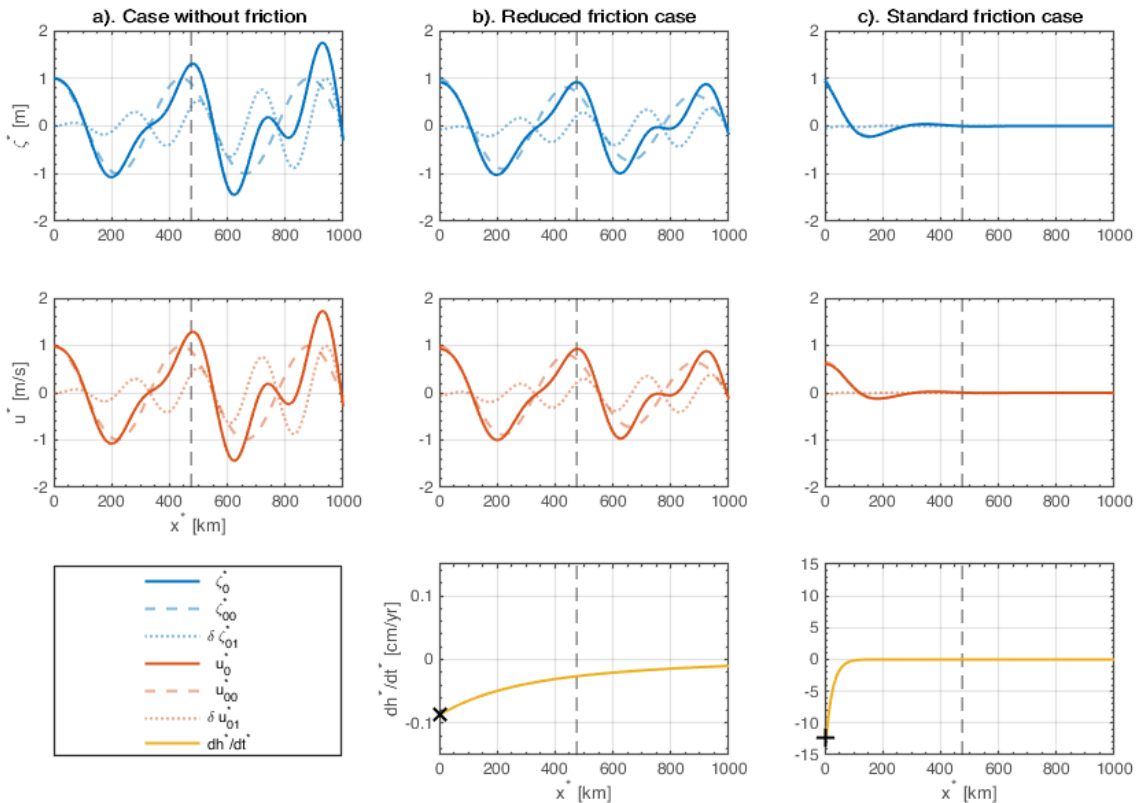


Figure 5: Solutions to the basic state: (top) free water surface (ζ^* in m); (centre) along-channel depth-averaged velocity (u^* in m/s); and (bottom) bed evolution (dh^*/dt^* in cm/yr), all as a function of the along-channel distance (x in km) at $t^* = 0$ s. The solutions are shown for the NRL model (Figure 3) applied to three cases in the Western Scheldt (Table 1): (a) the case without friction (i.e., the standard friction case with $r^* = 0$ m/s); (b) the reduced friction case; and (c) the standard friction case. The solid, dashed and dotted coloured lines represent the total solution, leading order solution and first order solution, respectively. The grey dashed line denotes the length of the model domain (i.e., $L_{dom}^* = 475$ km). \times and $+$ denote the maximum absolute bed evolution for the reduced and standard friction cases in the Western Scheldt, respectively.

Figure 5 also contains the solutions for the bed evolution. Note that the bed evolution is not shown for the case without friction. This is because when friction is neglected, the divergence of the tidally averaged bed transport, and thus the bed evolution, is equal to zero (see Subsection 6.1.1). The solutions for the other cases show that when friction is included, the strongest absolute bed evolution occurs at the left side of the model domain (i.e., at $x^* = 0$ km). Moreover, the standard friction case has a stronger and more localised erosion of the bed at the left side of the domain. The influence of multiple parameters on the maximum bed evolution is further analysed in Section 3.3.

Finally, it should be noted that this spatially variant solution to the basic state is only valid up to an along-channel distance of $\delta x \ll 1$, since the solution is of first order in Froude number (δ^1). For the Western Scheldt this implies $x^* \ll \sim 700$ km. The solution to the basic state is therefore considered to be sufficiently accurate, since the model has a domain length of 475 km and tidal bars have typical wavelengths between 1 and 15 km (Hepkema et al., 2019).

3.3 Sensitivity of the bed evolution in the spatially variant basic state

The basic state must represent a steady system with a flow over a flat bed, i.e., without rhythmic bedforms (Dodd et al., 2003). When the rigid lid assumption is applied, as is the case for the RL models, the basic state is characterised by a spatially uniform flow over a flat bed. Because of this, there is no divergence of tidally averaged bed transport. Hence, there is no bed evolution (i.e., $dh^*/dt^* = 0$ m/s). The bed thus remains flat in the basic state.

An analysis is performed to determine if the bed in the basic state also remains relatively flat when a propagating tidal wave is considered. The results for this analysis are given in Figure 6 to Figure 8. In Figure 6 and Figure 7, the maximum absolute bed evolution (dh^*/dt^*) is shown as a function of the amplitude of the free surface elevation (Z^*) and mean water depth (H^*). These figures correspond to the standard and reduced friction cases in the Western Scheldt (see Table 1), respectively. Similarly, Figure 8 shows the maximum absolute bed evolution as a function of the linear friction coefficient (r^*) and bed load coefficient (α^*). In these figures \dagger and \times denote the standard and reduced friction cases in the Western Scheldt, respectively.

For the standard friction case (see Figure 6), the maximum absolute bed evolution varies between 0 and 100 cm/yr for the analysed parameter regime. For the reduced friction case (see Figure 7) the bed evolution varies between 0 and 2 cm/yr for the same parameter regime. Both figures show that the bed evolution increases for an increasing Froude number. Figure 8 shows that the maximum absolute bed evolution varies between 0 and 25 cm/yr for the analysed parameter regime. The bed evolution is maximised when the linear friction coefficient is $r^* \approx 1.5 \cdot 10^{-3}$ m/s and increases for an increasing bed load coefficient.

In the Western Scheldt, the maximum absolute bed evolution is approximately 12.3 cm/yr for the standard friction case and approximately 0.1 cm/yr for the reduced friction case (see \dagger and \times in Figure 5 to Figure 8, respectively). To conclude if the bed in the basic state remains relatively flat, these values must be compared to the approximated bed evolution in the perturbed state. If the bed evolution in the basic state is small compared to the evolution of the bed in the perturbed state, it is valid to conclude that the bed in the basic state remains relatively flat under a propagating tidal wave. This is important because the basic state must represent a steady system with a flow over a flat bed. The validity of the solution to the basic state for the NRL model is further analysed in Subsection 6.1.1.

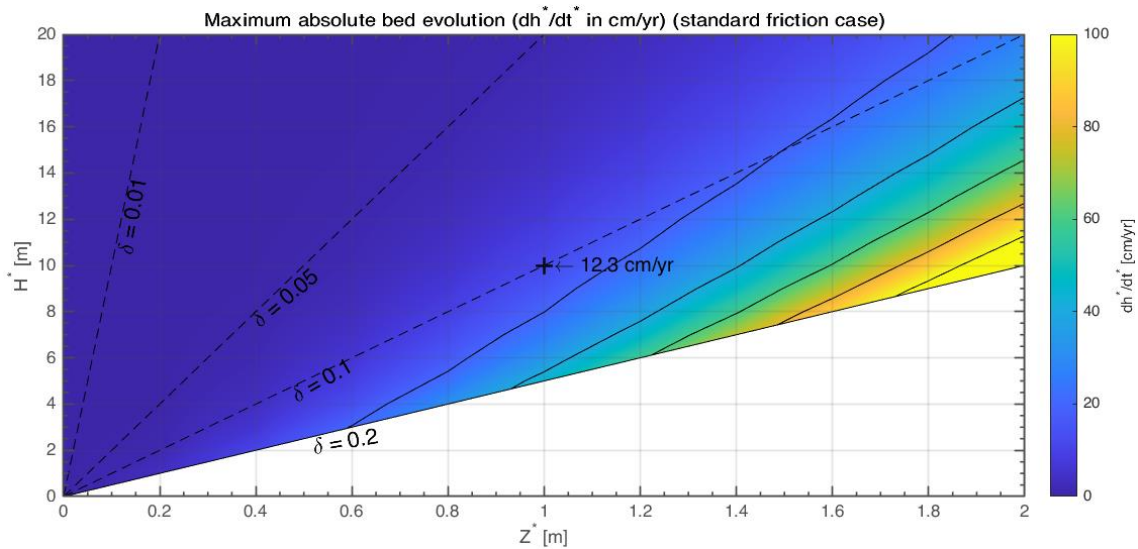


Figure 6: Maximum absolute bed evolution (dh^*/dt^* in cm/yr) as a function of the amplitude of the free surface elevation (Z^* in m) and mean water depth (H^* in m). The bed evolution is shown for the NRL model (Figure 3) applied to the standard friction case in the Western Scheldt (Table 1). The solid contour lines are given on an interval of 20 cm/yr. The dashed lines visualise lines along which the Froude number is constant (0.01, 0.05, 0.1 and 0.2). + denotes the standard friction case in the Western Scheldt.

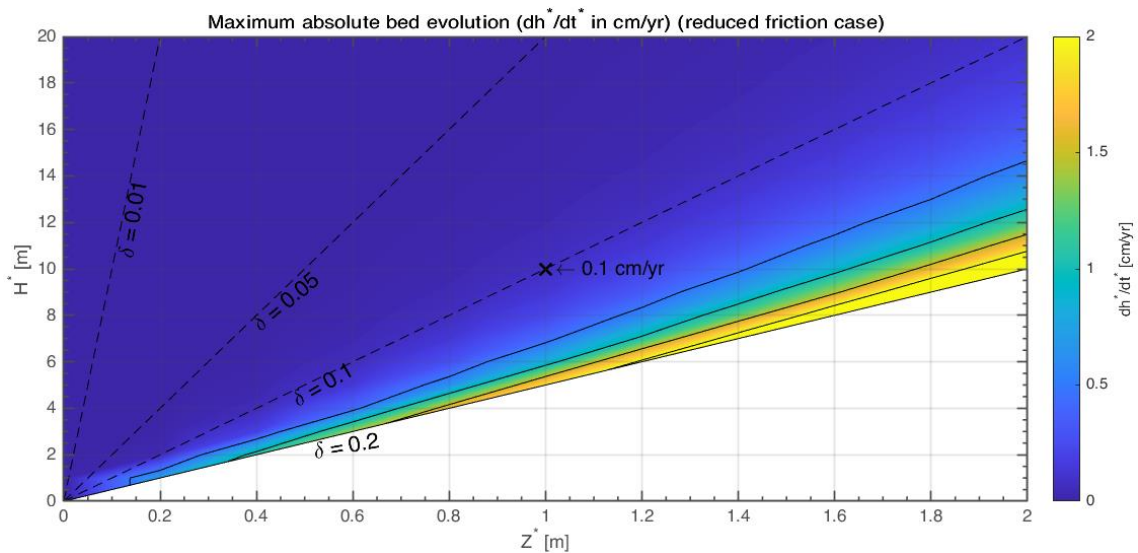


Figure 7: Maximum absolute bed evolution (dh^*/dt^* in cm/yr) as a function of the amplitude of the free surface elevation (Z^* in m) and mean water depth (H^* in m). The bed evolution is shown for the NRL model (Figure 3) applied to the reduced friction case in the Western Scheldt (Table 1). The solid contour lines are given on an interval of 0.5 cm/yr. The dashed lines visualise lines along which the Froude number is constant (0.01, 0.05, 0.1 and 0.2). x denotes the reduced friction case in the Western Scheldt.

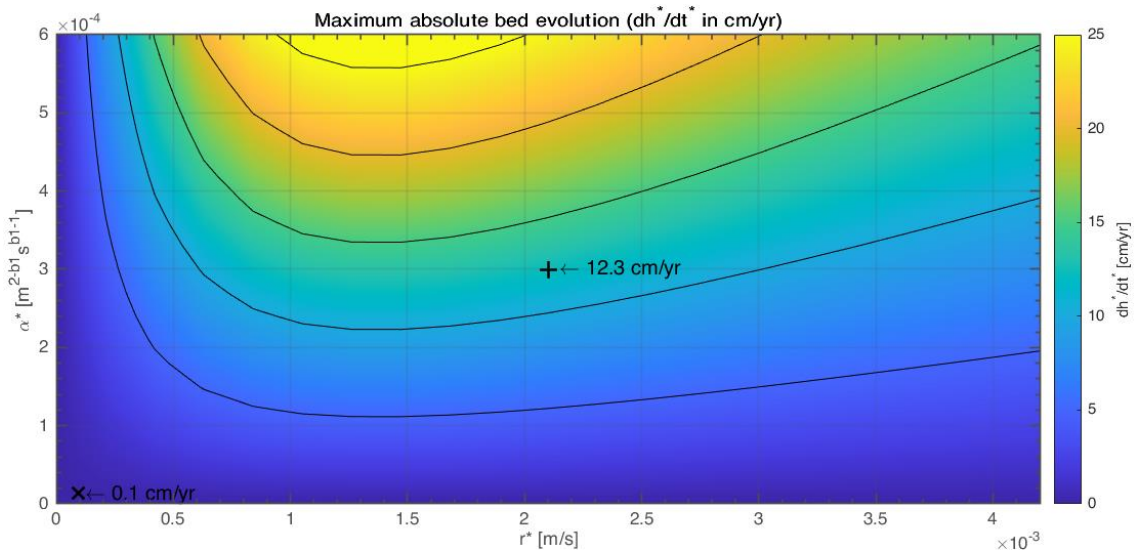


Figure 8: Maximum absolute bed evolution (dh^*/dt^* in cm/yr) as a function of the linear friction coefficient (r^* in m/s) and bed load coefficient (α^* in $m^{2-b_1}s^{b_1-1}$). The bed evolution is shown for the NRL model (Figure 3) applied to the Western Scheldt (Table 1). The solid contour lines are given on an interval of 0.05 m/yr. + and x denote the standard and reduced friction cases in the Western Scheldt, respectively.

4. Numerical solution procedure for the perturbed state

In this chapter the numerical solution procedure for the perturbed state is introduced. Recall that this procedure is developed because the semi-analytical procedure breaks down when the solution to the basic state is spatially variant, as is the case for the NRL model. Here, the numerical procedure is applied to the RL model with a spatially uniform basic state (see Figure 3). This is done to validate the numerical solution procedure. First, the model formulation in Chapter 2 is altered to comply with the RL models. This is done by scaling and altering the equations and boundary conditions such that the model represents a section of the tidal channel that is short compared to the tidal wavelength. This differs from the formulation for the NRL model in Chapter 2, in which the section of the channel is approximately equal to the tidal wavelength. Next, a spatially uniform basic flow is defined for the RL model, thereby directly implying that the bed in the basic state remains flat. Thereafter, the numerical procedure is used to obtain the solutions to the perturbed state. Finally, the numerical solution procedure is validated by comparing these numerical solutions to those obtained using the semi-analytical procedure (see arrow A in Figure 3).

4.1 Scaling procedure with rigid lid assumption

4.1.1 Scaled coordinates and variables

The coordinates and variables of the RL model are scaled as follows:

$$\begin{aligned} \mathbf{x} = \mathbf{x}^* k_m^* = \mathbf{x}^* \frac{\omega^*}{U^*}, \quad t = t^* \omega^*, \quad \tau = \frac{t^*}{T_m^*}, \\ \zeta = \frac{\zeta^*}{\delta Z^*}, \quad \mathbf{u} = \frac{\mathbf{u}^*}{U^*}, \quad h = \frac{h^*}{H^*}, \end{aligned} \quad (37)$$

in which:

$$U^* = \sqrt{\frac{g^*}{H^*} Z^*}, \quad T_m^* = \frac{(1-p)H^*}{\alpha^* \omega^* U^{*b_1-1}}. \quad (38)$$

In the first expression, $k_m^* = \omega^*/U^*$ is the morphological wavenumber. Note that a few of these expressions (for \mathbf{x} , ζ and T_m^*) differ slightly from those used in the NRL model (see Eq.(13) and Eq.(14)). This is because the RL model represents a section of the tidal channel that is short compared to the tidal wavelength, while the NRL model represents a section of the channel that is approximately equal to the tidal wavelength.

4.1.2 Scaled model equations

The rigid lid assumption is applied when scaling the model equations for the RL model. This assumption implies that terms of the order Froude number squared (δ^2) are neglected. This is motivated by the relatively small value of the Froude number (see Table 2). The scaled model equations for the RL model become:

$$\frac{\partial \zeta}{\partial t} + \frac{\partial[(1 + \delta \zeta - h)u]}{\partial x} + \frac{\partial[(1 + \delta \zeta - h)v]}{\partial y} = 0, \quad (39)$$

$$\frac{\partial u}{\partial t} + \delta u \frac{\partial u}{\partial x} + \delta v \frac{\partial u}{\partial y} + \frac{\partial \zeta}{\partial x} + \frac{ru}{1 + \delta \zeta - h} = 0, \quad (40)$$

$$\frac{\partial v}{\partial t} + \delta u \frac{\partial v}{\partial x} + \delta v \frac{\partial v}{\partial y} + \frac{\partial \zeta}{\partial y} + \frac{rv}{1 + \delta \zeta - h} = 0, \quad (41)$$

$$\frac{\partial h}{\partial \tau} = -\nabla \cdot \langle |\mathbf{u}|^{b_1} \frac{\mathbf{u}}{|\mathbf{u}|} \rangle - |\mathbf{u}|^{b_2} \lambda \nabla h, \quad (42)$$

where, strikethroughs (/) show the differences between the scaled model equations for the RL model and the scaled model equations for the NRL model (see Eq.(16) to Eq.(19)).

The RL model represents a section of the tidal channel that is short compared to the tidal wavelength. Therefore, the changes in the position of the free water surface due to a propagating tidal wave are assumed to be uniform over the model domain. The boundary conditions for the propagating tidal wave in Eq.(8) can thus be replaced by periodic boundary conditions that are applied at the open boundaries of the tidal channel (i.e., at $x^* = 0$ and 475 km). The boundary conditions at the sides of the channel for the RL model are equal to those for the NRL model (see Eq.(9)).

In the RL model, the water level gradient terms ($\nabla\zeta$) in Eq.(40) and Eq.(41) can be written as the superposition of two terms:

$$\nabla\zeta = \mathbf{P} + \nabla\tilde{\zeta}. \quad (43)$$

Here, $\mathbf{P} = (P_x, P_y)^T$ is the dimensionless pressure gradient caused by the tidal wave, which varies on the tidal length scale ($1/k^*$); $\nabla\tilde{\zeta}$ is the (dimensionless) free water elevation gradient in response to the bed perturbations, which varies on the morphological length scale ($1/k_m^*$). On the domain of the RL model the pressure gradient \mathbf{P} is considered spatially uniform.

Finally, the dimensionless parameters used to scale the equations and boundary conditions for the RL model are:

$$\begin{aligned} L_{dom} &= L_{dom}^* \frac{\omega^*}{U^*}, & B &= B^* \frac{\omega^*}{U^*}, & \delta &= Fr = \frac{Z^*}{H^*}, & r &= \frac{r^*}{H^* \omega^*}, \\ \lambda &= \lambda^* \omega^* H^* U^{*b_2-b_1-1}, & T_m &= T_m^* \omega^* = \frac{(1-p)H^*}{\alpha^*} U^{*1-b_1}. \end{aligned} \quad (44)$$

Note that a few of these expressions (for L_{dom} , B , λ and T_m) differ slightly from those used in the NRL model (see Eq.(22)).

4.2 Spatially uniform basic state

4.2.1 Formulation of the spatially uniform basic state

The basic state (ϕ_0) for the RL model is described as a unidirectional flow in the along-channel direction over a flat bed. This is symbolically written as:

$$\phi_0 = [0, u_0, 0, 0]^T, \quad (45)$$

since, $\zeta_0 = 0$, $v_0 = 0$ and $h_0 = 0$. In this case, the flow over the flat bed is spatially uniform. This means that $\partial/\partial x = 0$ and $\partial/\partial y = 0$. Therefore, the hydrodynamic model equations for the basic state become:

$$\frac{\partial u_0}{\partial t} + r u_0 + P_x = 0. \quad (46)$$

Moreover, the bed is again assumed to remain flat in the basic state. If this is indeed the case, the basic flow should satisfy:

$$\frac{\partial}{\partial x} (|u_0|^{b_1-1} u_0) = 0. \quad (47)$$

4.2.2 Solution to the spatially uniform basic state

A possible solution to the basic state, which also satisfies the boundary conditions, is a symmetric M_2 tidal current in the along-channel direction:

$$\zeta_0 = 0, \quad u_0 = \cos(t), \quad v_0 = 0. \quad (48)$$

Note that P_x in Eq.(46) must be chosen such that this solution (in Eq.(48)) satisfies Eq.(46). In the RL model, the basic flow is spatially uniform. This directly implies that the bed in the basic state remains flat, because there is no divergence of tidally averaged bed transport, thus satisfying Eq.(47).

4.3 Numerical solution procedure for the perturbed state

4.3.1 Formulation of the perturbed state

The perturbed state (ϕ_1) for the RL model is described as a flow over a perturbed bed. This is symbolically written as:

$$\phi_1 = [\zeta_1, u_1, v_1, h_1]^T. \quad (49)$$

The model equations for the perturbed state for the RL model become:

$$\frac{\partial u_1}{\partial x} - u_0 \frac{\partial h_1}{\partial x} + \frac{\partial v_1}{\partial y} = 0, \quad (50)$$

$$\frac{\partial u_1}{\partial t} + u_0 \frac{\partial u_1}{\partial x} + \frac{\partial \zeta_1}{\partial x} + ru_1 + ru_0 h_1 = 0, \quad (51)$$

$$\frac{\partial v_1}{\partial t} + u_0 \frac{\partial v_1}{\partial x} + \frac{\partial \zeta_1}{\partial y} + rv_1 = 0, \quad (52)$$

$$\frac{\partial h_1}{\partial \tau} = -\nabla \cdot \langle |\mathbf{u}_0|^{b_1-1} \mathbf{u}_1 + (b_1 - 1) |\mathbf{u}_0|^{b_1-3} (\mathbf{u}_0 \cdot \mathbf{u}_1) \mathbf{u}_0 - |\mathbf{u}_0|^{b_2} \lambda \nabla h_1 \rangle. \quad (53)$$

Note that in Eq.(51) and Eq.(52) the tilde on the parameter for the free water elevation in response to the bed perturbations is dropped ($\tilde{\zeta}_1 = \zeta_1$). Additionally, $b_1 = 3$ and $b_2 = 2$ (from Table 1) can be used to rewrite the bed evolution equation in Eq.(53) to:

$$\frac{\partial h_1}{\partial \tau} = -\nabla \cdot \langle |\mathbf{u}_0|^2 \mathbf{u}_1 + 2(\mathbf{u}_0 \cdot \mathbf{u}_1) \mathbf{u}_0 - |\mathbf{u}_0|^2 \lambda \nabla h_1 \rangle. \quad (54)$$

4.3.2 Numerical solution to the perturbed state

The model equations for the perturbed state, together with the boundary conditions, allow for solutions that are linear combinations of:

$$\phi_1(x, y, t) = \begin{bmatrix} \zeta_1(x, y, t) \\ u_1(x, y, t) \\ v_1(x, y, t) \\ h_1(x, y) \end{bmatrix} = \begin{bmatrix} \hat{\zeta}_1(x, t) \cos(n\pi y/B) \\ \hat{u}_1(x, t) \cos(n\pi y/B) \\ \hat{v}_1(x, t) \sin(n\pi y/B) \\ \hat{h}_1(x) \cos(n\pi y/B) \end{bmatrix}, \quad \text{for } n = 0, 1, 2, \dots, \quad (55)$$

where, $\hat{\zeta}_1$, \hat{u}_1 , \hat{v}_1 and \hat{h}_1 are complex valued functions over the along-channel direction and time (except for h_1 which does not directly depend on t); and n is the cross-channel mode number which is related to the number of bars and troughs in the lateral direction of the channel. Figure 9 shows the cross-channel bedform structures for the three lowest cross-channel modes (i.e., $n = 0$ to 2). This figure shows that $n = 0$ implies a spatially uniform cross-channel structure, $n = 1$ implies a structure of alternating bars on either side of the channel and $n = 2$ implies a structure with one bar or trough in the middle of the channel. Substituting Eq.(55) in the model equations for the perturbed state results in a set of 4 linearised equations. These equations are given in Appendix A.1.

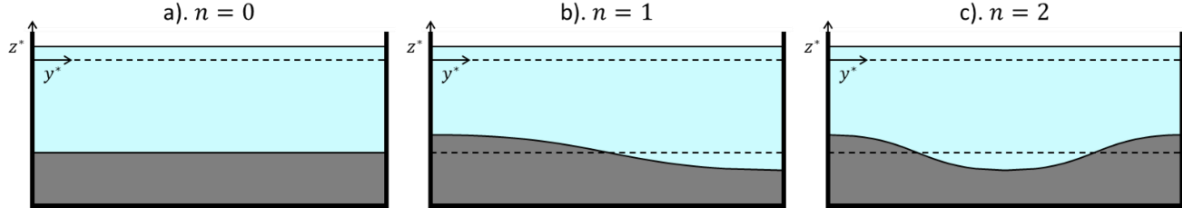


Figure 9: Schematic representation of the cross-channel bedform structures for different cross-channel modes (n): (a) $n = 0$; (b) $n = 1$; and (c) $n = 2$.

Additionally, the solutions for the perturbations of the hydrodynamic variables are expanded as a truncated Fourier series:

$$\begin{bmatrix} \hat{\zeta}_1(x, t) \\ \hat{u}_1(x, t) \\ \hat{v}_1(x, t) \end{bmatrix} = \sum_{p=-P}^P \begin{bmatrix} Z_{1,p}(x) \\ U_{1,p}(x) \\ V_{1,p}(x) \end{bmatrix} \exp(ipt). \quad (56)$$

In the cases presented in this study, the Fourier series is truncated at $P = 2$, thereby including M_0 , M_2 and M_4 tidal components. This allows for the inclusion of the most dominant higher harmonics that are generated by the advection terms. Substituting Eq.(56) in the linearised model equations for the perturbed state results in a set of $3(2P + 4/3)$ equations, which can be solved numerically. These equations are given in Appendix A.1.

Finally, a central difference scheme is used to approximate the first order and second order derivatives in the along-channel direction:

$$\left. \frac{\partial \phi}{\partial x} \right|_{x_m} \approx \frac{\phi_{m+1} - \phi_{m-1}}{2\Delta x}, \quad \left. \frac{\partial^2 \phi}{\partial x^2} \right|_{x_m} \approx \frac{\phi_{m+1} - 2\phi_m + \phi_{m-1}}{(\Delta x)^2}, \quad \text{for } m = 0, \dots, M-1, \quad (57)$$

where, ϕ_m is a system variable at $x = x_m = m \cdot \Delta x$, in which $m = 0, \dots, M-1$ and $\Delta x = L_{dom}/(M-1)$ is the spatial step. Moreover, M is the total number of discretisation points. In this discretisation, periodic boundary conditions are used at either side of the model domain (i.e., at $x_m = 0$ and $x_m = L_{dom}$). This is appropriate for the RL model due to the spatially uniform basic state. Using Eq.(57) to discretise the truncated model equations for the perturbed state results in a set of $3M(2P + 4/3)$ equations. These equations are given in Appendix A.1.

The system of discretised model equations for the perturbed state consists of $3M(2P + 4/3)$ equations and $3M(2P + 4/3)$ variables. A large square matrix (\mathbf{C}) can therefore be constructed in which each column corresponds to a variable of the system and each row represents an equation. This matrix can be used to define a generalised eigenvalue problem for the evolution of the perturbed state:

$$\mathbf{C} \cdot \boldsymbol{\phi}_1 = \frac{\partial}{\partial \tau} \mathbf{G} \cdot \boldsymbol{\phi}_1, \quad (58)$$

where, \mathbf{C} is a square partitioned matrix which contains the system of model equations and variables in the perturbed state; and \mathbf{G} is a partitioned matrix which contains null matrices and one identity matrix. The generalised eigenvalue problem can thus also be written as:

$$\begin{bmatrix} \mathbf{C}_{11} & \mathbf{C}_{12} & \mathbf{C}_{13} & \mathbf{C}_{14} \\ \mathbf{C}_{21} & \mathbf{C}_{22} & \mathbf{C}_{23} & \mathbf{C}_{24} \\ \mathbf{C}_{31} & \mathbf{C}_{32} & \mathbf{C}_{33} & \mathbf{C}_{34} \\ \mathbf{C}_{41} & \mathbf{C}_{42} & \mathbf{C}_{43} & \mathbf{C}_{44} \end{bmatrix} \cdot \begin{bmatrix} \mathbf{Z}_1 \\ \mathbf{U}_1 \\ \mathbf{V}_1 \\ \hat{\mathbf{h}}_1 \end{bmatrix} = \frac{\partial}{\partial \tau} \begin{bmatrix} \mathbf{0} & \mathbf{0} & \mathbf{0} & \mathbf{0} \\ \mathbf{0} & \mathbf{0} & \mathbf{0} & \mathbf{0} \\ \mathbf{0} & \mathbf{0} & \mathbf{0} & \mathbf{0} \\ \mathbf{0} & \mathbf{0} & \mathbf{0} & \mathbf{G}_{44} \end{bmatrix} \cdot \begin{bmatrix} \mathbf{Z}_1 \\ \mathbf{U}_1 \\ \mathbf{V}_1 \\ \hat{\mathbf{h}}_1 \end{bmatrix}, \quad (59)$$

where the colours of the submatrices denote the corresponding model equations (i.e., **continuity**, **x-momentum**, **y-momentum** and **bed evolution**). \mathbf{C}_{11} to \mathbf{C}_{44} are submatrices of \mathbf{C} . Each submatrix corresponds to a subset of variables used in one of the model equations. For example, \mathbf{C}_{11} corresponds to the \mathbf{Z}_1 variables in the continuity equation, and \mathbf{C}_{44} corresponds to the $\hat{\mathbf{h}}_1$ variables in the bed evolution equation. \mathbf{G}_{44} is an identity matrix and corresponds to the term on the left side of the bed evolution equation (e.g. in Eq.(54)). The other submatrices in \mathbf{G} are null matrices (denoted by $\mathbf{0}$). Expanded versions of the \mathbf{C} and \mathbf{G} matrices are given in Appendix B.1. The generalised eigenvalue problem can be rewritten as:

$$\mathbf{C} \cdot \boldsymbol{\varphi}_1 = \boldsymbol{\gamma} \mathbf{G} \cdot \boldsymbol{\varphi}_1, \quad (60)$$

where, $\boldsymbol{\gamma}$ is a square matrix containing $3M(2P + 4/3)$ generalised complex eigenvalues on its diagonal; and $\boldsymbol{\varphi}_1$ is a square matrix in which each column contains a complex eigenvector that corresponds to an eigenvalue in $\boldsymbol{\gamma}$. The M -by- M subsections of $\boldsymbol{\gamma}$ and $\boldsymbol{\varphi}_1$ that correspond to the \mathbf{C}_{44} and \mathbf{G}_{44} submatrices contain values for the complex growth rate and complex structure of the bedforms.

The real part of the complex eigenvectors represents the actual structure of the bedforms in the along-channel direction. In this case, the bedforms have monochromatic structures and can therefore be described using a single wavenumber (k_m) and wavelength ($L_m = 2\pi/k_m$). The real part of the complex growth rate represents the actual growth rate of the bedform (ω_m), while minus the imaginary part represents the speed at which the bedform propagates (c_m) multiplied by the wavenumber. From a mathematical point of view, this can be written as:

$$\boldsymbol{\gamma} = \omega_m - ic_m k_m, \quad (61)$$

where, k_m , ω_m and c_m are the morphological wavenumber, growth rate and migration rate of a bedform structure. The dimensional bedform characteristics are determined according to:

$$k_m^* = k_m \frac{\omega^*}{U^*}, \quad L_m^* = \frac{2\pi}{k_m^*}, \quad \omega_m^* = \frac{\omega_m}{T_m^*}, \quad c_m^* = c_m \frac{U^*}{\omega^* T_m^*}, \quad (62)$$

where, k_m^* , L_m^* , ω_m^* and c_m^* are the dimensional versions of their dimensionless counterparts (k_m , L_m , ω_m and c_m). Finally, the wavenumber and cross-channel mode are determined for the bedform with the maximum growth rate, i.e., the fastest growing mode (FGM):

$$\omega_{m,\text{FGM}}^* = \omega_m^*(k_{m,\text{FGM}}^*, n_{\text{FGM}}) = \max_{k_m^*, n} \{\omega_m^*(k_m^*, n)\}. \quad (63)$$

The FGM is considered the dominant bedform and therefore provides insight into the behaviour of the modelled system.

4.4 Comparison of the numerical and semi-analytical solutions to the perturbed state

The solutions to the perturbed state for the RL model obtained using the numerical procedure are compared to those obtained using the semi-analytical procedure (see arrow A in Figure 3). This is done to validate the numerical solution procedure developed in this study. Figure 10 and Figure 11 contain the growth curves showing the growth rate (ω_m^*) as a function of the morphological wavenumber (k_m^*) for different cross-channel modes (n) and for an increasing number of discretisation points (M). These two figures correspond to the standard and reduced friction cases in the Western Scheldt (see Table 1), respectively. The solid and dashed lines represent the growth curves for the semi-analytical and numerical RL models, respectively. \dagger and \times denote the corresponding semi-analytical FGM and numerical FGM, respectively. Moreover, \bullet denotes the FGM for each individual cross-channel mode. Hereafter, the FGMs for each individual cross-channel mode are referred to as partial fastest growing modes (pFGMs).

It should be noted that as M increases, thereby decreasing the size of the spatial step (Δx), growth rates can be determined for larger morphological wavenumbers. Thus, increasing M does not increase the smoothness of the growth curves within the visualised domain (i.e., $k_m^* = 0$ to 1 km^{-1}), but increases the largest wavenumbers for which the growth curve can be plotted. This can be seen by comparing the subplots in Figure 10 or Figure 11. For example, for $M = 101$ the numerical growth curves end at $k_m^* \approx 0.65 \text{ km}^{-1}$, while for $M = 201$ (and higher) the growth curves continue past the right edge of the visualised domain (i.e., $k_m^* > 1 \text{ km}^{-1}$).

Figure 10 and Figure 11 show that for $M = 101$ the numerical growth curves accurately approximate the corresponding semi-analytical growth curves for small wavenumbers (i.e., $k_m^* \approx 0 \text{ km}^{-1}$), but not for large wavenumbers (i.e., $k_m^* > 0 \text{ km}^{-1}$). As M increases, the numerical growth curves converge to the semi-analytical growth curves. For $M \geq 801$ the numerical growth curves are approximately equal to the corresponding semi-analytical growth curves for the visualised domain (i.e., $k_m^* = 0$ to 1 km^{-1}).

Moreover, as M increases, the growth rate and wavenumber for the numerical FGM (and pFGMs) converges to the semi-analytical FGMs (and pFGMs). This is most clearly visible for the standard friction case (see Figure 10). For this case, the analytical FGM has a wavenumber of $k_m^* = 0.59 \text{ km}^{-1}$ and a cross-channel mode of $n = 2$. The numerical FGM clearly approaches the semi-analytical FGM as M increases. For the standard friction case, the numerical and semi-analytical pFGMs for all cross-channel modes are roughly equal for $M \geq 801$.

For the reduced friction case (see Figure 11), the FGM has a wavenumber of $k_m^* = 0 \text{ km}^{-1}$ and the lowest cross-channel mode (i.e., $n = 0$). The numerical FGM does not become more accurate as M increases, because the numerical growth curves are relatively accurate for small morphological wavenumbers. However, increasing M does increase the accuracy of the numerical pFGMs for all higher cross-channel modes. For the reduced friction case, the numerical and semi-analytical pFGMs for all cross-channel modes are roughly equal for $M \geq 401$.

The results in Figure 10 and Figure 11 show that the numerical and semi-analytical growth curves and FGMs are roughly equal when M is sufficiently large. This implies that the numerical solution procedure can be used to determine the solution to the perturbed state for the NRL model in which a propagating tidal wave is considered (see Chapter 5).

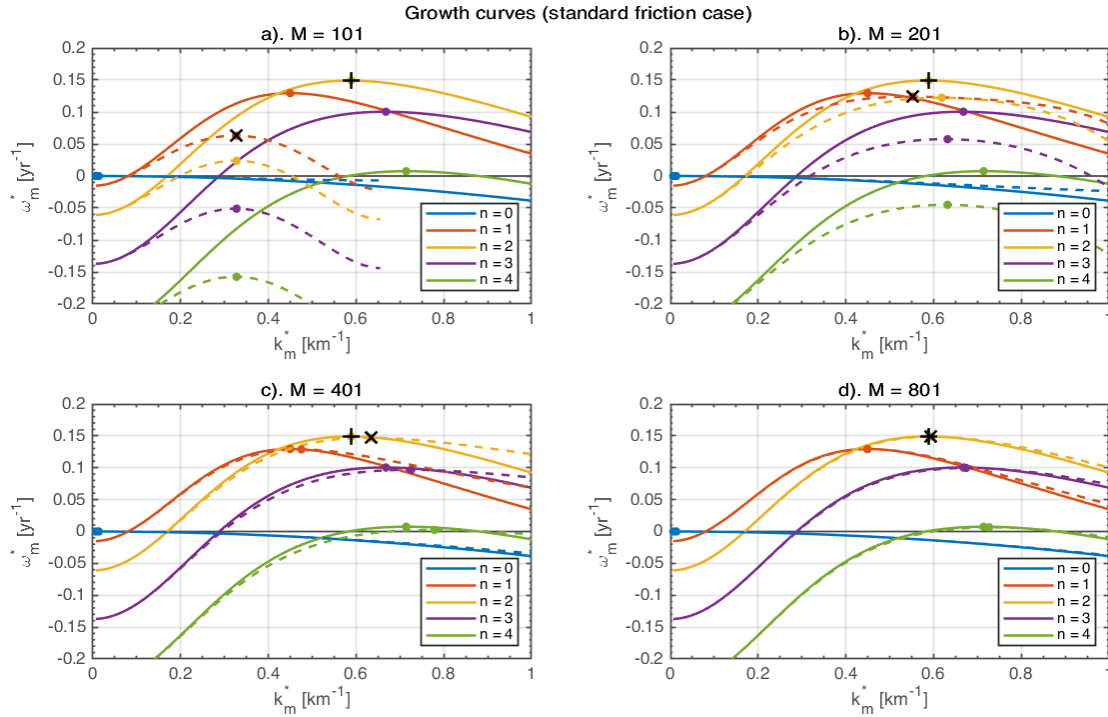


Figure 10: Growth curves showing the growth rate (ω_m^* in yr^{-1}) as a function of the morphological wavenumber (k_m^* in km^{-1}) for different cross-channel modes (n) and for an increasing number of discretisation points (M): (a) $M = 101$; (b) $M = 201$; (c) $M = 401$; and (d) $M = 801$. The growth curves are shown for the standard friction case in the Western Scheldt (Table 1). The solid and dashed lines represent the growth curves for the semi-analytical and numerical RL models (Figure 3), respectively. •, + and × denote the pFGM for each cross-channel mode, the semi-analytical FGM and the numerical FGM, respectively.

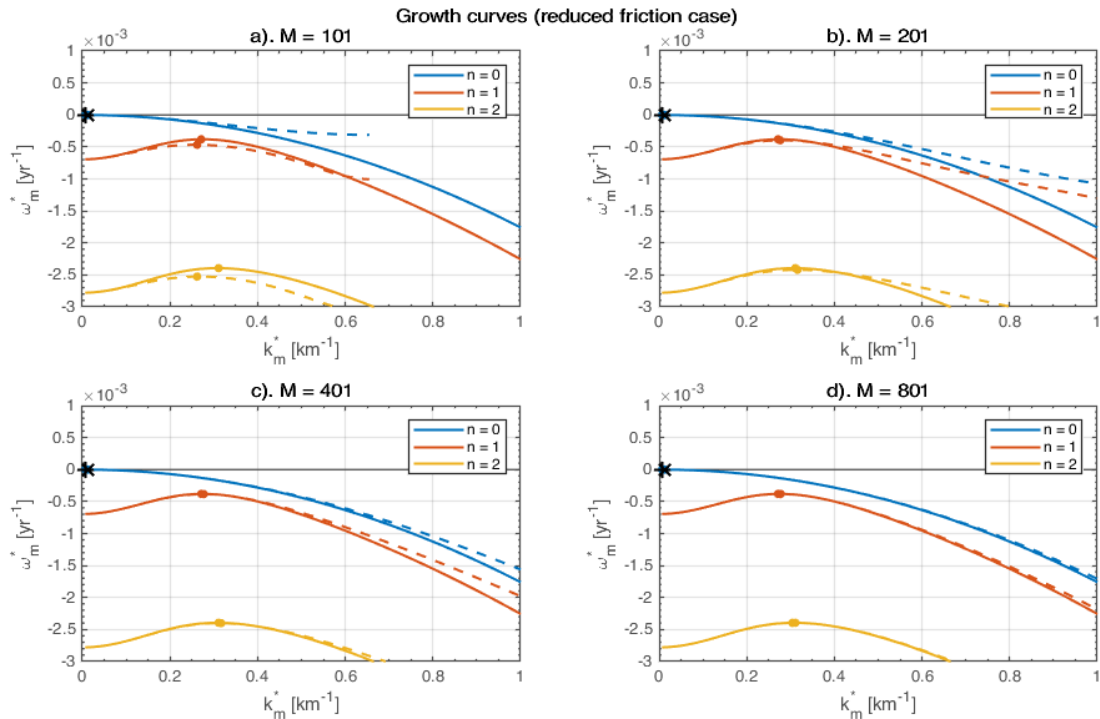


Figure 11: Growth curves showing the growth rate (ω_m^* in yr^{-1}) as a function of the morphological wavenumber (k_m^* in km^{-1}) for different cross-channel modes (n) and for an increasing number of discretisation points (M): (a) $M = 101$; (b) $M = 201$; (c) $M = 401$; and (d) $M = 801$. The growth curves are shown for the reduced friction case in the Western Scheldt (Table 1). The solid and dashed lines represent the growth curves for the semi-analytical and numerical RL models (Figure 3), respectively. •, + and × denote the pFGM for each cross-channel mode, the semi-analytical FGM and the numerical FGM, respectively.

Figure 12 contains the along-channel bedform structures of the pFGMs for the three lowest cross-channel modes (i.e., $n = 0$ to 2). These bedforms are shown for the (semi-analytical) RL model applied to the standard and reduced friction cases in the Western Scheldt (see Table 1). Note that this figure only shows a section of the model domain (i.e., $x^* = 0$ to 100 km).

The bedform of the pFGM for the lowest cross-channel mode (i.e., $n = 0$) is characterised by a spatially uniform structure. This is because the pFGM for $n = 0$ has a wavenumber of $k_m^* = 0 \text{ km}^{-1}$ (see • in Figure 10 and Figure 11). This bedform is spatially uniform, because it has an infinitely long wavelength (i.e., $L_m^* = \infty \text{ km}$). This spatially uniform bedform thus represents a flat bed. Moreover, this bedform has a growth rate of zero, meaning that it will not grow or decay over time. This makes sense because sedimentation or erosion along the whole bed would not satisfy the conservation of sediment in the system. The bedforms of the pFGMs for the higher cross-channel modes (i.e., $n > 0$) are characterised by monochromatic structures with a range of (finite) wavelengths. This is because the pFGMs for these cross-channel modes have wavenumbers of $k_m^* > 0 \text{ km}^{-1}$ (see • in Figure 10 and Figure 11).

Figure 10 shows that the FGM for the standard friction case has a positive growth rate (i.e., $\omega_m^* = 0.15 \text{ yr}^{-1}$). Therefore, the basic state is unstable, meaning the system evolves to a dynamic equilibrium with conditions that roughly agree with those of the FGM. In this case, the FGM has a wavelength of $L_m^* = 10.7 \text{ km}$ and a cross-channel mode of $n = 2$. Figure 13 shows the bedform structure of the FGM found by applying the (semi-analytical) RL model to the standard friction case in the Western Scheldt. Note that this figure only shows a section of the model domain (i.e., $x^* = 0$ to 50 km). Similarly, Figure 11 shows that the FGM for the reduced friction case has a growth rate of zero (i.e., $\omega_m^* = 0 \text{ yr}^{-1}$). This means that all other modes have negative growth rates. Therefore, the basic state is stable, meaning the system evolves back to the basic state (i.e., a flat bed). Based on the growth curves for the (semi-analytical) RL model, the formation of tidal bars is not expected for the reduced friction case in the Western Scheldt.

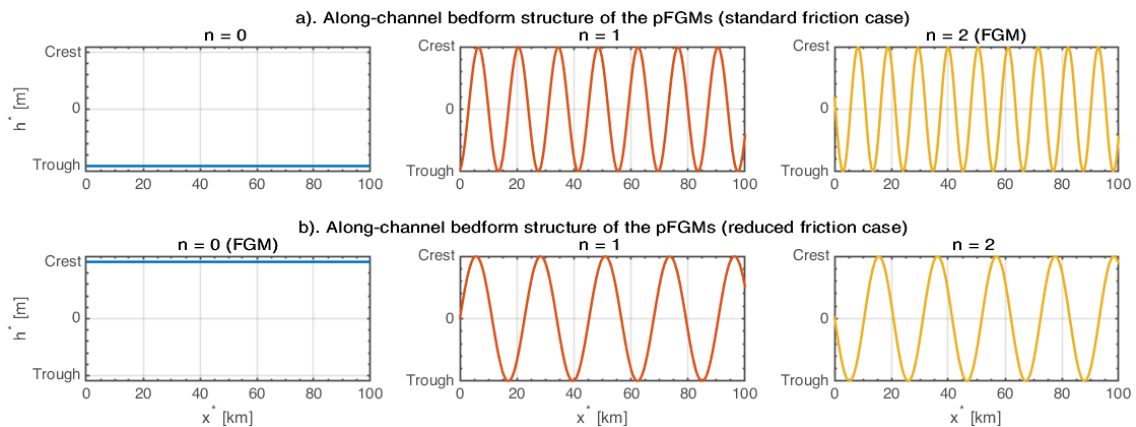


Figure 12: Along-channel bedform structures of the pFGMs for the three lowest cross-channel modes (n). The bedform structures are shown for the (semi-analytical) RL model (Figure 3) applied to two cases in the Western Scheldt (Table 1): (top) standard friction case; and (bottom) reduced friction case.

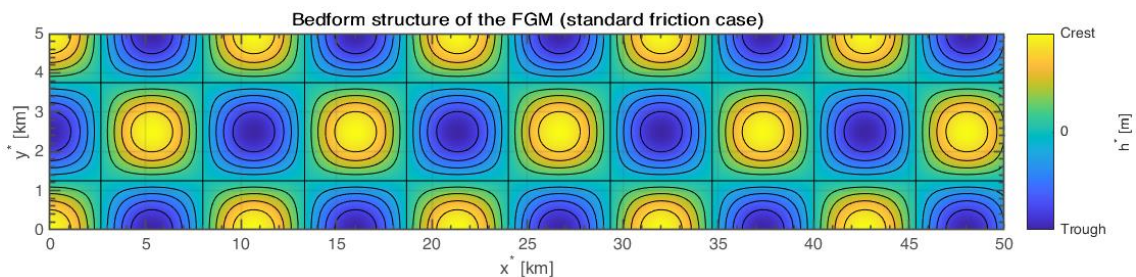


Figure 13: Bedform structure of the FGM. The bedform structure is shown for the (semi-analytical) RL model (Figure 3) applied to the standard friction case in the Western Scheldt (Table 1).

5. Perturbed state when including a propagating tidal wave

In this chapter the numerical solution procedure for the perturbed state is applied to the NRL model in which a propagating tidal wave is considered (see Figure 3). Recall that the semi-analytical solution procedure breaks down when the solution to the basic state is spatially variant. Therefore, a numerical procedure is required to obtain the solution to the perturbed state for the NRL model. The NRL model is formulated in Chapter 2 and the solution to the basic state for this model is determined in Chapter 3. Here, the numerical procedure is used to obtain the solution to the perturbed state for the reduced friction case in the Western Scheldt. In this study, the (numerical) NRL model cannot be applied to the standard friction case in the Western Scheldt due to the periodic boundary conditions used in the discretisation (see Subsection 5.1.2). Finally, the (numerical) solutions for the NRL model are compared to the (semi-analytical) solutions for the RL model (see arrow B in Figure 3). This is done to determine the influence of a propagating tidal wave on the formation of tidal bars (see Subsection 6.1.3).

5.1 Numerical solution procedure for the perturbed state

5.1.1 Formulation of the perturbed state

The perturbed state (ϕ_1) for the NRL model is described as a flow over a perturbed bed. This is symbolically written as:

$$\phi_1 = [\zeta_1, u_1, v_1, h_1]^T. \quad (64)$$

The model equations for the perturbed state for the NRL model become:

$$\begin{aligned} \frac{\partial \zeta_1}{\partial t} + \frac{\partial u_1}{\partial x} - u_0 \frac{\partial h_1}{\partial x} - h_1 \frac{\partial u_0}{\partial x} + \delta u_0 \frac{\partial \zeta_1}{\partial x} + \delta u_1 \frac{\partial \zeta_0}{\partial x} + \delta \zeta_0 \frac{\partial u_1}{\partial x} + \delta \zeta_1 \frac{\partial u_0}{\partial x} + \frac{\partial v_1}{\partial y} \\ + \delta \zeta_0 \frac{\partial v_1}{\partial y} = 0, \end{aligned} \quad (65)$$

$$\frac{\partial u_1}{\partial t} + \delta u_0 \frac{\partial u_1}{\partial x} + \delta u_1 \frac{\partial u_0}{\partial x} + \frac{\partial \zeta_1}{\partial x} + \frac{ru_1}{1 + \delta \zeta_0} + \frac{ru_0(h_1 - \delta \zeta_1)}{(1 + \delta \zeta_0)^2} = 0, \quad (66)$$

$$\frac{\partial v_1}{\partial t} + \delta u_0 \frac{\partial v_1}{\partial x} + \frac{\partial \zeta_1}{\partial y} + \frac{rv_1}{1 + \delta \zeta_0} = 0, \quad (67)$$

$$\frac{\partial h_1}{\partial \tau} = -\nabla \cdot (|\mathbf{u}_0|^2 \mathbf{u}_1 + 2(\mathbf{u}_0 \cdot \mathbf{u}_1) \mathbf{u}_0 - |\mathbf{u}_0|^2 \lambda \nabla h_1). \quad (68)$$

Here, $b_1 = 3$ and $b_2 = 2$ (from Table 1) have been substituted in the bed evolution equation in Eq.(68). The friction terms in the momentum equations are linearised using a geometric series in the Froude number ($Fr = \delta = Z^*/H^*$):

$$\frac{1}{1 + \delta C} = 1 - \delta C + \mathcal{O}(\delta^2), \quad (69)$$

where, C represents a part of the friction terms (e.g., ζ_0). The momentum equations with the linearised friction terms become:

$$\frac{\partial u_1}{\partial t} + \delta u_0 \frac{\partial u_1}{\partial x} + \delta u_1 \frac{\partial u_0}{\partial x} + \frac{\partial \zeta_1}{\partial x} + ru_1 + ru_0 h_1 - \delta r \zeta_0 u_1 - 2\delta r \zeta_0 u_0 h_1 - \delta r u_0 \zeta_1 = 0, \quad (70)$$

$$\frac{\partial v_1}{\partial t} + \delta u_0 \frac{\partial v_1}{\partial x} + \frac{\partial \zeta_1}{\partial y} + rv_1 - \delta r \zeta_0 v_1 = 0. \quad (71)$$

5.1.2 Numerical solution to the perturbed state

As described in Subsection 4.3.2, the model equations for the perturbed state for the NRL model are linearised by substituting the expressions in Eq.(55). This is followed by a truncation and discretisation using the truncated Fourier series in Eq.(56) and the central difference scheme in Eq.(57), respectively. The model equations after each of these transformations are given in Appendix A.2. The transformed model equations are used to construct a square partition matrix (\mathbf{C}) for the generalised eigenvalue problem shown in Eq.(58) to Eq.(60). An expanded version of this \mathbf{C} matrix is given in Appendix B.2.

The discretisation uses periodic boundary conditions at either side of the model domain (i.e., at $x^* = 0$ and 475 km). To correctly use periodic boundary conditions, the solution for the basic flow at the left side of the model domain (i.e., at $x^* = 0$ km) must smoothly match the solution at the right side of the domain (i.e., at $x^* = 475$ km). If this requirement is not met, then the periodic boundary conditions represent interactions that do not naturally occur in the system. These interactions result in (numerical) inaccuracies in the solutions to the perturbed state. The discretisation can also be done with non-periodic boundary conditions. However, the use of these boundary conditions is outside the main scope of this study. Nevertheless, Subsection 6.2.4 and Appendix E do briefly touch on the use of non-periodic boundary conditions in the NRL model.

The abovementioned requirement for periodic boundary conditions is automatically met by the RL model since the basic state is spatially uniform. When a propagating tidal wave is considered, as is the case for the NRL model, this requirement is only met under specific conditions. Figure 5 shows that the solution to the basic state found by applying the NRL model to the reduced friction case seems to satisfy this requirement, since the length of the model domain is equal to one tidal wavelength (i.e., $L_{dom}^* = 475$ km) and the amplitude of the tidal wave remains approximately constant over the model domain. Conversely, this requirement is not satisfied by the solution to the basic state found by applying the NRL model to the standard friction case, since the amplitude of the wave decreases over the model domain (see Figure 5). In this study, the (numerical) NRL model is therefore only applied to the reduced friction case and not to the standard friction case in the Western Scheldt.

Similar to Subsection 4.3.2, the eigenvectors and eigenvalues that follow from the eigenvalue problem are used to determine the structures and characteristics of the bedforms. In the case of a spatially uniform basic state, the bedforms have monochromatic structures and can therefore be described using a single wavenumber and wavelength (see Figure 12). Conversely, a spatially variant basic state results in multichromatic bedforms (see Figure 15). The structures of these bedforms are defined by multiple sinusoidal components each with a different wavenumber. Because of this, it is not possible to simply construct growth curves using the method applied in Chapter 4, in which each eigenvector corresponds to a unique wavenumber.

In this study, a method is developed and used to construct growth curves for multichromatic bedforms. In short, this method uses a discrete Fourier transform to decompose a multichromatic bedform into its monochromatic sinusoidal components. Based on the constructed Discrete Fourier Transform (DFT) spectrum, the growth rate for a particular multichromatic bedform structure is assigned to the three most dominant components that are present in that structure (see \times in Figure 15). This procedure is repeated for all multichromatic bedforms (i.e., all eigenvectors). The highest and lowest growth rates that are assigned to each wavenumber are used to construct a so-called growth area (see shaded areas in Figure 14). Finally, the growth curve is constructed using the upper limit of the growth area (see dashed lines in Figure 14). Appendix D contains a more detailed description of this method.

The horizontal length scale used in the scaling procedure for the NRL model (i.e., $1/k^*$) differs from the one used for the RL model (i.e., $1/k_m^*$). Therefore, the expressions used for the NRL model to scale the bedform characteristics to their dimensional form also differ from those used for the RL model (see Eq.(62)). For the NRL model, the dimensional characteristics are determined according to:

$$k_m^* = k_m k^*, \quad L_m^* = \frac{2\pi}{k_m^*}, \quad \omega_m^* = \frac{\omega_m}{T_m^*}, \quad c_m^* = \frac{c_m}{k^* T_m^*}, \quad (72)$$

where, k_m^* , L_m^* , ω_m^* and c_m^* are the dimensional versions of their dimensionless counterparts (k_m , L_m , ω_m and c_m). Finally, the fastest growing mode (FGM) is again determined according to Eq.(63).

5.2 Numerical solutions to the perturbed state when including a propagating tidal wave

The (numerical) solutions for the NRL model are compared to the (semi-analytical) solutions for the RL model (see arrow B in Figure 3). This is done to determine the influence of a propagating tidal wave on the formation of tidal bars (see Subsection 6.1.3).

Figure 14 contains the growth curves (and areas) showing the growth rate (ω_m^*) as a function of the morphological wavenumber (k_m^*) for different cross-channel modes (n). These growth curves (and areas) are shown for the reduced friction case in the Western Scheldt (see Table 1). The solid lines and dashed lines (with shaded areas) represent the growth curves for the (semi-analytical) RL model and the growth curves (with growth areas) for the (numerical) NRL model, respectively. \dagger and \times denote the FGM for the RL and NRL model, respectively. Moreover, \bullet denotes the partial fastest growing mode (pFGM) for each cross-channel mode. Recall that the pFGMs are the FGM for each individual cross-channel mode.

The following aspects are noted regarding the differences between the growth curves (and areas) for the NRL and RL model (see Figure 14):

- **Computational sawtooth patterns:**
Multiple sections of the (numerical) growth curves for the NRL model are characterised by sawtooth patterns (e.g., around $k_m^* \approx 0 \text{ km}^{-1}$ for $n = 0$; and between $k_m^* \approx 0.37$ and 0.68 km^{-1} for $n = 1$). These computational patterns are caused by the method that is used to construct the growth areas and curves for multichromatic bedforms (see Appendix D).
- **Growth curve (and area) for $n = 0$:**
The growth curve (for $n = 0$) for the NRL model has a steeper slope than the curve for the RL model. Moreover, the growth curve for the NRL model has positive growth rates for wavenumbers between $k_m^* \approx 0$ and 0.33 km^{-1} . Because of this, the growth curve does not approach the origin as the wavenumber decreases to zero. This differs from the growth curve for the RL model, which does approach to origin as the wavenumber decreases to zero.
- **Growth curves (and areas) for $n > 0$:**
The differences between the growth curves (for $n > 0$) for the NRL and RL model are relatively consistent. Firstly, for smaller wavenumbers (i.e., $k_m^* \approx 0 \text{ km}^{-1}$), the growth curves for the NRL and RL models have similar growth rates. Moreover, the peaks of the growth curves for the NRL model are higher and occur at larger wavenumbers compared to the peaks for the RL model. The growth rate and wavenumber of the pFGMs are therefore larger for the NRL model than for the RL model. Finally, for larger wavenumbers (i.e., $k_m^* > 0.5 \text{ km}^{-1}$), the growth curves for the NRL model have steeper slopes than the curves for the RL model. This last difference is also observed for the growth curves for $n = 0$. Although not explicitly shown, the abovementioned aspects also apply to the growth curves and pFGMs for even higher cross-channel modes (i.e., $n = 3$ and 4).

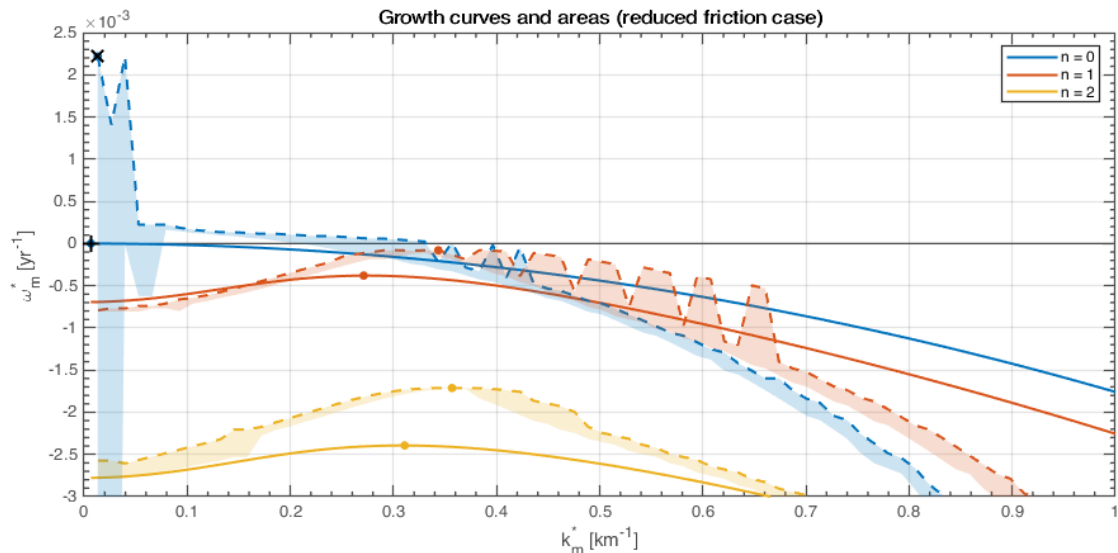


Figure 14: Growth curves (and areas) showing the growth rate (ω_m^* in yr^{-1}) as a function of the morphological wavenumber (k_m^* in km^{-1}) for different cross-channel modes (n). The growth curves (and areas) are shown for the reduced friction case in the Western Scheldt (Table 1). The solid lines and dashed lines (with shaded areas) represent the growth curves for the (semi-analytical) RL model and the growth curves (with growth areas) for the (numerical) NRL model (Figure 3), respectively. •, + and × denote the pFGM for each cross-channel mode, the FGM for the RL model and the FGM for the NRL model, respectively.

Figure 15 contains the along-channel bedform structures of the pFGMs for the three lowest cross-channel modes (i.e., $n = 0$ to 2). The bedforms are shown for the NRL model applied to the reduced friction case in the Western Scheldt (see Table 1). This figure also shows the corresponding Discrete Fourier Transform (DFT) spectra of the pFGMs.

The following aspects are noted regarding the along-channel bedform structures and corresponding DFT spectra for the NRL model (see Figure 15):

- Bedform structure of the pFGM for $n = 0$:**
 The bedform (for $n = 0$) for the NRL model has a spatially variant structure. This differs from the spatially uniform bedform structure for the RL model (see $n = 0$ in Figure 12). The DFT spectrum shows that the most dominant component has a wavelength of $k_m^* = 0 \text{ km}^{-1}$. This is a spatially uniform component, because it has an infinitely long wavelength (i.e., $L_m^* = \infty \text{ km}$). Due to this component, erosion occurs along the whole bed. This cannot satisfy the conservation of sediment in the system. This bedform must therefore have a growth rate of zero, meaning that it will not grow or decay over time. However, the bedform for the NRL model does have a positive growth rate (i.e., $\omega_m^* = 2.2 \cdot 10^{-3} \text{ yr}^{-1}$). This also differs from the bedform (for $n = 0$) for the RL model, which does have a growth rate of zero.
- Bedform structure of the pFGM for $n = 1$:**
 The bedform (for $n = 1$) has a weakly multichromatic structure with an amplitude that remains approximately constant over the model domain. The amplitude of this bedform seems to increase slightly towards the ends of the model domain (i.e., at $x^* = 0$ and 475 km). The DFT spectrum shows that the dominant monochromatic components have wavelengths that vary over a wider range (three separate peaks). Moreover, the spatially uniform component (i.e., $k_m^* = 0 \text{ km}^{-1}$) has a relatively weak presence in the bedform for $n = 1$.
- Bedform structure of the pFGM for $n = 2$:**
 The bedform (for $n = 2$) has a relatively strong multichromatic structure. The amplitude of this bedform is largest around the centre of the model domain (i.e., $x^* \approx 240 \text{ km}$) and decreases towards both ends of the domain. The DFT spectrum shows that the dominant monochromatic components have similar wavelengths (one peak). Moreover, the spatially uniform component also has a relatively weak presence in the bedform for $n = 2$.

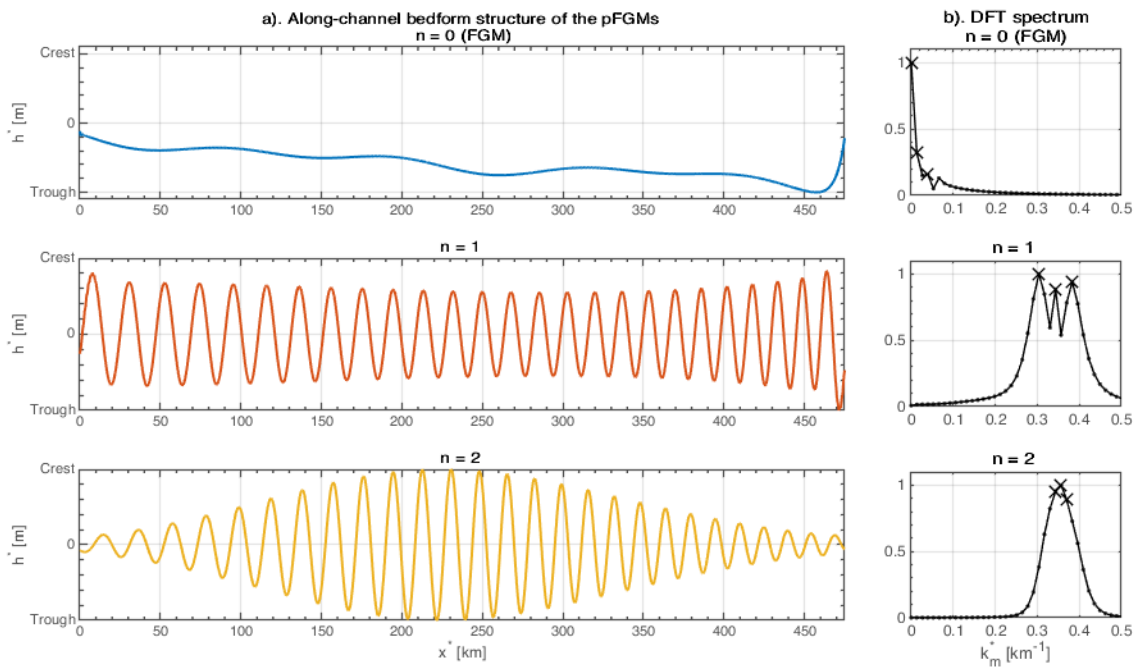


Figure 15: (a) Along-channel bedform structures of the pFGMs for the three lowest cross-channel modes (n); and (b) the corresponding Discrete Fourier Transform (DFT) spectra of the pFGMs. The bedform structures are shown for the NRL model (Figure 3) applied to the reduced friction case in the Western Scheldt (Table 1). X denotes the wavenumbers (k_m^* in km^{-1}) of the three monochromatic sinusoidal components that are most strongly present in the corresponding multichromatic bedform structure.

6. Discussion

In this chapter we first interpret and discuss the results obtained using the NRL model in which a propagating tidal wave is considered (see Figure 3). From these results, statements are derived regarding the influence of a propagating tidal wave on the formation of tidal bars. Finally, we evaluate the NRL model developed and applied in this study.

6.1 Interpretation of the results for the NRL model

6.1.1 Interpretation of the solutions to the basic state when a propagating tidal wave is considered

Aspects of the spatially variant basic state

The spatially variant solutions to the basic state for the NRL model are given in Subsection 3.2.2. First, we discuss two aspects of the solutions to the basic state in Figure 5:

1. Spatially variant solutions for the free water surface and depth-averaged velocity.
2. Bed evolution in the spatially variant basic state.

1. Spatially variant solutions for the free water surface and depth-averaged velocity

The free water surface and depth-averaged velocity are described by sinusoidal waves. As these waves travel in the along-channel direction they become increasingly distorted due to advection. This distortion leads to an increase in amplitude of the wave over the model domain. Conversely, the amplitude of the wave decreases due to friction. In the reduced friction case for the Western Scheldt, the wave amplitude remains relatively constant over the model domain, meaning that the effects caused by advection and friction cancel each other out. Friction is much higher in the standard friction case, therefore resulting in a wave amplitude that decreases over the model domain.

2. Bed evolution in the spatially variant basic state

The bed evolution in the basic state is equal to zero when friction is neglected. Conversely, when friction is included the bed evolution in the basic state decreases in the along-channel direction. The bed evolution is equal to the divergence of the tidally averaged bed transport, which is in turn related to the flow velocity and friction. Figure 16 contains the tidally averaged flow velocity ($\langle u^* \rangle$) as a function of the along-channel distance for three cases in the Western Scheldt (see Table 1): the case without friction (i.e., the standard friction case with $r^* = 0$ m/s), the reduced friction case and the standard friction case. Figure 16a shows that the tidally averaged flow velocity is spatially uniform when friction is neglected. The bed evolution is thus equal to zero. Figure 16b and c show that the tidally averaged flow velocity decreases exponentially over the model domain when friction is included. The absolute bed evolution is therefore strongest at the left side of the model domain (i.e., at $x^* = 0$ km) and decreases in the along-channel direction. This figure also shows why the erosion of the bed is stronger and more localised at the left side of the domain for the standard friction case.

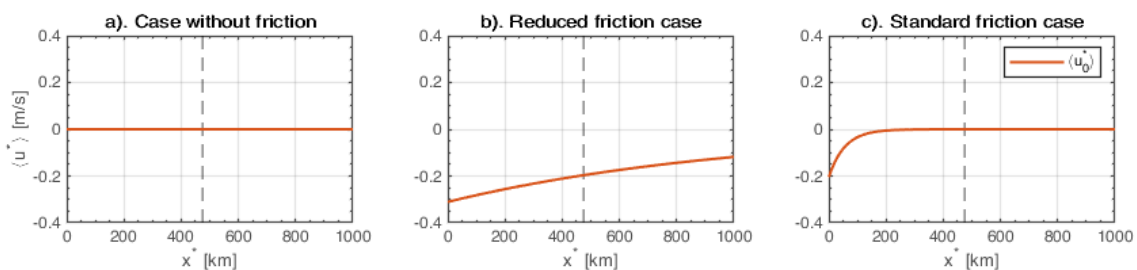


Figure 16: Solution to the basic state: tidally averaged along-channel depth-averaged velocity ($\langle u^* \rangle$ in m/s) as a function of the along-channel distance (x in km). The solution is shown for the NRL model (Figure 3) applied to three cases in the Western Scheldt (Table 1): (a) the case without friction (i.e., the standard friction case with $r^* = 0$ m/s); (b) the reduced friction case; and (c) the standard friction case. The grey dashed line denotes the length of the model domain (i.e., $L_{dom}^* = 475$ km).

Sensitivity of the bed evolution in the spatially variant basic state

The sensitivity of the bed evolution under the basic flow is analysed in Section 3.3. In this analysis the maximum absolute bed evolution (dh^*/dt^*) is plotted against different model parameters (see Figure 6 to Figure 8). The following relations can be derived from these figures:

1. Froude number (Fr), mean water depth (H^*) and free surface elevation amplitude (Z^*):

dh^*/dt^* increases when Fr becomes larger. Therefore, dh^*/dt^* mostly depends on the ratio between H^* and Z^* (i.e., $Fr = \delta = Z^*/H^*$) and to a lesser extent on the absolute values of H^* and Z^* . This is expected since the amplitude of the flow velocity depends on Fr (see the expression in Eq.(14), which can be rewritten to $U^* = \delta\sqrt{g^*H^*}$). Therefore, dh^*/dt^* indirectly depends on Fr, due to the relation between the flow velocity and dh^*/dt^* (see Eq.(12)).

2. Linear friction coefficient (r^*):

dh^*/dt^* is maximised when $r^* \approx 1.5 \cdot 10^{-3}$ m/s. This can be explained by analysing the tidally averaged flow velocity. When the $r^* < 1.5 \cdot 10^{-3}$ m/s this results in a smaller divergence of the tidally averaged flow velocity, thereby also decreasing dh^*/dt^* . When $r^* > 1.5 \cdot 10^{-3}$ m/s this decreases the maximum tidally averaged flow velocity at the left side of the model domain. The divergence over the domain will thus also be smaller, thereby again decreasing dh^*/dt^* .

3. Bed load coefficient (α^*):

dh^*/dt^* increases when α^* becomes larger. This is expected because of the linear relation between α^* and dh^*/dt^* (see Eq.(12)).

The abovementioned relations provide some insight into the sensitivity of the bed evolution in the basic state for the NRL model.

Validity of the solution to the basic state

Finally, we analyse the validity of the solution to the basic state for the NRL model presented in Subsection 3.2.2. This is done by comparing the bed evolution in the basic state with the evolution of the bed in the perturbed state. If the former is small compared to the latter, it is valid to conclude that the bed in the basic state remains relatively flat. This is important because the basic state must represent a steady system with a flow over a flat bed.

The validity of the solution to the basic state for the NRL model is analysed by determining a critical bedform height (h_c), for which the bed evolution in the perturbed state is equal to the bed evolution in the basic state. This critical bedform height is determined according to:

$$h_c^* = \frac{1}{\omega_{m,FGM}^*} \frac{dh_0^*}{dt^*}, \quad (73)$$

where, h_c^* is the critical bedform height; $\omega_{m,FGM}^*$ is the growth rate of the FGM; and dh_0^*/dt^* is the bed evolution in the basic state. When the height of the bedforms is larger than the critical height, the bed evolution in the basic state is smaller than the bed evolution in the perturbed state.

The results in Section 3.3. show that the (maximum absolute) bed evolution in the basic state for the NRL model is approximately 12.3 and 0.1 cm/yr for the standard and reduced friction case in the Western Scheldt, respectively (see † and × in Figure 5 to Figure 8). In this analysis we use the growth rate of the FGM found by applying the RL model to the standard friction case (i.e., $\omega_m^* = 0.15 \text{ yr}^{-1}$). This growth rate is used because it complies with the growth rates for the Western Scheldt found in similar linear stability studies (e.g., Hepkema et al., 2019, 2020). Therefore, the growth rate found by applying the RL model to the standard friction case seems to be more representative for the Western Scheldt than the growth rates found for the reduced friction case. Substituting the abovementioned values in Eq.(73) results in a critical bedform height of $h_c = 82$ cm and 0.7 cm for the standard and reduced friction case in the Western Scheldt, respectively.

A linear stability analysis can only be used to analyse the initial growth of rhythmic bed features (i.e., within the linear regime). Tidal bars typically have heights of several metres (Hepkema et al., 2019). The linear regime for the height of these bed features is therefore expected to be of the order of centimetres. The critical bedform height for the standard friction case (i.e., $h_c = 82$ cm) is thus expected to be far outside the linear regime, while the critical height for the reduced friction case (i.e., $h_c = 0.7$ cm) is likely within the linear regime.

Finally, it should be noted that the bed evolution in the basic state occurs on a larger spatial scale (i.e., tidal wavelength) compared to the smaller spatial scale of the bed evolution in the perturbed state (i.e., morphological wavelength). Because of this, the former leads to the formation of a gradual slope that extends over (a large section of) the model domain, while the latter results in shorter rhythmic bedforms on this slope. This difference between the spatial scales mainly applies to the reduced friction case, since for this case the erosion of the bed in the basic state occurs over the whole model domain, contrary to the more localised bed erosion for the standard friction case (see Figure 5).

From the abovementioned results, we derive that the solution to the basic state for the NRL model presented in this study is only valid for the reduced friction case in the Western Scheldt, since the bed evolution is small and occurs on a relatively large spatial scale. The solution to the basic state for the reduced friction case thus represents a valid basic state, i.e., an approximately steady system with a flow over a relatively flat bed.

6.1.2 Interpretation of the solutions to the perturbed state when a propagating tidal wave is considered

Aspects of the solutions to the perturbed state for the NRL model

The solutions to the perturbed state for the NRL model applied to the reduced friction case are shown in Section 5.2. First, we discuss three aspects regarding the growth curves (see Figure 14) and along-channel bedform structures (see Figure 15):

1. Computational sawtooth patterns.
2. Multichromatic bedform structures that do not satisfy the conservation of sediment.
3. Consistent differences between the growth curves for $n > 0$ for the NRL and RL model.

1. Computational sawtooth patterns

First, we analyse the sawtooth patterns that occur along the (numerical) growth curves for the NRL model. These patterns are caused by the method that is used to construct the growth areas and curves for multichromatic bedforms (see Appendix D). This method uses a Discrete Fourier Transform (DFT) spectrum to assign the growth rate for a particular bedform structure to the three most dominant sinusoidal components that are present in this structure. When these three components have wavenumbers that lie within a narrow spectrum, this results in a smooth growth area, and hence a smooth growth curve (e.g., see the growth curve around the pFGM for $n = 2$ for the NRL model in Figure 14 and the corresponding DFT spectrum in Figure 15). Conversely, the three most dominant components can also have wavenumbers that vary over a wider range (e.g., see the DFT spectrum for $n = 1$ in Figure 15). The other wavenumbers within this range might have different growth rates, since the growth rate for a particular bedform structure is only assigned to the three most dominant components, and not to the whole range of wavenumbers between these components. When adjacent wavenumbers have different growth rates, this results in a jagged edge for the growth area, and hence a sawtooth pattern for the growth curve. The computational sawtooth patterns are thus caused by the method used to construct the growth areas and curves for multichromatic bedforms.

2. Multichromatic bedform structures that do not satisfy the conservation of sediment

First, we analyse the multichromatic bedform structures for $n = 0$. Most bedforms for $n = 0$ have a dominant (or relatively strong) sinusoidal component with a wavenumber of $k_m^* = 0 \text{ km}^{-1}$ (e.g., see the DFT spectrum for $n = 0$ in Figure 15). This component is spatially uniform, because it has an infinitely long wavelength (i.e., $L_m^* = \infty \text{ km}$). If this spatially uniform component has a non-zero growth rate, this implies sedimentation or erosion along the whole bed. To satisfy the conservation of sediment in the system, this component must therefore have a growth rate of zero, meaning that the bed perturbation will not grow or decay over time. Since most multichromatic bedforms for $n = 0$ have a dominant (or relatively strong) spatially uniform component, these bedforms must all have growth rates equal to zero. However, the growth curve for $n = 0$ shows that these bedforms have non-zero growth rates (see Figure 14). The bedforms for $n = 0$ therefore do not comply with the requirement for conservation of sediment.

The contradiction described above might be the reason for the unexpected shape of the growth curve for $n = 0$ around small wavenumbers (see Figure 14). This growth curve for the NRL model approaches a slightly positive growth rate, instead of the origin, as the wavenumber decreases to zero. This does not comply with the growth curve for the RL model (see Figure 14) and the results found by similar linear stability studies (e.g., Schramkowski et al., 2002). The shape of this growth curve for the NRL model is therefore assumed to be invalid (mainly around small wavenumbers). We expect that the growth curve for $n = 0$ should approach the origin, as the wavenumber decreases to zero, similar to the shape of the growth curve for the RL model.

Next, we analyse the multichromatic bedforms for higher cross-channel modes (i.e., $n > 0$). The DFT spectra show that the spatially uniform component has a relatively weak presence in most bedforms for $n > 0$, (e.g., see DFT spectrum for $n = 1$ and 2 in Figure 18). Therefore, the bedforms for $n > 0$ seem to better comply with the requirement for conservation of sediment in the system. The growth curves for $n > 0$ are therefore assumed to be valid.

The model equations and periodic boundary conditions used in the model formulation of the NRL model set the requirement for conservation of sediment. However, the abovementioned results for the NRL model do not seem to comply with this requirement. Possible causes for this contradiction between the model formulation and the results are given in Subsection 6.2.6.

3. Consistent differences between the growth curves for $n > 0$ for the NRL and RL model

Several differences are noted when comparing the growth curves for the NRL model to those for the RL model (see Figure 14). Three of these differences are consistent for the higher cross-channel modes (i.e., $n > 0$): (1) the growth curves for the NRL and RL model have similar growth rates for small wavenumbers (i.e., $k_m^* \approx 0 \text{ km}^{-1}$); (2) the peaks of the growth curves for the NRL model are higher and occur at larger wavenumbers compared to the peaks for the RL model; and (3) the growth curves for the NRL model have steeper slopes for larger wavenumbers (i.e., $k_m^* > 0.5 \text{ km}^{-1}$) than the curves for the RL model. The consistency of these differences suggests that they may be caused by a propagating tidal wave. Moreover, since the results for $n > 0$ seem to comply relatively well with the requirement for conservation of sediment (as explained above), it is less likely that these differences are related to (numerical) inaccuracies in the NRL model.

Assuming that the growth curve for $n = 0$ for the NRL model should approach the origin (as explained above), the FGM for the reduced friction case has a growth rate of zero (i.e., $\omega_m^* = 0 \text{ yr}^{-1}$). This means that all other modes have negative growth rates. Therefore, the basic state is stable, meaning the system evolves back to the basic state (i.e., a flat bed). Based on the growth curves for the NRL model (see Figure 14), the formation of tidal bars is thus not expected for the reduced friction case in the Western Scheldt. Hence, it is not possible to use these results to draw direct conclusions regarding the influence of a propagating tidal wave on the formation of tidal bars.

The NRL model developed in this study cannot be used to obtain solutions to the perturbed state for the standard friction case. However, based on the growth curves for the RL model (see Figure 10), the formation of tidal bars is expected for the standard friction case. We assume that the general (or qualitative) influence of a propagating tidal wave on the growth curves is similar for both cases in the Western Scheldt. By making this assumption it is possible to get a first impression regarding the influence of a propagating tidal wave on the formation of tidal bars (see Subsection 6.1.3). This assumption is based on the observation that the general (or qualitative) aspects of the solutions to the basic state (as listed in Subsection 6.1.1) are consistent for both cases in the Western Scheldt. Nevertheless, the exact (or quantitative) details of these solutions do differ. Further research must therefore be conducted to ensure the validity of the abovementioned assumption.

Replicating the growth curves for the NRL model

Finally, we will show that the growth curves for the NRL model (see Figure 14) can be replicated using the (semi-analytical) RL model with increased values for two coefficients: the linear friction coefficient (r^*) and the bed slope correction coefficient in the along-channel direction (λ_a^*). Note that the original (semi-analytical) RL model only has one bed slope correction coefficient (λ^*). In this analysis, this coefficient is split into a cross-channel coefficient (λ_c^*) and an along-channel coefficients (λ_a^*). The cross-channel bed slope correction coefficient (λ_c^*) is not increased. These changes to the coefficients of the RL model are based on the findings for the study by Scharmowski et al. (2002), in which the effects of the geometry and bed friction on local bedforms are analysed. The exact values for the two coefficients are determined by fitting the growth curve for $n = 1$ for the RL model with altered coefficients (r^* and λ_a^*) to the growth curve for $n = 1$ for the NRL model.

Figure 17 contains the growth curves (and areas) for the NRL model and the RL model with altered coefficients (r^* and λ_a^*). The solid lines and dashed lines (with shaded areas) represent the growth curves for the RL model with altered coefficients (r^* and λ_a^*) and the growth curves (with growth areas) for the (numerical) NRL model, respectively. \bullet and \times denote the FGM for the RL and NRL model, respectively. Moreover, \bullet denotes the partial fastest growing mode (pFGM) for each cross-channel mode. Recall that the pFGMs are the FGM for each individual cross-channel mode.

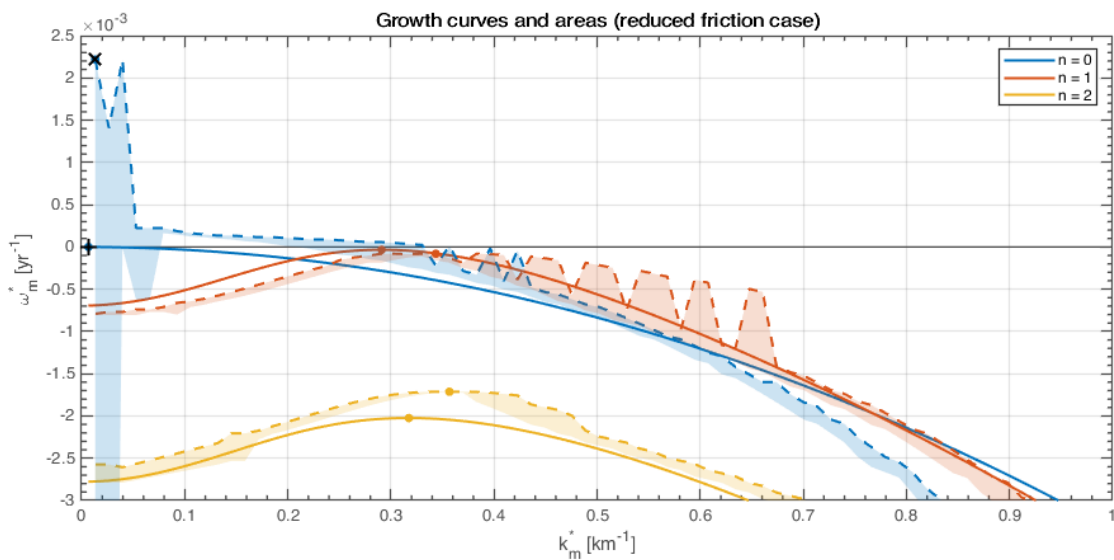


Figure 17: Growth curves (and areas) showing the growth rate (ω_m^* in yr^{-1}) as a function of the morphological wavenumber (k_m^* in km^{-1}) for different cross-channel modes (n). The growth curves (and areas) are shown for the reduced friction case in the Western Scheldt (Table 1). The solid lines and dashed lines (with shaded areas) represent the growth curves for the (semi-analytical) RL model with altered model coefficients (r^* and λ_a^*) and the growth curves (with growth areas) for the (numerical) NRL model, respectively. \bullet , \times and \times denote the pFGM for each cross-channel mode, the FGM for the RL model and the FGM for the NRL model, respectively.

Figure 17 shows that the growth curves for the NRL model can be replicated by altering two coefficients (r^* and λ_a^*) of the RL model. This however does not directly imply that the free surface effects caused by a propagating tidal wave increase the effects caused by friction (r^*) and the bed slope in the cross-channel direction (λ_a^*). It is entirely possible that a propagating tidal wave induces other effects, such as free surface effects, that result in the differences between the growth curves for the NRL and RL model observed in Figure 14.

6.1.3 Influence of a propagating tidal wave on the formation of tidal bars

The growth curves for the reduced friction case in the Western Scheldt are shown in Figure 14. This figure shows that the peaks of the growth curves (for $n > 0$) for the NRL model are higher and occur at larger wavenumbers compared to the peaks for the RL model. These results cannot be used to draw direct conclusions about the relation between a propagating tidal wave and the formation of tidal bars. However, by making two assumptions, these results can be used to get a first impression regarding the influence of a propagating tidal wave on the formation of tidal bars (see Subsection 6.1.2).

In Subsection 6.1.2 we argue that the abovementioned difference between the growth curves might be caused by a propagating tidal wave. Moreover, we also propose that the general (or qualitative) influence of a propagating tidal wave on the formation of tidal bars may be the same for both cases in the Western Scheldt. Assuming that these two preconditions are true, we expect that a propagating tidal wave might have the following influence on the formation of tidal bars:

- **Formation of shorter tidal bars (i.e., the wavelength of the FGM decreases):**
A propagating tidal wave increases the wavenumber of the FGM. Hence, the wavelength of the dominant bedform decreases. Assuming the FGM has a positive growth rate, this results in the formation of shorter tidal bars.
- **Faster formation of tidal bars (i.e., the growth rate of the FGM increases):**
A propagating tidal wave also increases the growth rate of the FGM. Assuming that the growth rate of the FGM is positive, this implies faster formation of tidal bars. Here, we also assume that the growth rate of the FGM gives an indication of the speed at which tidal bars develop.

The abovementioned statements are based on the results obtained using the NRL model developed and applied in this study. To ensure the validity of these statements, further research must therefore be conducted in which this model is improved and validated. The NRL model presented in this study can be improved by addressing the points discussed in Section 6.2. Moreover, the abovementioned statements are based on the results for the reduced friction case in the Western Scheldt. The NRL model should thus also be applied to a wider range of cases, including the standard friction case presented in this study.

6.2 Evaluation of the NRL model

6.2.1 Model formulation

Linear stability models are generally simple due to their idealised nature. However, the model formulation used in this study (see Chapter 2) is especially simple compared to other linear stability models that are used to analyse the formation of tidal bars (e.g., Hepkema et al., 2019, 2020). Similar models generally capture additional physical processes of the system, such as the Coriolis effect and suspended sediment transport. Moreover, the linear stability model used in this study only considers a flow induced by a M_2 tide. The current model can therefore not be used, but can be extended, to study asymmetrical flow conditions caused by a residual current (M_0) and higher order tidal components (M_4 and M_8).

6.2.2 Expansions in the Froude number

An expansion in the Froude number is used to find the solution for the basic flow under a propagating tidal wave (see Subsection 3.2.2). The solution presented in this study is of first order in Froude number (δ^1). This solution is therefore only valid up to an along-channel distance of $\delta x \ll 1$. When friction is neglected, the amplitude of the wave keeps increasing as it becomes more distorted. This is physically unrealistic since this behaviour is in reality counterbalanced by dispersion. Including higher order terms in Froude number will result in a slightly more accurate solution for the basic flow and increase the along-channel distance for which this solution is valid. Alternatively, a multiple-scale expansion can be used to obtain a solution which consists of two (or more) components that occur on different scales (Holmes, 2013). For example, an oscillatory component that describes the solution on a small spatial scale, and another component that describes the variations that take place on a large spatial scale. Using a multiple-scale expansion might therefore result in a more accurate solution to the basic state.

The friction terms in the momentum equations of the perturbed state are also linearised using a geometric series in the Froude number (see Subsection 5.1.1). In this study this linearisation is also an approximation of first order in Froude number (δ^1). Including higher order terms will also increase the accuracy of the linearised friction terms.

Ideally, all expansions in the Froude number used throughout the NRL model should be approximations of second order (or higher) in Froude number. This is because, the Froude number ($Fr = \delta = Z^*/H^*$) is of the same order as the ratio $\varepsilon = \hat{h}^*/H^*$ used to linearise the system (see Eq.(2)). Expansions of second order in Froude number will therefore ensure that the accuracy of the analysis is not limited by the accuracy of the expansions in the Froude number (i.e., $\mathcal{O}(\delta^3)$), but by the accuracy of the linearisation of the system (i.e., $\mathcal{O}(\varepsilon^2)$).

6.2.3 Truncation and discretisation

The hydrodynamic variables in the perturbed state are expanded as Fourier series (see Subsection 4.3.2). In this study these Fourier series are truncated at $P = 2$. Increasing the value of P will allow for the inclusion of additional higher harmonics that are generated by the advection terms in the model equations. This can result in a more accurate solution to the perturbed state. Moreover, a central difference scheme is used to discretise the model domain. Increasing the number of discretisation points (M) results in a numerical solution that is a better approximation of the semi-analytical solutions (see Subsection 4.4). In this study, $M = 801$ seems to result in sufficiently accurate numerical solutions for both cases in the Western Scheldt. Nevertheless, a larger (or smaller) number of discretisation points might be required when applying the numerical model to other cases.

6.2.4 Periodic boundary conditions

In this study, the discretisation uses periodic boundary conditions at either side of the model domain (i.e., at $x^* = 0$ and 475 km). Due to these boundary conditions, the (numerical) NRL model can currently only be applied to the reduced friction case (see Subsection 5.1.2). It is beneficial to use non-periodic boundary conditions in the discretisation, since this allows us to apply the NRL model to a

wider range of cases, including the standard friction case for the Western Scheldt. However, the use of non-periodic boundary conditions (e.g., Neumann and/or Dirichlet) is outside the main scope of this study. This is because further research must be conducted to correctly implement these boundary conditions. Nevertheless, Appendix E does contain the solutions to the perturbed state obtained using the NRL model with three different sets of non-periodic boundary conditions.

6.2.5 Numerical solution procedure for the cross-channel bedform structures

The (numerical) NRL model presented in this study uses an analytical procedure to obtain the solutions for the bedforms in the cross-channel direction. This analytical procedure is comparable to the procedure used (in the along-channel direction) by the (semi-analytical) RL model. Part of this procedure is to predefine the sinusoidal structure of the bedforms in the cross-channel direction. Therefore, the cross-channel structure cannot respond to spatially variant flows caused by a propagating tidal wave. To allow for such a response, the current analytical procedure must be replaced by a numerical procedure. This procedure is comparable to the numerical procedure used (in the along-channel direction) by the NRL model presented in this study. When implemented, the NRL model will be fully numerical, meaning that numerical solution procedures for the perturbed state are used in both horizontal directions. This will most likely not enhance the results for tidal bars in a tidal channel due to the unidirectional nature of the propagating tidal wave. However, a completely numerical solution procedure is required to analyse the influence of a propagating tidal wave on the formation of other tide-induced rhythmic bed features (see Subsection 7.6.1).

6.2.6 Contradictions in model formulations and results

In this study, a standard and reduced friction case are analysed for the Western Scheldt (see Table 1). For the standard friction case, the solutions to the perturbed state comply with the solutions for the Western Scheldt found in similar linear stability studies (e.g., Hepkema et al., 2019, 2020). This implies that the linear friction coefficient (r^*) and bed load coefficient (α^*) used in the standard friction case seem to be appropriate for the Western Scheldt. However, the solutions to the basic state show that the standard friction case results in a propagating tidal wave that decays unrealistically fast (i.e., complete decay after roughly one tidal wavelength). Based on these solutions, the coefficients used in the reduced friction case seem to be more appropriate, since the propagating tidal wave decays much slower (i.e., complete decay after multiple tidal wavelengths). However, the solutions to the perturbed state for the reduced friction case underestimate the solutions found in similar linear stability studies. Further research must therefore be conducted regarding the values of the linear friction coefficient (r^*) and bed load coefficient (α^*) used in the NRL model.

The model equations and periodic boundary conditions used in the model formulation of the NRL model set the requirement for conservation of sediment. However, the results for the NRL model do not seem to comply with this requirement (see Subsection 6.1.2). This contradiction may be related to one or more of the following aspects of the NRL model: slightly incorrect use of periodic boundary conditions, since the solutions to basic state at the left of the model domain does not completely match the solution at the right side of the domain; the bed evolution in the basic state (see Figure 5) does not comply with the requirement for conservation of sediment in the system; and other (numerical) inaccuracies that might have occurred in the NRL model. Further research must be conducted to find the exact cause for this contradiction between the model formulation and the model results.

6.2.7 Conceptual and computational complexity

It should be noted that the (numerical) NRL model presented in this study is conceptually complex compared to the (semi-analytical) RL model. This is because of the expansion in the Froude number required to find the solution to the basic state and the numerical procedure required to obtain the solution to the perturbed state. Due to the latter, the (numerical) NRL model is also computationally more expensive than the (semi-analytical) RL model. This makes the NRL model less suitable for an extensive sensitivity analysis.

7. Conclusion and Outlook

The objective of this master thesis and the research questions are formulated in Section 1.4. This chapter contains answers to these research questions and provides an outlook for further research regarding the influence of a propagating tidal wave on the formation of rhythmic bed features.

7.1 How can a propagating tidal wave be considered in a linear stability model for tidal bars?

In Chapter 2, a model is formulated for a propagating tidal wave in a tidal channel. This model consists of the depth-averaged hydrodynamic equations, a simple sediment transport formula and a sediment conservation equation for the bed evolution. Boundary conditions at the open boundaries of the channel demand that both the free water surface and along-channel flow velocity must follow sinusoidal waves that can only propagate in the positive along-channel direction. Due to these boundary conditions, the NRL model can consider a tidal wave that propagates through the channel.

7.2 How can we define a meaningful basic state for this NRL model?

In Chapter 3, an expansion in the Froude number is used to obtain the solution to the basic state for the NRL model. The results show that the free water surface and depth-averaged velocity in the along-channel direction are described by sinusoidal waves that become increasingly distorted as they travel in the along-channel direction. Moreover, because the basic flow is spatially variant, the sensitivity of the bed evolution under the basic flow is analysed. This is done by comparing the bed evolution in the basic state to the approximated evolution of the bed in the perturbed state. If the former is small compared to the latter, it is valid to conclude that the bed in the basic state remains relatively flat. This is important because the basic state must represent a steady system with a flow over a flat bed. The results show that the solution to the basic state for the NRL model presented in this study is only valid for the reduced friction case in the Western Scheldt.

7.3 How can we obtain the solution to the perturbed state for this NRL model?

In Chapter 4, a numerical solution procedure for the perturbed state is developed. This is done because the semi-analytical procedure breaks down when the solution to the basic state is spatially variant, as is the case for the NRL model. As part of the numerical procedure, a generalised eigenvalue problem for the evolution of this state is defined. The eigenvectors and eigenvalues that follow from this problem describe the structure of the bedforms and can be used to determine the other bedform characteristics (i.e., growth rate, cross-channel mode and wavelength). These characteristics are used to construct growth curves and to define the fastest growing mode (FGM). The FGM is considered the dominant bedform and therefore provides insight into the behaviour of the system. The numerical procedure developed in this study is first applied to the (numerical) RL model. This is done to validate the numerical procedure by comparing the numerical solutions to those obtained using the semi-analytical solution procedure. The results show that the numerical and semi-analytical solutions are approximately equal when the total number of discretisation points is sufficiently large.

7.4 What are the growth characteristics for this NRL model?

In Chapter 5, the numerical solution procedure for the perturbed state is applied to the NRL model in which a propagating tidal wave is considered. The (numerical) NRL model can only be applied to the reduced friction case, due to the periodic boundary conditions used in the discretisation. Therefore, the results for the NRL model can only be used to derive growth characteristics for the reduced friction case in the Western Scheldt. However, by using the results for the RL model and making two assumptions (summarised in Section 7.5), it is possible to get a first impression of the growth characteristics for the standard friction case. The growth characteristics of the FGM for both cases in the Western Scheldt are given in Table 3. Based on these characteristics, tidal bars are only expected to develop for the standard friction case.

Table 3: Growth characteristics of the FGM for the standard and reduced friction cases in the Western Scheldt.

Growth characteristic	Symbol	Unit	Value of the FGM	
			Reduced friction case ¹	Standard friction case ²
Growth rate	ω_m^*	yr ⁻¹	0	> 0.15
Cross-channel mode	n	–	0	2
Wavenumber	k_m^*	km ⁻¹	0	> 0.59
Wavelength	L_m^*	km	–	< 10.7

¹The values of the FGM for the reduced friction case are based on the growth curves for the NRL model (see Figure 14). Note that the shape of the growth curve for $n = 0$ is assumed to be invalid (mainly around small wavenumbers). ²The values of the FGM for the standard friction case are based on the growth curves for the RL model (see Figure 10). The relative increase (>) or decrease (<) of these values is based on the differences between the growth curves for the reduced friction case for the NRL and RL model (see Figure 14).

7.5 What is the influence of a propagating tidal wave on the formation of tidal bars?

In Chapter 6, the results obtained using the NRL model are discussed and interpreted. These results show that the peaks of the growth curves (for $n > 0$) for the NRL model are higher and occur at larger wavenumbers compared to the peaks for the RL model. We define two preconditions: this difference between the growth curves is caused by a propagating tidal wave; and the general (or qualitative) influence of a propagating tidal wave is the same for both cases in the Western Scheldt. Assuming these preconditions are true, we expect that a propagating tidal wave might have the following influence on the formation of tidal bars:

- Formation of shorter tidal bars (i.e., the wavelength of the FGM decreases).
- Faster formation of tidal bars (i.e., the growth rate of the FGM increases).

These statements are based on the results obtained using the NRL model developed and applied in this study. To ensure the validity of these statements, further research must therefore be conducted in which this model is improved and validated.

7.6 Outlook for further research regarding the influence of a propagating tidal wave on the formation of rhythmic bed features

Further research can be performed regarding the NRL model that is developed and applied in this study. Firstly, the NRL model can be improved by addressing the points discussed in Section 6.2. Secondly, the NRL model may be used to analyse the formation of other tide-induced rhythmic bed features under a propagating tidal wave, such as sand banks and sand waves. We briefly comment on the points that must be considered before the NRL model can be used to analyse these bedforms. Finally, we also discuss how the NRL model might provide further insight into the $k = 0$ -problem.

7.6.1 Sand banks and sand waves

Sand banks are large offshore rhythmic bed features with typical wavelengths of tens of kilometres, widths of 5 to 10 km and heights of tens of metres. Their crests are usually oriented at a slight angle (ranging from 0° to 30°) with respect to the mean tidal current (Hulscher & van den Brink, 2001). This is due to tidal rectification, which describes the adjustment of the tidal flow obliquely approaching a sand bank (Pattiaratchi & Collins, 1987; Robinson, 1983; Roos & Hulscher, 2003; Zimmerman, 1982). Because of their orientation, sandbanks are generally modelled using 2DH models (e.g., Hulscher et al., 1993). To capture the mechanism of tidal rectification, the Coriolis effect must be added to the NRL model. Due to the orientation of the sand banks, a propagating tidal wave influences the structures of the bedforms in both horizontal directions. The NRL model must therefore be fully numerical, meaning that numerical solution procedures for the perturbed state are used in both horizontal directions. A more detailed description of a fully numerical NRL model is given in Subsection 6.2.5.

Sand waves are rhythmic bed features with typical wavelengths of 100 to 800 m, heights of the order of several metres and their crests are oriented perpendicular to the mean tidal current (Hulscher & van den Brink, 2001). Sand waves are formed due to residual circulations in the vertical plane (Zimmerman, 1982). To capture these circulations, sand waves are generally modelled using 2DV (or 3D) models (e.g., Hulscher, 1996). The NRL model must thus be changed to a 2DV (or 3D) model. In sand wave models, the rigid lid assumption is generally used to simplify the boundary conditions at the free surface. This assumption cannot be used in the NRL model, since this neglects the free surface effects caused by a propagating tidal wave. Because of this, the solution to the basic state obtained by the NRL model will vary in both the horizontal and vertical direction. The NRL model must therefore also be fully numerical when it is used to model sand waves.

The abovementioned changes must be made to the NRL model before this model can be used to analyse the formation of sand banks and sand waves. Before all this, the NRL model must first be improved by addressing the points discussed in Section 6.2.

7.6.2 $k = 0$ -problem

Field observations have shown that bedforms have a limited range in wavelengths (van Santen et al., 2011). The formation of bedforms with short wavelengths is known to be suppressed by slope-induced sediment transport. It is however still unknown which physical mechanisms suppresses the formation of bedforms with long wavelengths (Borsje et al., 2014; Campmans, 2018). When modelling bed evolution on large spatial domains, the system therefore tends to gradually develop bedforms with positive growth rates and wavelengths equal to the size of the domain length (van den Berg et al., 2012). Because of this, the problem is sometimes referred to as the $k = 0$ -problem (Roos, 2019). This fundamental problem occurs in both linear stability models and nonlinear models for different morphodynamic systems, e.g., sand banks (e.g., Roos & Hulscher, 2007), sand waves (e.g., Campmans et al., 2018) and river dunes (e.g., Paarlberg et al., 2009). This implies that the physical mechanism that suppresses the formation of long bedforms is still missing. In nonlinear models, this mechanism might be found by modelling turbulence using a $k - \varepsilon$ model in combination with including suspended load transport (Borsje et al., 2014), or by including a bedform splitting mechanisms that artificially introduces small bedforms (Warmink et al., 2014).

The missing mechanism that suppresses the formation of long bedforms could also be related to the horizontal variations in a tidal wave over a large spatial domain (Campmans, 2018). Currently, most linear stability models apply the rigid lid assumption, through which these variations are neglected. This assumption may therefore be the underlying cause of the $k = 0$ -problem. The rigid lid assumption is not applied in the NRL model presented in this study. This model might thus be able to provide further insight into one of the mechanisms that suppresses the formation of long bedforms.

The $k = 0$ -problem does not occur when modelling tidal bars in a tidal channel with a traditional linear stability model (e.g., the RL model used in this study). This is because, the formation of infinitely long tidal bars is already suppressed by the effects related to the finite width of the tidal channel. Therefore, the results for the NRL model obtained in this study do not directly provide further insight regarding the possible relation between the rigid lid assumption and the $k = 0$ -problem. If the NRL model can be altered to analyse the formation of other tide-induced rhythmic bed features (see Subsection 7.6.1), then this model might be able to provide further insight into the missing mechanism that suppresses the formation of long bedforms.

References

- Borsje, B. W., Kranenburg, W. M., Roos, P. C., Matthieu, J., & Hulscher, S. J. M. H. (2014). The role of suspended load transport in the occurrence of tidal sand waves. *Journal of Geophysical Research: Earth Surface*, *119*(4), 701–716. <https://doi.org/10.1002/2013JF002828>
- Campmans, G. H. P. (2018). *Modeling storm effects on sand wave dynamics* [University of Twente]. <https://doi.org/10.3990/1.9789036546003>
- Campmans, G. H. P., Roos, P. C., de Vriend, H. J., & Hulscher, S. J. M. H. (2017). Modeling the influence of storms on sand wave formation: A linear stability approach. *Continental Shelf Research*, *137*, 103–116. <https://doi.org/10.1016/j.csr.2017.02.002>
- Campmans, G. H. P., Roos, P. C., Vriend, H. J., & Hulscher, S. J. M. H. (2018). The Influence of Storms on Sand Wave Evolution: A Nonlinear Idealized Modeling Approach. *Journal of Geophysical Research: Earth Surface*, *123*(9), 2070–2086. <https://doi.org/10.1029/2018JF004616>
- Dalrymple, R. W., & Rhodes, R. N. (1995). *Estuarine dunes and bars*. In: *Geomorphology and Sedimentology of Estuaries, Development in Sedimentology* (G. M. E. Perillo (ed.); 53rd ed.). Elsevier. <https://www.elsevier.com/books/geomorphology-and-sedimentology-of-estuaries/perillo/978-0-444-88170-0>
- Dodd, N., Falqués, A., Hulscher, S. J. M. H., Rózyński, G., Vittori, G., Blondeaux, P., Calvete, D., & De Swart, H. E. (2003). Understanding Coastal Morphodynamics Using Stability Methods. *Journal of Coastal Research*, *19*(4), 849–865.
- Exner, F. M. (1920). Zur physik der dünen. *Akad. Wiss. Wien Math. Naturwiss. Klasse*, *129*(2a), 929–952.
- Exner, F. M. (1925). Über die wechselwirkung zwischen wasser und geschiebe in flüssen. *Akad. Wiss. Wien Math. Naturwiss. Klasse*, *134*(2a), 165–204.
- Fox, R. W., McDonald, A. T., Pritchard, P. J., & Mitchell, H. W. (2015). *Fluid Mechanics* (9th SI). John Wiley & Sons.
- Hepkema, T. M., de Swart, H. E., Nnafie, A., Schramkowski, G. P., & Schuttelaars, H. M. (2020). Oblique sand ridges in confined tidal channels due to Coriolis and frictional torques. *Ocean Dynamics*, *70*(12), 1505–1513. <https://doi.org/10.1007/s10236-020-01413-0>
- Hepkema, T. M., de Swart, H. E., & Schuttelaars, H. M. (2019). Sensitivity of Tidal Bar Wavelength to Channel Width. *Journal of Geophysical Research: Earth Surface*, *124*(10), 2417–2436. <https://doi.org/10.1029/2019JF005032>
- Holmes, M. H. (2013). *Introduction to Perturbation Methods* (Vol. 20). Springer New York. <https://doi.org/10.1007/978-1-4614-5477-9>
- Hulscher, S. J. M. H. (1996). Tidal-induced large-scale regular bed form patterns in a three-dimensional shallow water model. *Journal of Geophysical Research: Oceans*, *101*(C9), 20727–20744. <https://doi.org/10.1029/96JC01662>
- Hulscher, S. J. M. H., de Swart, H. E., & de Vriend, H. J. (1993). The generation of offshore tidal sand banks and sand waves. *Continental Shelf Research*, *13*(11), 1183–1204. [https://doi.org/10.1016/0278-4343\(93\)90048-3](https://doi.org/10.1016/0278-4343(93)90048-3)
- Hulscher, S. J. M. H., & van den Brink, G. M. (2001). Comparison between predicted and observed sand waves and sand banks in the North Sea. *Journal of Geophysical Research: Oceans*, *106*(C5), 9327–9338. <https://doi.org/10.1029/2001JC900003>
- Huthnance, J. M. (1982a). On one mechanism forming linear sand banks. *Estuarine, Coastal and Shelf Science*, *14*(1), 79–99. [https://doi.org/10.1016/S0302-3524\(82\)80068-6](https://doi.org/10.1016/S0302-3524(82)80068-6)
- Huthnance, J. M. (1982b). On the formation of sand banks of finite extent. *Estuarine, Coastal and Shelf Science*, *15*(3), 277–299. [https://doi.org/10.1016/0272-7714\(82\)90064-6](https://doi.org/10.1016/0272-7714(82)90064-6)
- Lange, D., Müller, H., Piechota, F., & Schubert, R. (2008). The Weser estuary. *Küste*, *74*, 275–287.
- Leuven, J. R. F. W., Kleinhans, M. G., Weisscher, S. A. H., & van der Vegt, M. (2016). Tidal sand bar dimensions and shapes in estuaries. *Earth-Science Reviews*, *161*, 204–223. <https://doi.org/10.1016/j.earscirev.2016.08.004>
- Naqshband, S., Ribberink, J. S., & Hulscher, S. J. M. H. (2014). Using Both Free Surface Effect and

- Sediment Transport Mode Parameters in Defining the Morphology of River Dunes and Their Evolution to Upper Stage Plane Beds. *Journal of Hydraulic Engineering*, 140(6), 06014010. [https://doi.org/10.1061/\(ASCE\)HY.1943-7900.0000873](https://doi.org/10.1061/(ASCE)HY.1943-7900.0000873)
- Paarlberg, A. J., Dohmen-Janssen, C. M., Hulscher, S. J. M. H., & Termes, P. (2009). Modeling river dune evolution using a parameterization of flow separation. *Journal of Geophysical Research*, 114(F1), F01014. <https://doi.org/10.1029/2007JF000910>
- Pattiaratchi, C., & Collins, M. (1987). Mechanisms for linear sandbank formation and maintenance in relation to dynamical oceanographic observations. *Progress in Oceanography*, 19(2), 117–176. [https://doi.org/10.1016/0079-6611\(87\)90006-1](https://doi.org/10.1016/0079-6611(87)90006-1)
- Phillips, O. M. (1977). *The dynamics of the upper ocean* (2nd ed.). Cambridge University Press.
- Robinson, I. S. (1983). *Chapter 7 Tidally Induced Residual Flows* (pp. 321–356). [https://doi.org/10.1016/S0422-9894\(08\)70505-1](https://doi.org/10.1016/S0422-9894(08)70505-1)
- Roos, P. C. (2019). On the crest of sandwave modelling: Achievements from the past, directions for the future. *Marine and River Dune Dynamics, MARID VI*, 197–202. <https://www.marum.de/Binaries/Binary18538/MARIDVI-Roos-Pieter-KEYNOTE.pdf>
- Roos, P. C., & Hulscher, S. J. M. H. (2003). Large-scale seabed dynamics in offshore morphology: Modeling human intervention. *Reviews of Geophysics*, 41(2). <https://doi.org/10.1029/2002RG000120>
- Roos, P. C., & Hulscher, S. J. M. H. (2007). Nonlinear modeling of tidal sandbanks: Wavelength evolution and sand extraction. *Coastal Engineering 2006*, 2761–2771. https://doi.org/10.1142/9789812709554_0233
- Schramkowski, G. P., Schuttelaars, H. M., & de Swart, H. E. (2002). The effect of geometry and bottom friction on local bed forms in a tidal embayment. *Continental Shelf Research*, 22(11–13), 1821–1833. [https://doi.org/10.1016/S0278-4343\(02\)00040-7](https://doi.org/10.1016/S0278-4343(02)00040-7)
- Seminara, G., & Tubino, M. (2001). Sand bars in tidal channels. Part 1. Free bars. *Journal of Fluid Mechanics*, 440, 49–74. <https://doi.org/10.1017/S0022112001004748>
- Soulsby, R. L. (1997). *Dynamics of marine sands*. Thomas Telford.
- Tambroni, N., Bolla Pittaluga, M., & Seminara, G. (2005). Laboratory observations of the morphodynamic evolution of tidal channels and tidal inlets. *Journal of Geophysical Research: Earth Surface*, 110(4). <https://doi.org/10.1029/2004JF000243>
- van den Berg, J., Sterlini, F., Hulscher, S. J. M. H., & van Damme, R. (2012). Non-linear process based modelling of offshore sand waves. *Continental Shelf Research*, 37, 26–35. <https://doi.org/10.1016/j.csr.2012.01.012>
- van Santen, R. B., de Swart, H. E., & van Dijk, T. A. G. P. (2011). Sensitivity of tidal sand wavelength to environmental parameters: A combined data analysis and modelling approach. *Continental Shelf Research*, 31(9), 966–978. <https://doi.org/10.1016/j.csr.2011.03.003>
- Warmink, J. J., Dohmen-Janssen, C. M., Lansink, J., Naqshband, S., van Duin, O. J. M., Paarlberg, A. J., Termes, P., & Hulscher, S. J. M. H. (2014). Understanding river dune splitting through flume experiments and analysis of a dune evolution model. *Earth Surface Processes and Landforms*, 39(9), 1208–1220. <https://doi.org/10.1002/esp.3529>
- Zimmerman, J. T. F. (1982). On the Lorentz linearization of a quadratically damped forced oscillator. *Physics Letters A*, 89(3), 123–124. [https://doi.org/10.1016/0375-9601\(82\)90871-4](https://doi.org/10.1016/0375-9601(82)90871-4)

Appendices

Appendix A: Rewritten model equations for the perturbed state

A.1 Rewritten model equations for the perturbed state of the RL model

The model equations for the perturbed state of the RL model (see Eq.(50) to Eq.(52) and Eq.(54) in Chapter 4) are linearised by substituting the expressions given in Eq.(55) in these equations. This results in:

$$\frac{\partial \hat{u}_1}{\partial x} - u_0 \frac{\partial \hat{h}_1}{\partial x} + \frac{n\pi}{B} \hat{v}_1 = 0, \quad (\text{A.1})$$

$$\frac{\partial \hat{u}_1}{\partial t} + u_0 \frac{\partial \hat{u}_1}{\partial x} + \frac{\partial \hat{\zeta}_1}{\partial x} + r\hat{u}_1 + ru_0 \hat{h}_1 = 0, \quad (\text{A.2})$$

$$\frac{\partial \hat{v}_1}{\partial t} + u_0 \frac{\partial \hat{v}_1}{\partial x} - \frac{n\pi}{B} \hat{\zeta}_1 + r\hat{v}_1 = 0, \quad (\text{A.3})$$

$$\frac{\partial \hat{h}_1}{\partial \tau} = -\frac{\partial}{\partial x} \left(3u_0^2 \hat{u}_1 - u_0^2 \lambda \frac{\partial \hat{h}_1}{\partial x} \right) - \left(\frac{n\pi}{B} u_0^2 \hat{v}_1 + \frac{n^2 \pi^2}{B^2} u_0^2 \lambda \hat{h}_1 \right). \quad (\text{A.4})$$

Next, substituting the truncated Fourier series given in Eq.(56) in these equations results in:

$$\frac{\partial U_{1,p}}{\partial x} - U_{0,p} \frac{\partial h_1}{\partial x} + \frac{n\pi}{B} V_{1,p} = 0, \quad (\text{A.5})$$

$$ipU_{1,p} + \sum_{p'=\max(-P,-P+p)}^{\min(P,P+p)} \left[U_{0,p-p'} \frac{\partial U_{1,p'}}{\partial x} \right] + \frac{\partial Z_{1,p}}{\partial x} + rU_{1,p} + rU_{0,p} \hat{h}_1 = 0, \quad (\text{A.6})$$

$$ipV_{1,p} + \sum_{p'=\max(-P,-P+p)}^{\min(P,P+p)} \left[U_{0,p-p'} \frac{\partial V_{1,p'}}{\partial x} \right] - \frac{n\pi}{B} Z_{1,p} + rV_{1,p} = 0, \quad (\text{A.7})$$

$$\begin{aligned} \frac{\partial \hat{h}_1}{\partial \tau} = & -\frac{\partial}{\partial x} \left(\sum_{p'=\max(-P,-P+p)}^{\min(P,P+p)} \left[3D_{UU,-p'} \frac{\partial U_{1,p'}}{\partial x} - U_{0,-p'} U_{0,p'} \lambda \frac{\partial^2 \hat{h}_1}{\partial x^2} \right] \right) \\ & - \left(\sum_{p'=\max(-P,-P+p)}^{\min(P,P+p)} \left[\frac{n\pi}{B} D_{UV,-p'} V_{1,p'} + \frac{n^2 \pi^2}{B^2} U_{0,-p'} U_{0,p'} \lambda \hat{h}_1 \right] \right). \end{aligned} \quad (\text{A.8})$$

These model equations can also be written in matrix notation:

$$\frac{\partial U_{1,p}}{\partial x} - U_{0,p} \frac{\partial h_1}{\partial x} + \frac{n\pi}{B} V_{1,p} = 0, \quad (\text{A.9})$$

$$\mathbf{A}\mathbf{U}_1 + \mathbf{B}_U \frac{\partial \mathbf{U}_1}{\partial x} + \frac{\partial \mathbf{Z}_1}{\partial x} + r\mathbf{U}_1 + r\mathbf{U}_0 \hat{h}_1 = 0, \quad (\text{A.10})$$

$$\mathbf{A}\mathbf{V}_1 + \mathbf{B}_U \frac{\partial \mathbf{V}_1}{\partial x} - \frac{n\pi}{B} \mathbf{Z}_1 + r\mathbf{V}_1 = 0, \quad (\text{A.11})$$

$$\frac{\partial \hat{h}_1}{\partial \tau} = -\frac{\partial}{\partial x} \left(3\mathbf{E}'_{UU} \mathbf{U}_1 - \mathbf{D}'_{UU} \lambda \frac{\partial \hat{h}_1}{\partial x} \right) - \left(\frac{n\pi}{B} \mathbf{E}'_{UV} \mathbf{V}_1 + \frac{n^2 \pi^2}{B^2} \mathbf{D}'_{UU} \lambda \hat{h}_1 \right). \quad (\text{A.12})$$

The vectors and matrices used in these equations are given in Appendix C. Finally, discretising the model equations using the central difference scheme in Eq.(57), results in:

$$-\frac{1}{2\Delta x} \mathbf{U}_{1,m-1} + \frac{1}{2\Delta x} \mathbf{U}_{1,m+1} + \frac{n\pi}{2B} \mathbf{V}_{1,m} + \frac{\mathbf{U}_{0,m}}{2\Delta x} h_{1,m-1} - \frac{\mathbf{U}_{0,m}}{2\Delta x} h_{1,m+1} = 0, \quad (\text{A.13})$$

$$-\frac{1}{2\Delta x}Z_{1,m-1} + \frac{1}{2\Delta x}Z_{1,m+1} - \frac{B_{U,m}}{2\Delta x}U_{1,m-1} + (A+r)U_{1,m} + \frac{B_{U,m}}{2\Delta x}U_{1,m+1} + rU_{0,m}h_{1,m} = 0, \quad (\text{A.14})$$

$$-\frac{n\pi}{B}Z_{1,m} - \frac{B_{U,m}}{2\Delta x}V_{1,m-1} + (A+r)V_{1,m} + \frac{B_{U,m}}{2\Delta x}V_{1,m+1} = 0, \quad (\text{A.15})$$

$$\frac{3E'_{UU,m}}{2\Delta x}U_{1,m-1} - \frac{3E'_{UU,m}}{2\Delta x}U_{1,m+1} - \frac{n\pi}{B}E'_{UU,m}V_{1,m} + \frac{\lambda D'_{UU,m}}{(\Delta x)^2}\hat{h}_{1,m-1} - \left(\frac{2\lambda D'_{UU,m}}{(\Delta x)^2} + \frac{\lambda n^2\pi^2}{B^2}D'_{UU,m}\right)\hat{h}_{1,m} + \frac{\lambda D'_{UU,m}}{(\Delta x)^2}\hat{h}_{1,m+1} = \frac{\partial \hat{h}_{1,m}}{\partial \tau}. \quad (\text{A.16})$$

A.2 Rewritten model equations for the perturbed state of the NRL model

The model equations for the perturbed state of the NRL model (see Eq.(65), Eq.(66), Eq.(70) and Eq.(71) in Chapter 5) are linearised by substituting the expressions given in Eq.(55) in these equations. This results in:

$$\frac{\partial \hat{\zeta}_1}{\partial t} + \frac{\partial \hat{u}_1}{\partial x} - u_0 \frac{\partial \hat{h}_1}{\partial x} - \hat{h}_1 \frac{\partial u_0}{\partial x} + \delta u_0 \frac{\partial \hat{\zeta}_1}{\partial x} + \delta \hat{u}_1 \frac{\partial \zeta_0}{\partial x} + \delta \zeta_0 \frac{\partial \hat{u}_1}{\partial x} + \delta \hat{\zeta}_1 \frac{\partial u_0}{\partial x} + \frac{n\pi}{B}\hat{v}_1 + \delta \frac{n\pi}{B}\zeta_0\hat{v}_1 = 0, \quad (\text{A.17})$$

$$\frac{\partial \hat{u}_1}{\partial t} + \delta u_0 \frac{\partial \hat{u}_1}{\partial x} + \delta \hat{u}_1 \frac{\partial u_0}{\partial x} + \frac{\partial \hat{\zeta}_1}{\partial x} + r\hat{u}_1 + ru_0\hat{h}_1 - \delta r\zeta_0\hat{u}_1 - 2\delta r\zeta_0u_0\hat{h}_1 - \delta ru_0\hat{\zeta}_1 = 0, \quad (\text{A.18})$$

$$\frac{\partial \hat{v}_1}{\partial t} + \delta u_0 \frac{\partial \hat{v}_1}{\partial x} - \frac{n\pi}{B}\hat{\zeta}_1 + r\hat{v}_1 - \delta r\zeta_0\hat{v}_1 = 0, \quad (\text{A.19})$$

$$\frac{\partial \hat{h}_1}{\partial \tau} = -\frac{\partial}{\partial x} \langle 3u_0^2\hat{u}_1 - u_0^2\lambda \frac{\partial \hat{h}_1}{\partial x} \rangle - \langle \frac{n\pi}{B}u_0^2\hat{v}_1 + \frac{n^2\pi^2}{B^2}u_0^2\lambda\hat{h}_1 \rangle. \quad (\text{A.20})$$

Next, substituting the truncated Fourier series given in Eq.(56) in these equations results in:

$$ipZ_{1,p} + \frac{\partial U_{1,p}}{\partial x} - U_{0,p} \frac{\partial \hat{h}_1}{\partial x} - \hat{h}_1 \frac{\partial U_{0,p}}{\partial x} + \sum_{p'=\max(-P,-P+p)}^{\min(P,P+p)} \left[\delta U_{0,p-p'} \frac{\partial Z_{1,p'}}{\partial x} + U_{1,p'} \frac{\partial Z_{0,p-p'}}{\partial x} + \delta Z_{0,p-p'} \frac{\partial U_{1,p'}}{\partial x} + \delta Z_{1,p'} \frac{\partial U_{0,p-p'}}{\partial x} \right] + \frac{n\pi}{B}V_{1,p} + \sum_{p'=\max(-P,-P+p)}^{\min(P,P+p)} \left[\delta \frac{n\pi}{B}Z_{0,p-p'}V_{1,p'} \right] = 0, \quad (\text{A.21})$$

$$pU_{1,p} + \sum_{p'=\max(-P,-P+p)}^{\min(P,P+p)} \left[\delta U_{0,p-p'} \frac{\partial U_{1,p'}}{\partial x} + \delta U_{1,p'} \frac{\partial U_{0,p-p'}}{\partial x} \right] + \frac{\partial Z_{1,p}}{\partial x} + rU_{1,p} + rU_{0,p}\hat{h}_1 + \sum_{p'=\max(-P,-P+p)}^{\min(P,P+p)} \left[-\delta rZ_{0,p-p'}U_{1,p'} - 2\delta rZ_{0,p-p'}U_{0,p'}\hat{h}_1 - \delta rU_{0,p-p'}Z_{1,p'} \right] = 0, \quad (\text{A.22})$$

$$ipV_{1,p} + \delta \sum_{p'=\max(-P,-P+p)}^{\min(P,P+p)} \left[U_{0,p-p'} \frac{\partial V_{1,p'}}{\partial x} \right] - \frac{n\pi}{B}Z_{1,p} + rV_{1,p} - \delta rZ_{0,p-p'}V_{1,p'} = 0, \quad (\text{A.23})$$

$$\frac{\partial \hat{h}_1}{\partial \tau} = -\frac{\partial}{\partial x} \left(\sum_{p'=\max(-P,-P+p)}^{\min(P,P+p)} \left[3D_{UU,-p'} \frac{\partial U_{1,p'}}{\partial x} - U_{0,-p'}U_{0,p'}\lambda \frac{\partial^2 \hat{h}_1}{\partial x^2} \right] \right) - \left(\sum_{p'=\max(-P,-P+p)}^{\min(P,P+p)} \left[\frac{n\pi}{B}D_{UU,-p'}V_{1,p'} + \frac{n^2\pi^2}{B^2}U_{0,-p'}U_{0,p'}\lambda\hat{h}_1 \right] \right). \quad (\text{A.24})$$

These model equations can also be written in matrix notation:

$$\begin{aligned} \mathbf{A}\mathbf{Z}_1 + \frac{\partial \mathbf{U}_1}{\partial x} - \mathbf{U}_0 \frac{\partial \hat{h}_1}{\partial x} - \hat{h}_1 \frac{\partial \mathbf{U}_0}{\partial x} + \delta \mathbf{B}_U \frac{\partial \mathbf{Z}_1}{\partial x} + \delta \frac{\partial \mathbf{B}_Z}{\partial x} \mathbf{U}_1 + \delta \mathbf{B}_Z \frac{\partial \mathbf{U}_1}{\partial x} + \delta \frac{\partial \mathbf{B}_U}{\partial x} \mathbf{Z}_1 \\ + \frac{n\pi}{B} \mathbf{V}_1 + \delta \frac{n\pi}{B} \mathbf{B}_Z \mathbf{V}_1 = 0, \end{aligned} \quad (\text{A.25})$$

$$\begin{aligned} \mathbf{A}\mathbf{U}_1 + \delta \mathbf{B}_U \frac{\partial \mathbf{U}_1}{\partial x} + \delta \frac{\partial \mathbf{B}_U}{\partial x} \mathbf{U}_1 + \frac{\partial \mathbf{Z}_1}{\partial x} + r\mathbf{U}_1 + r\mathbf{U}_0 \hat{h}_1 - \delta r \mathbf{B}_Z \mathbf{U}_1 - 2\delta r \mathbf{D}_{ZU} \hat{h}_1 \\ - \delta r \mathbf{B}_U \mathbf{Z}_1 = 0, \end{aligned} \quad (\text{A.26})$$

$$\mathbf{A}\mathbf{V}_1 + \delta \mathbf{B}_U \frac{\partial \mathbf{V}_1}{\partial x} - \frac{n\pi}{B} \mathbf{Z}_1 + r\mathbf{V}_1 - \delta r \mathbf{B}_Z \mathbf{V}_1 = 0, \quad (\text{A.27})$$

$$\frac{\partial \hat{h}_1}{\partial \tau} = -\frac{\partial}{\partial x} \left(3\mathbf{E}'_{UU} \mathbf{U}_1 - \mathbf{D}'_{UU} \lambda \frac{\partial \hat{h}_1}{\partial x} \right) - \left(\frac{n\pi}{B} \mathbf{E}'_{UV} \mathbf{V}_1 + \frac{n^2 \pi^2}{B^2} \mathbf{D}'_{UU} \lambda \hat{h}_1 \right). \quad (\text{A.28})$$

The vectors and matrices used in these equations are given in Appendix C. Finally, discretising the model equations using the central difference scheme in Eq.(57), results in:

$$\begin{aligned} -\frac{\delta \mathbf{B}_{U,m}}{2\Delta x} \mathbf{Z}_{1,m-1} + \left(\mathbf{A} + \frac{\delta(\mathbf{B}_{U,m+1} - \mathbf{B}_{U,m-1})}{2\Delta x} \right) \mathbf{Z}_{1,m} + \frac{\delta \mathbf{B}_{U,m}}{2\Delta x} \mathbf{Z}_{1,m+1} \\ -\frac{1 + \delta \mathbf{B}_{Z,m}}{2\Delta x} \mathbf{U}_{1,m-1} + \frac{\delta(\mathbf{B}_{Z,m+1} - \mathbf{B}_{Z,m-1})}{2\Delta x} \mathbf{U}_{1,m} + \frac{1 + \delta \mathbf{B}_{Z,m}}{2\Delta x} \mathbf{U}_{1,m+1} \\ + \frac{n\pi(1 + \delta \mathbf{B}_{Z,m})}{B} \mathbf{V}_{1,m} + \frac{\mathbf{U}_{0,m}}{2\Delta x} \hat{h}_{1,m-1} - \frac{\mathbf{U}_{0,m+1} - \mathbf{U}_{0,m-1}}{2\Delta x} \hat{h}_{1,m} - \frac{\mathbf{U}_{0,m}}{2\Delta x} \hat{h}_{1,m+1} = 0, \end{aligned} \quad (\text{A.29})$$

$$\begin{aligned} -\frac{1}{2\Delta x} \mathbf{Z}_{1,m-1} - \delta r \mathbf{B}_{U,m} \mathbf{Z}_{1,m} + \frac{1}{2\Delta x} \mathbf{Z}_{1,m+1} - \frac{\delta \mathbf{B}_{U,m}}{2\Delta x} \mathbf{U}_{1,m-1} \\ + \left(\mathbf{A} + \frac{\delta(\mathbf{B}_{U,m+1} - \mathbf{B}_{U,m-1})}{2\Delta x} + r - \delta r \mathbf{B}_{Z,m} \right) \mathbf{U}_{1,m} + \frac{\delta \mathbf{B}_{U,m}}{2\Delta x} \mathbf{U}_{1,m+1} \\ + r(\mathbf{U}_{0,m} - 2\delta \mathbf{D}_{ZU,m}) \hat{h}_{1,m} = 0, \end{aligned} \quad (\text{A.30})$$

$$\begin{aligned} -\frac{n\pi}{B} \mathbf{Z}_{1,m} - \frac{\delta \mathbf{B}_{U,m}}{2\Delta x} \mathbf{V}_{1,m-1} + (\mathbf{A} + r - \delta r \mathbf{B}_{Z,m}) \mathbf{V}_{1,m} + \frac{\delta \mathbf{B}_{U,m}}{2\Delta x} \mathbf{V}_{1,m+1} = 0, \end{aligned} \quad (\text{A.31})$$

$$\begin{aligned} \frac{3\mathbf{E}'_{UU,m}}{2\Delta x} \mathbf{U}_{1,m-1} - \frac{3(\mathbf{E}'_{UU,m+1} - \mathbf{E}'_{UU,m-1})}{2\Delta x} \mathbf{U}_{1,m} - \frac{3\mathbf{E}'_{UU,m}}{2\Delta x} \mathbf{U}_{1,m+1} - \frac{n\pi}{B} \mathbf{E}'_{UV} \mathbf{V}_{1,m} \\ - \frac{\lambda(\mathbf{D}'_{UU,m+1} - 4\mathbf{D}'_{UU,m} - \mathbf{D}'_{UU,m-1})}{4(\Delta x)^2} \hat{h}_{1,m-1} - \left(\frac{2\lambda \mathbf{D}'_{UU,m}}{(\Delta x)^2} + \frac{\lambda n^2 \pi^2}{B^2} \mathbf{D}'_{UU,m} \right) \hat{h}_{1,m} \\ + \frac{\lambda(\mathbf{D}'_{UU,m+1} + 4\mathbf{D}'_{UU,m} - \mathbf{D}'_{UU,m-1})}{4(\Delta x)^2} \hat{h}_{1,m+1} = \frac{\partial \hat{h}_{1,m}}{\partial \tau}. \end{aligned} \quad (\text{A.32})$$

$$\begin{aligned}
 & \begin{bmatrix}
 \frac{\pi\tau(1+\delta B_{z0})}{B} & 0 & 0 & \dots & 0 & -\frac{\partial U_{00}}{\partial x} & -\frac{U_{00}}{2\Delta x} & 0 & \dots & \frac{U_{00}}{2\Delta x} \\
 0 & \frac{\pi\tau(1+\delta B_{z1})}{B} & 0 & \dots & 0 & \frac{U_{01}}{2\Delta x} & -\frac{\partial U_{01}}{\partial x} & -\frac{U_{01}}{2\Delta x} & \dots & 0 \\
 0 & 0 & \frac{\pi\tau(1+\delta B_{z2})}{B} & \dots & 0 & 0 & \frac{U_{02}}{2\Delta x} & -\frac{\partial U_{02}}{\partial x} & \dots & 0 \\
 \vdots & \vdots & \vdots & \ddots & \vdots & \vdots & \vdots & \vdots & \ddots & \vdots \\
 0 & 0 & 0 & \dots & \frac{\pi\tau(1+\delta B_{z_{M-1}})}{B} & -\frac{U_{0_{M-1}}}{2\Delta x} & 0 & 0 & \dots & -\frac{\partial U_{0_{M-1}}}{\partial x} \\
 0 & 0 & 0 & \dots & 0 & r(U_{00}-2\delta D_{zu0}) & 0 & 0 & \dots & 0 \\
 0 & 0 & 0 & \dots & 0 & 0 & r(U_{01}-2\delta D_{zu1}) & 0 & \dots & 0 \\
 0 & 0 & 0 & \dots & 0 & 0 & 0 & r(U_{02}-2\delta D_{zu2}) & \dots & 0 \\
 \vdots & \vdots & \vdots & \ddots & \vdots & \vdots & \vdots & \vdots & \ddots & \vdots \\
 0 & 0 & 0 & \dots & 0 & 0 & 0 & 0 & \dots & r(U_{0_{M-1}}-2\delta D_{z_{UM-1}}) \\
 \vdots & \vdots & \vdots & \ddots & \vdots & \vdots & \vdots & \vdots & \ddots & \vdots \\
 0 & 0 & 0 & \dots & 0 & 0 & 0 & 0 & \dots & 0
 \end{bmatrix} \\
 & = \begin{bmatrix}
 A+r-\delta\tau B_{z0} & \frac{\delta B_{u0}}{2\Delta x} & 0 & \dots & -\frac{\delta B_{u0}}{2\Delta x} & 0 & 0 & 0 & \dots & 0 \\
 \frac{\delta B_{u1}}{2\Delta x} & A+r-\delta\tau B_{z1} & \frac{\delta B_{u1}}{2\Delta x} & \dots & 0 & 0 & 0 & 0 & \dots & 0 \\
 0 & \frac{\delta B_{u2}}{2\Delta x} & A+r-\delta\tau B_{z2} & \dots & 0 & 0 & 0 & 0 & \dots & 0 \\
 \vdots & \vdots & \vdots & \ddots & \vdots & \vdots & \vdots & \vdots & \ddots & \vdots \\
 \frac{\delta B_{u_{M-1}}}{2\Delta x} & 0 & 0 & \dots & A+r-\delta\tau B_{z_{M-1}} & 0 & 0 & 0 & \dots & 0 \\
 -\frac{\pi\tau}{B} E'_{uu0} & 0 & 0 & \dots & 0 & -\frac{2\lambda D'_{uu0}}{(\Delta x)^2} - \frac{\lambda\pi^2\tau^2}{B^2} D'_{uu0} & \frac{\lambda D'_{uu0}}{(\Delta x)^2} + \frac{\lambda}{2\Delta x} \frac{\partial D'_{uu0}}{\partial x} & 0 & \dots & \frac{\lambda D'_{uu0}}{(\Delta x)^2} - \frac{\lambda}{2\Delta x} \frac{\partial D'_{uu0}}{\partial x} \\
 0 & -\frac{\pi\tau}{B} E'_{uu1} & 0 & \dots & 0 & -\frac{2\lambda D'_{uu1}}{(\Delta x)^2} - \frac{\lambda\pi^2\tau^2}{B^2} D'_{uu1} & \frac{\lambda D'_{uu1}}{(\Delta x)^2} + \frac{\lambda}{2\Delta x} \frac{\partial D'_{uu1}}{\partial x} & -\frac{2\lambda D'_{uu1}}{(\Delta x)^2} - \frac{\lambda\pi^2\tau^2}{B^2} D'_{uu1} & \dots & 0 \\
 0 & 0 & -\frac{\pi\tau}{B} E'_{uu2} & \dots & 0 & -\frac{2\lambda D'_{uu2}}{(\Delta x)^2} - \frac{\lambda\pi^2\tau^2}{B^2} D'_{uu2} & \frac{\lambda D'_{uu2}}{(\Delta x)^2} + \frac{\lambda}{2\Delta x} \frac{\partial D'_{uu2}}{\partial x} & -\frac{2\lambda D'_{uu2}}{(\Delta x)^2} - \frac{\lambda\pi^2\tau^2}{B^2} D'_{uu2} & \dots & 0 \\
 \vdots & \vdots & \vdots & \ddots & \vdots & \vdots & \vdots & \vdots & \ddots & \vdots \\
 0 & 0 & 0 & \dots & -\frac{\pi\tau}{B} E'_{uu_{M-1}} & -\frac{2\lambda D'_{uu_{M-1}}}{(\Delta x)^2} - \frac{\lambda\pi^2\tau^2}{B^2} D'_{uu_{M-1}} & \frac{\lambda D'_{uu_{M-1}}}{(\Delta x)^2} + \frac{\lambda}{2\Delta x} \frac{\partial D'_{uu_{M-1}}}{\partial x} & -\frac{2\lambda D'_{uu_{M-1}}}{(\Delta x)^2} - \frac{\lambda\pi^2\tau^2}{B^2} D'_{uu_{M-1}} & \dots & -\frac{2\lambda D'_{uu_{M-1}}}{(\Delta x)^2} - \frac{\lambda\pi^2\tau^2}{B^2} D'_{uu_{M-1}}
 \end{bmatrix} \\
 & \begin{matrix}
 C_{13} & C_{14} \\
 C_{23} & C_{24} \\
 C_{33} & C_{34} \\
 C_{43} & C_{44}
 \end{matrix}
 \end{aligned}
 \tag{B.5}$$

For $P = 2$ each term in this matrix becomes a 5-by-5 submatrix.

Appendix C: Vectors and matrices

The vectors and matrices (for $P = 2$) used in this report are shown below. The vectors for the non-zero system variables in the basic and perturbed state are:

$$\mathbf{Z}_0 = \begin{bmatrix} Z_{0,-2} \\ Z_{0,-1} \\ Z_{0,0} \\ Z_{0,1} \\ Z_{0,2} \end{bmatrix}, \quad \mathbf{U}_0 = \begin{bmatrix} U_{0,-2} \\ U_{0,-1} \\ U_{0,0} \\ U_{0,1} \\ U_{0,2} \end{bmatrix}, \quad \mathbf{Z}_1 = \begin{bmatrix} Z_{1,-2} \\ Z_{1,-1} \\ Z_{1,0} \\ Z_{1,1} \\ Z_{1,2} \end{bmatrix}, \quad \mathbf{U}_1 = \begin{bmatrix} U_{1,-2} \\ U_{1,-1} \\ U_{1,0} \\ U_{1,1} \\ U_{1,2} \end{bmatrix}, \quad \mathbf{V}_1 = \begin{bmatrix} V_{1,-2} \\ V_{1,-1} \\ V_{1,0} \\ V_{1,1} \\ V_{1,2} \end{bmatrix}. \quad (\text{C.1})$$

\mathbf{A} is a diagonal matrix filled with ip -terms that correspond to the time derivative:

$$\mathbf{A} = \begin{bmatrix} -2i & 0 & 0 & 0 & 0 \\ 0 & -i & 0 & 0 & 0 \\ 0 & 0 & 0 & 0 & 0 \\ 0 & 0 & 0 & i & 0 \\ 0 & 0 & 0 & 0 & 2i \end{bmatrix}. \quad (\text{C.2})$$

\mathbf{B}_Z and \mathbf{B}_U are convolution matrices that correspond to the advection terms in the momentum equations (e.g., $u_0 \frac{\partial u_1}{\partial x}$):

$$\mathbf{B}_Z = \begin{bmatrix} Z_{0,0} & Z_{0,-1} & Z_{0,-2} & 0 & 0 \\ Z_{0,1} & Z_{0,0} & Z_{0,-1} & Z_{0,-2} & 0 \\ Z_{0,2} & Z_{0,1} & Z_{0,0} & Z_{0,-1} & Z_{0,-2} \\ 0 & Z_{0,2} & Z_{0,1} & Z_{0,0} & Z_{0,-1} \\ 0 & 0 & Z_{0,2} & Z_{0,1} & Z_{0,0} \end{bmatrix}, \quad \mathbf{B}_U = \begin{bmatrix} U_{0,0} & U_{0,-1} & U_{0,-2} & 0 & 0 \\ U_{0,1} & U_{0,0} & U_{0,-1} & U_{0,-2} & 0 \\ U_{0,2} & U_{0,1} & U_{0,0} & U_{0,-1} & U_{0,-2} \\ 0 & U_{0,2} & U_{0,1} & U_{0,0} & U_{0,-1} \\ 0 & 0 & U_{0,2} & U_{0,1} & U_{0,0} \end{bmatrix}. \quad (\text{C.3})$$

\mathbf{B}'_Z and \mathbf{B}'_U are the vectors on the centre row of the \mathbf{B}_Z and \mathbf{B}_U convolution matrices:

$$\mathbf{B}'_Z = [Z_{0,2} \quad Z_{0,1} \quad Z_{0,0} \quad Z_{0,-1} \quad Z_{0,-2}], \quad \mathbf{B}'_U = [U_{0,2} \quad U_{0,1} \quad U_{0,0} \quad U_{0,-1} \quad U_{0,-2}]. \quad (\text{C.4})$$

\mathbf{D}_{ZU} and \mathbf{D}_{UU} are the vectors that result from multiplying the \mathbf{B}_U convolution matrix with the \mathbf{Z}_0 and \mathbf{U}_0 vectors, respectively:

$$\mathbf{D}_{ZU} = \mathbf{B}_Z \mathbf{U}_0 = \begin{bmatrix} Z_{0,0} & Z_{0,-1} & Z_{0,-2} & 0 & 0 \\ Z_{0,1} & Z_{0,0} & Z_{0,-1} & Z_{0,-2} & 0 \\ Z_{0,2} & Z_{0,1} & Z_{0,0} & Z_{0,-1} & Z_{0,-2} \\ 0 & Z_{0,2} & Z_{0,1} & Z_{0,0} & Z_{0,-1} \\ 0 & 0 & Z_{0,2} & Z_{0,1} & Z_{0,0} \end{bmatrix} \cdot \begin{bmatrix} U_{0,-2} \\ U_{0,-1} \\ U_{0,0} \\ U_{0,1} \\ U_{0,2} \end{bmatrix} = \begin{bmatrix} D_{ZU,-2} \\ D_{ZU,-1} \\ D_{ZU,0} \\ D_{ZU,1} \\ D_{ZU,2} \end{bmatrix},$$

$$\mathbf{D}_{UU} = \mathbf{B}_U \mathbf{U}_0 = \begin{bmatrix} U_{0,0} & U_{0,-1} & U_{0,-2} & 0 & 0 \\ U_{0,1} & U_{0,0} & U_{0,-1} & U_{0,-2} & 0 \\ U_{0,2} & U_{0,1} & U_{0,0} & U_{0,-1} & U_{0,-2} \\ 0 & U_{0,2} & U_{0,1} & U_{0,0} & U_{0,-1} \\ 0 & 0 & U_{0,2} & U_{0,1} & U_{0,0} \end{bmatrix} \cdot \begin{bmatrix} U_{0,-2} \\ U_{0,-1} \\ U_{0,0} \\ U_{0,1} \\ U_{0,2} \end{bmatrix} = \begin{bmatrix} D_{UU,-2} \\ D_{UU,-1} \\ D_{UU,0} \\ D_{UU,1} \\ D_{UU,2} \end{bmatrix}. \quad (\text{C.5})$$

D'_{UU} is the scalar that results from multiplying the B'_U vector with the U_0 vector:

$$D'_{UU} = B'_U U_0 = [U_{0,2} \quad U_{0,1} \quad U_{0,0} \quad U_{0,-1} \quad U_{0,-2}] \cdot \begin{bmatrix} U_{0,-2} \\ U_{0,-1} \\ U_{0,0} \\ U_{0,1} \\ U_{0,2} \end{bmatrix} = D_{UU,0}. \quad (\text{C.6})$$

E_{UU} is the convolution matrix that corresponds to the quadratic terms in the bed evolution equation (e.g., $u_0^2 u_1$):

$$E_{UU} = \begin{bmatrix} D_{UU,0} & D_{UU,-1} & D_{UU,-2} & 0 & 0 \\ D_{UU,1} & D_{UU,0} & D_{UU,-1} & D_{UU,-2} & 0 \\ D_{UU,2} & D_{UU,1} & D_{UU,0} & D_{UU,-1} & D_{UU,-2} \\ 0 & D_{UU,2} & D_{UU,1} & D_{UU,0} & D_{UU,-1} \\ 0 & 0 & D_{UU,2} & D_{UU,1} & D_{UU,0} \end{bmatrix}. \quad (\text{C.7})$$

E'_{UU} is the vector on the centre row of the E_{UU} convolution matrix:

$$E'_{UU} = [D_{U,2} \quad D_{U,1} \quad D_{U,0} \quad D_{U,-1} \quad D_{U,-2}]. \quad (\text{C.8})$$

Appendix D: Method to construct growth curves for multichromatic bedforms

A detailed description of the method developed and used in this study to construct growth curves for multichromatic bedforms is given below. A generalised eigenvalue problem is defined as part of the numerical solution procedure (see Subsection 4.3.2). The eigenvalues and eigenvectors that follow from this problem are used to determine the structures and characteristics of the bedforms. Finally, note that the number of bedforms that follow from the generalised eigenvalue problem is equal to the total number of points used in the discretisation (M). For example, $M = 801$ results in 801 individual bedforms each with their own structure and growth rate.

Figure 18a shows a single multichromatic bedform structure. A discrete Fourier transform (with a fast Fourier transform algorithm) is used to decompose this bedform into its monochromatic sinusoidal components. This results in the Discrete Fourier Transform (DFT) spectrum shown in Figure 18b. The DFT spectrum shows a (arbitrary) magnitude as a function of the wavenumbers. The magnitude (ranging from 0 to 1) represents the amount that a sinusoidal component (with a single wavenumber) is present in the multichromatic bedform structure. The most dominant component that is present in a particular structure has a magnitude of 1. Based on the DFT spectrum, the growth rate for a multichromatic bedform structure is assigned to the three most dominant components that are present in that structure. The growth rate for the bedform structure in Figure 18 is thus assigned to the sinusoidal components with wavenumbers of approximately $k_m^* = 0.30, 0.34$ and 0.38 km^{-1} (see \times in Figure 18b).

The abovementioned procedure is repeated for all multichromatic bedform structures. After this is done, each sinusoidal component (with a corresponding wavenumber) is characterised by zero, one or multiple growth rates that were assigned when repeating the abovementioned procedure. Next, an upper (and lower) limit is determined by plotting lines through the highest (and lowest) growth rate that is assigned to each wavenumber. The growth area is defined as the area between these limits (e.g., see shaded areas in Figure 14). Finally, the growth curve is constructed using the upper limit of the growth area (see dashed lines in Figure 14).

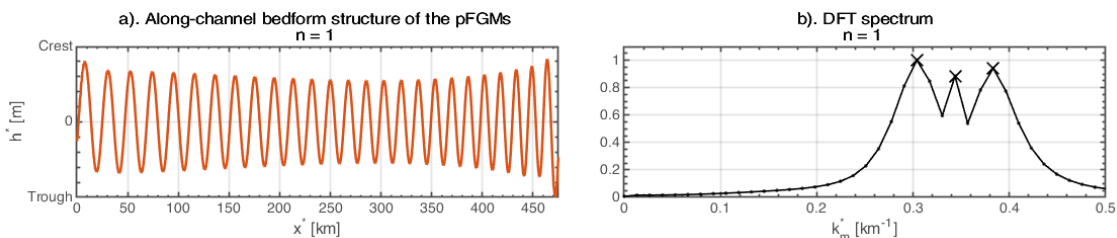


Figure 18: (a) Along-channel bedform structure of the pFGM for a cross-channel mode of $n = 0$; and (b) the corresponding Discrete Fourier Transform (DFT) spectra of the pFGM. The bedform structure is shown for the NRL model (Figure 3) applied to the reduced friction case in the Western Scheldt (Table 1). \times denotes the wavenumbers (k_m^* in km^{-1}) of the three monochromatic sinusoidal components that are most strongly present in the corresponding multichromatic bedform structure.

Appendix E: NRL model with non-periodic boundary conditions

The solutions to the perturbed state for the NRL model with different sets of non-periodic boundary conditions are shown below. Because of the non-periodic boundary conditions, the central difference scheme (i.e., Eq.(57)) cannot be used at both ends of the model domain (i.e., at $x = 0$ and 475 km). Therefore, a forward difference scheme (at $m = 0$) and a backward difference scheme (at $m = M - 1$) are used to approximate the first order and second order derivatives in the along-channel direction:

$$\left. \frac{\partial \phi}{\partial x} \right|_{x_m} \approx \frac{\phi_{m+1} - \phi_m}{\Delta x}, \quad \left. \frac{d^2 \phi}{dx^2} \right|_{x_m} \approx \frac{\phi_{m+2} - 2\phi_{m+1} + \phi_m}{(\Delta x)^2}, \quad \text{for } m = 0, \quad (\text{D.1})$$

and:

$$\left. \frac{\partial \phi}{\partial x} \right|_{x_m} \approx \frac{\phi_m - \phi_{m-1}}{\Delta x}, \quad \left. \frac{d^2 \phi}{dx^2} \right|_{x_m} \approx \frac{\phi_m - 2\phi_{m-1} + \phi_{m-2}}{(\Delta x)^2}, \quad \text{for } m = M - 1, \quad (\text{D.2})$$

respectively. The solutions to the perturbed state are given for three sets of non-periodic boundary conditions (see Table 4): Unspecified; Neumann; and Neumann and Dirichlet. The unspecified set is based on the model equations used throughout the whole model domain (i.e., Eq.(A.25) to Eq.(A.28)). However, the forward and backward difference schemes are used to discretise these model equations at the boundaries of the domain. As a result, the boundaries are non-periodic without imposing a specific boundary condition. The other two sets do specifically impose boundary conditions at the ends of the model domain.

Table 4: Sets of non-periodic boundary conditions and the corresponding figures in which the solutions to the perturbed state are shown.

Set	Name	Boundary conditions	Solution to the perturbed state
1	Unspecified ¹	-	Figure 19, Figure 22
2	Neumann	$\frac{\partial \zeta_1}{\partial x} = 0, \quad \frac{\partial u_1}{\partial x} = 0, \quad \frac{\partial v_1}{\partial x} = 0, \quad \frac{\partial h_1}{\partial x} = 0$	Figure 20, Figure 23
3	Neumann and Dirichlet	$\frac{\partial \zeta_1}{\partial x} = 0, \quad \frac{\partial u_1}{\partial x} = 0, \quad \frac{\partial v_1}{\partial x} = 0, \quad h_1 = 0$	Figure 21, Figure 24

¹The unspecified boundary conditions are determined by applying the forward and backward difference schemes to the model equations given in Eq.(A.25) to Eq.(A.28).

Figure 19 to Figure 21 contain the growth curves (and areas) showing the growth rate (ω_m^*) as a function of the morphological wavenumber (k_m^*) for different cross-channel modes (n). The growth curves (and areas) are shown for the reduced friction case in the Western Scheldt (see Table 1). The three figures correspond to the NRL model with different sets of non-periodic boundary conditions in Table 4. The solid lines and dashed lines (with shaded areas) represent the growth curves for the (semi-analytical) RL model and the growth curves (with growth areas) for the (numerical) NRL model with non-periodic boundary conditions, respectively. + and × denote the FGM for the RL and NRL model, respectively. Moreover, • denotes the partial fastest growing mode (pFGM) for each cross-channel mode. Recall that the pFGMs are the FGM for each individual cross-channel mode.

Moreover, Figure 22 to Figure 24 contain the along-channel bedform structures of the pFGMs for the three lowest cross-channel modes (i.e., $n = 0$ to 2). The bedforms are shown for the reduced friction case in the Western Scheldt (see Table 1). The three figures correspond to the NRL model with different sets of non-periodic boundary conditions in Table 4. These figures also show the corresponding Discrete Fourier Transform (DFT) spectra of the pFGMs.

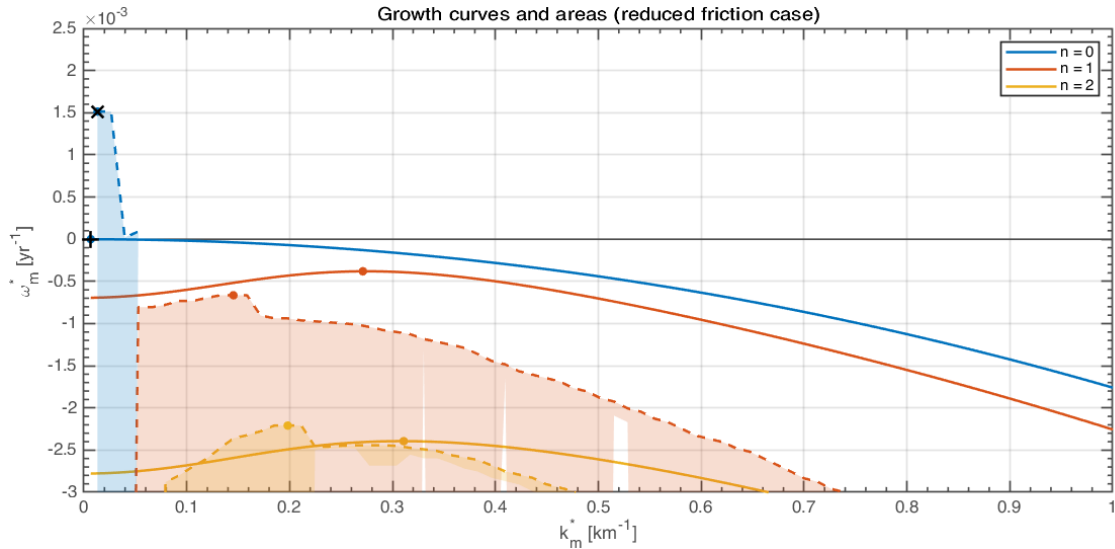


Figure 19: Growth curves (and areas) showing the growth rate (ω_m^* in yr^{-1}) as a function of the morphological wavenumber (k_m^* in km^{-1}) for different cross-channel modes (n). The growth curves (and areas) are shown for the reduced friction case in the Western Scheldt (Table 1). The solid lines and dashed lines (with shaded areas) represent the growth curves for the (semi-analytical) RL model and the growth curves (with growth areas for the (numerical) NRL model with unspecified boundary conditions (Table 4), respectively. •, † and × denote the pFGM for each cross-channel mode, the FGM for the RL model and the FGM for the NRL model, respectively.

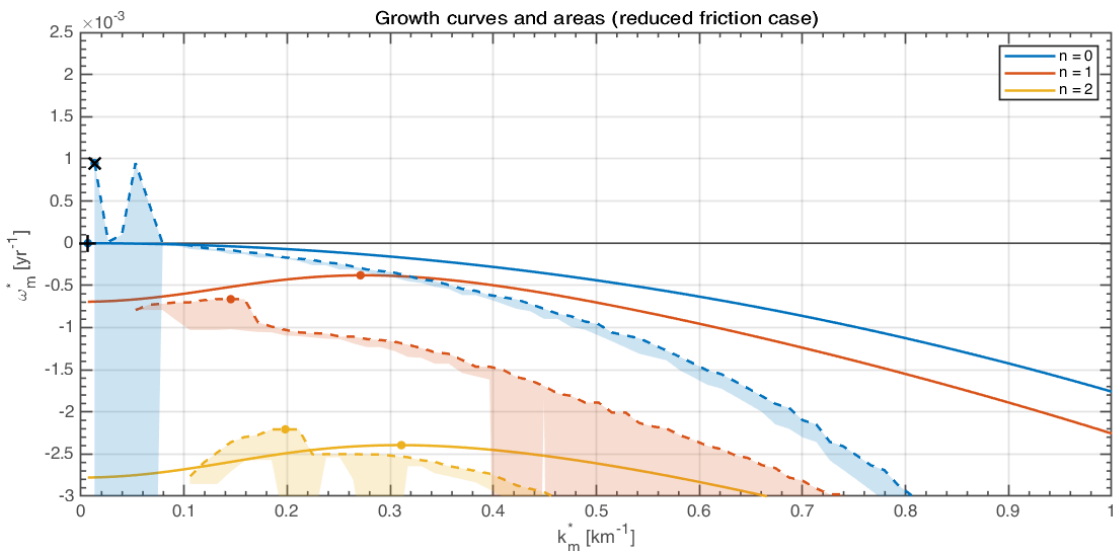


Figure 20: Growth curves (and areas) showing the growth rate (ω_m^* in yr^{-1}) as a function of the morphological wavenumber (k_m^* in km^{-1}) for different cross-channel modes (n). The growth curves (and areas) are shown for the reduced friction case in the Western Scheldt (Table 1). The solid lines and dashed lines (with shaded areas) represent the growth curves for the (semi-analytical) RL model and the growth curves (with growth areas for the (numerical) NRL model with Neumann boundary conditions (Table 4), respectively. •, † and × denote the pFGM for each cross-channel mode, the FGM for the RL model and the FGM for the NRL model, respectively.

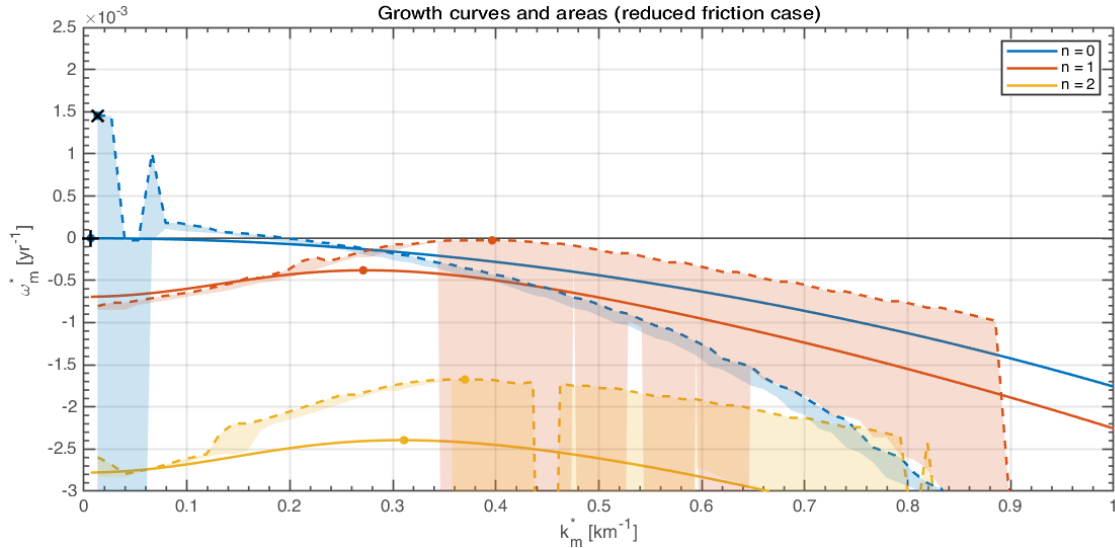


Figure 21: Growth curves (and areas) showing the growth rate (ω_m^* in yr^{-1}) as a function of the morphological wavenumber (k_m^* in km^{-1}) for different cross-channel modes (n). The growth curves (and areas) are shown for the reduced friction case in the Western Scheldt (Table 1). The solid lines and dashed lines (with shaded areas) represent the growth curves for the (semi-analytical) RL model and the growth curves (with growth areas for the (numerical) NRL model with Neumann and Dirichlet boundary conditions (Table 4), respectively. •, + and × denote the pFGM for each cross-channel mode, the FGM for the RL model and the FGM for the NRL model, respectively.

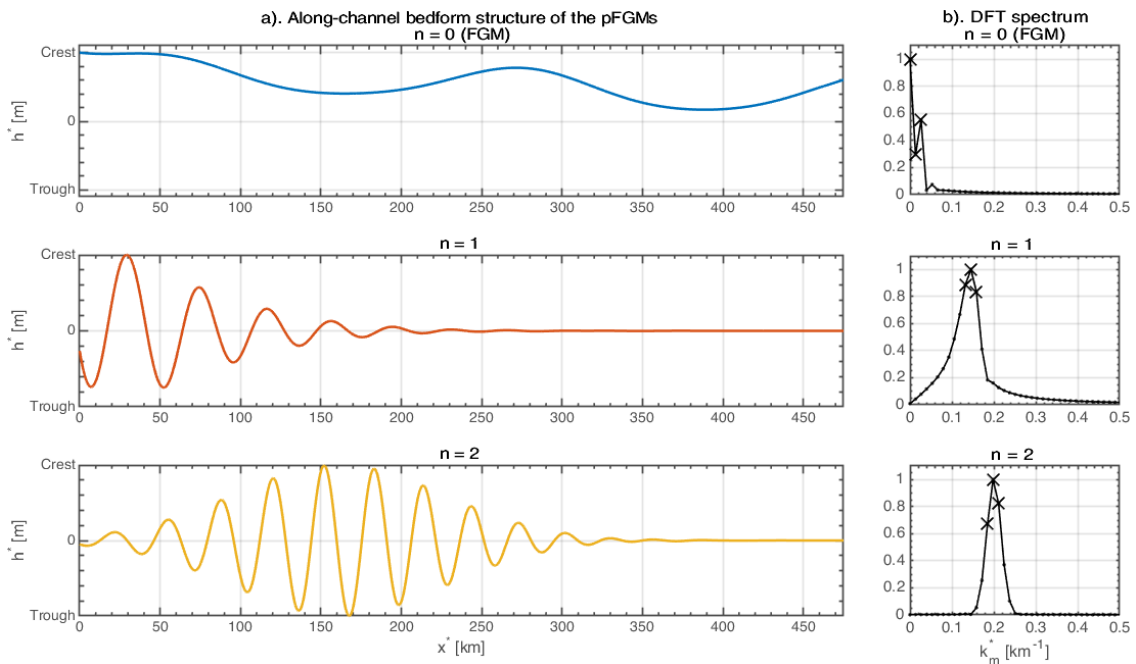


Figure 22: (a) Along-channel bedform structures of the pFGMs for the three lowest cross-channel modes (n); and (b) the corresponding Discrete Fourier Transform (DFT) spectra of the pFGMs. The bedform structures are shown for the NRL model with unspecified boundary conditions (Table 4) applied to the reduced friction case in the Western Scheldt (Table 1). × denotes the wavenumbers (k_m^* in km^{-1}) of the three monochromatic sinusoidal components that are most strongly present in the corresponding multichromatic bedform structure.

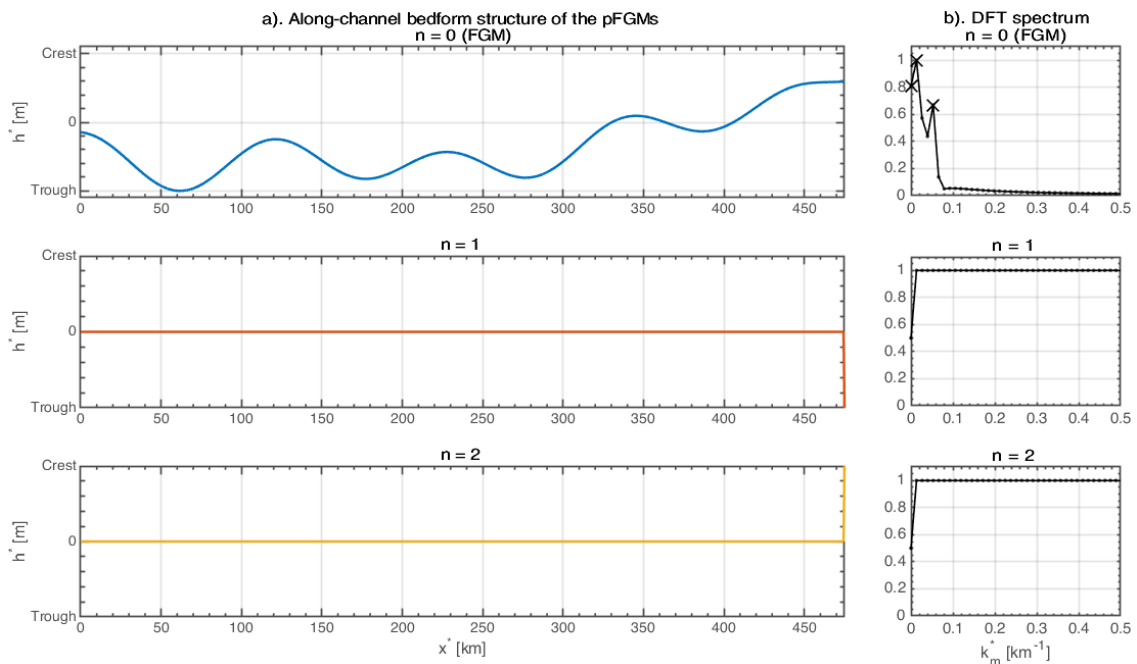


Figure 23: (a) Along-channel bedform structures of the pFGMs for the three lowest cross-channel modes (n); and (b) the corresponding Discrete Fourier Transform (DFT) spectra of the pFGMs. The bedform structures are shown for the NRL model with Neumann boundary conditions (Table 4) applied to the reduced friction case in the Western Scheldt (Table 1). \times denotes the wavenumbers (k_m^* in km^{-1}) of the three monochromatic sinusoidal components that are most strongly present in the corresponding multichromatic bedform structure.

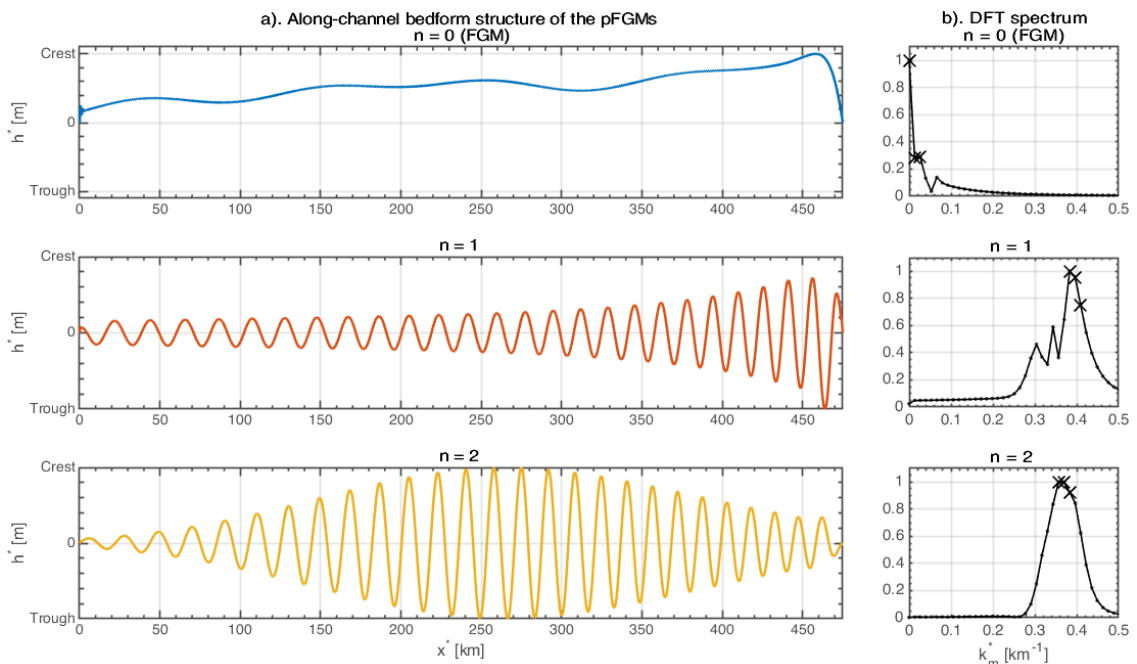


Figure 24: (a) Along-channel bedform structures of the pFGMs for the three lowest cross-channel modes (n); and (b) the corresponding Discrete Fourier Transform (DFT) spectra of the pFGMs. The bedform structures are shown for the NRL model with Neumann and Dirichlet boundary conditions (Table 4) applied to the reduced friction case in the Western Scheldt (Table 1). \times denotes the wavenumbers (k_m^* in km^{-1}) of the three monochromatic sinusoidal components that are most strongly present in the corresponding multichromatic bedform structure.